Modeling of Cardiac Biomechanics

Hvid, Rasmus

Publication date:
2024

Document Version
Publisher's PDF, also known as Version of record

PhD Thesis
Doctor of Philosophy

Modeling of Cardiac Biomechanics

Rasmus Hvid

Supervised by: Assoc. Prof. Marie Sand Traberg, PhD

Co-supervised by: Assoc. Prof. Matthias Bo Stuart, PhD
Co-supervised by: Prof. Jørgen Arendt Jensen, PhD, Dr. Techn.

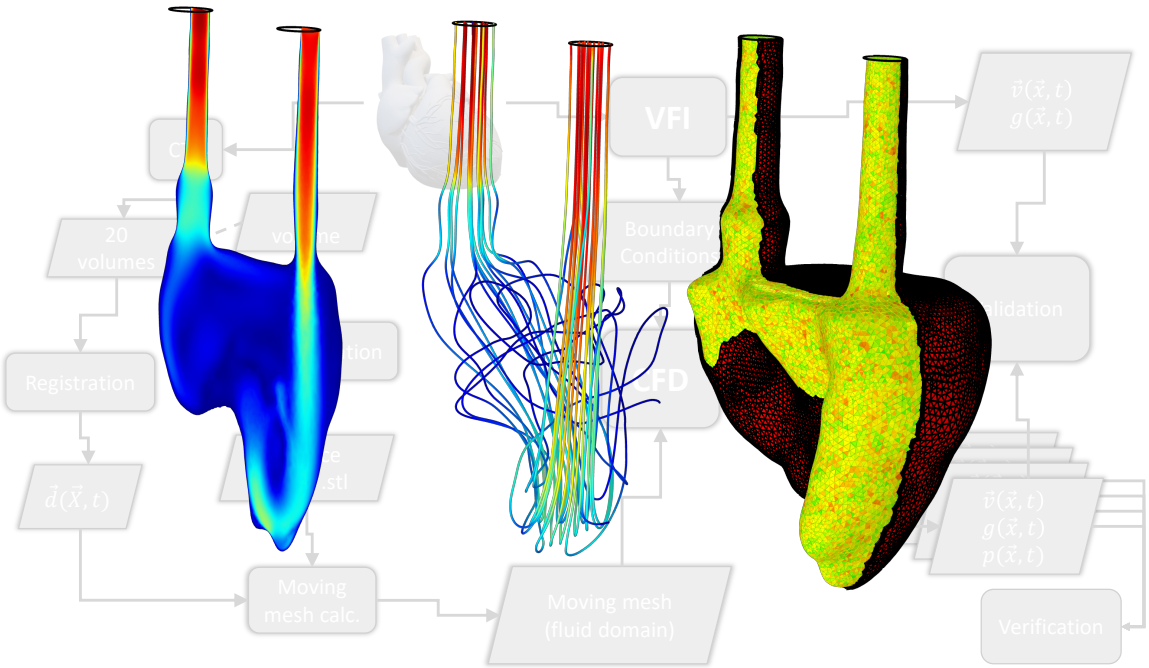

Technical University of Denmark
Kgs. Lyngby, Denmark 2023

Cover image:
Three simulation visualizations from the dynamic heart phantom study. All at the same time instance.
Left: Velocity magnitude in a single plane.
Center: Streamlines from the inlet and outlet. The colors represent velocity magnitude with the same color map as for the plane (left).
Right: Computational mesh; the boundary- and surface layers are red with black edges. The volumetric mesh (tetrahedrons) are colored after mesh quality where green is best and red is worst.
Background: Flowchart describing the simulation pipeline as applied to the dynamic heart phantom for verification and validation.

Technical University of Denmark

DTU Health Tech. Department of Health Technology

Center for Fast Ultrasound Imaging (CFU)

Ørsteds Plads 349, Room 227

2800 Kgs. Lyngby

DENMARK

Tel: (+45) 40 29 51 80

Web: http://www.cfu.dtu.dk

Author e-mail: rahv@dtu.dk

Author e-mail: rasmus@hvids.eu

Preface

This PhD thesis has been submitted to the Department of Health Technology at the Technical University of Denmark (DTU) in partial fulfillment of the requirements for acquiring the PhD degree. The research providing the foundation for this thesis has been conducted over a period of three years from April 1, 2018 to August 18, 2021, at the Center for Fast Ultrasound Imaging (CFU), Department of Health Technology. The work to finish the research and dissertation between August 2021 and January 2023 has been conducted in the free time available between a full time employment and becoming a father for the second time. The project has been supervised by Assoc. Prof. Marie Sand Traberg, PhD, co-supervised by Prof. Jørgen Arendt Jensen, PhD, Dr. Techn., and co-supervised by Matthias Bo Stuart, PhD. The project was financially supported by Innovationsfonden and I was granted financial support by the Otto Mønsteds Fond, Copenhagen, Denmark, for the IEEE International Ultrasonics Symposium in 2019. I have had the pleasure of being the first PhD student working on this project which has resulted in many interesting open problems, and I have had the opportunity to lay the first bricks in almost everything I worked with, which is something I really enjoy doing. During the project I had the opportunity to attend and contribute to conferences in Japan, Glasgow, Norway, and several online conferences as well. At a COMSOL conference I gave a talk and presented a poster which won an award of "best poster by popular vote". I had the pleasure of visiting the Norwegian University of Science and Technology (NTNU) in Trondheim, Norway for several months where in-vivo data in the form of MRI and ultrasound was acquired for the project. The last almost five years have brought some hard times in the forms of working late nights, losing a friend and colleague, a global pandemic and becoming a father. Luckily the the last years have also brought a lot of good memories in the forms of late nights, new friends, and becoming a father twice.

During the project I have had the privilege of co-supervising four MSc students in their master projects, two BSc students in their bachelor projects and several specialized courses. All were in the field of biomedical modeling.

Rasmus Hvid
Kgs. Lyngby, Denmark
January 2023

Contents

Summary

The blood flow patterns inside your heart are likely to contain information about your cardiac health. An automated pipeline for estimating these intra-cardiac blood flow patterns might one day be a vital tool, helping doctors make informed decisions in diagnosis and treatment of cardiac diseases. The pipeline is meant to work “at the push of a button” to provide novel metrics based on existing data. This project aims to prove that such a “button” can be made.

In this work a pipeline has been constructed based on temporal volumetric image registration of cardiac imaging from computed tomography or magnetic resonance which are already being used in clinic today. The pipeline is applied on a dynamic heart phantom based on a cardiac computed tomography scan. The pipeline is validated by measuring the phantom blood flow patterns using ultrasound vector flow imaging with a controlled setup aimed at repeatability and spatial precision in measurements.

The results demonstrate that with proper validation such tools may be made available to clinicians in the future and will operate "at the push of a button".

Resumé

Blodets flow mønstre inde i dit hjerte indeholder sandsynligvis informationer om dit hjerte-kar sundhed. En automatik pipeline der estimerer disse intra-cardiac blod-flow mønstre kunne en dag i fremtiden være et vigtigt redskab der hjælper læger med at træffe informerede beslutninger i forbindelse med diagnose og valg af behandling af hjerte-kar-sygdomme. Denne pipeline er tænkt som en "knap man kan trykke på" der genererer nye metrikker baseret på eksisterende data. Dette projekt har til formål at vise at en sådan "knap" kan laves.

I dette arbejde er en pipeline blevet konstrueret baseret på temporal volumetrisk billedregistrering af hjerte-billeder fra computertomografi og magnetisk resonans som allerede bliver brugt i klinikken i dag. Denne pipeline bliver anvendt på et dynamisk hjertefantom baseret på en hjerte-computertomografi skanning. Pipelinen er valideret ved at måle fantomets flowmønstre med ultralyds vector flow imaging i et kontrolleret setup med fokus på målingernes gentagelighed og spatiale præcision.

Resultaterne demonstrerer at disse redskaber, med egnet validering, en dag kan blive gjort tilgængelige til klinikere, og at de kan virke ved at "trykke på en knap".

Acknowledgements

Initially I would like to express my gratitude to my supervisor team: Assoc. Prof. Marie Sand Traberg, Prof. Jørgen Arendt Jensen and Assoc. Prof. Matthias Bo Stuart for providing me with the opportunity.
Thank you Klaus F. Kofoed (MD, PhD, DmSc Department of Cardiology, Rigshospitalet, University of Copenhagen) for making the data acquisition possible for the phantom study. Thank you to radiographer Peter Winther Rasmussen for technical insights and for executing the scan.
Thank you Sigrid K. Dahl (PhD, Seniorforsker at SINTEF Digital) for hosting my visit at NTNU and providing the opportunity of collecting in-vivo data for the project.
All of my fellow ph.d. students at CFU have never failed to brighten my day at the office, both the one at DTU and the one at home where virtual coffee meetings and frequent sharing of memes have helped keeping the morale high even at challenging times. Mikkel Schou, thank you for functioning as my sanity check and for being my friend.
Thank you Henrik Laursen for technical support and for answering my, at some times, highly irrelevant questions and for kindling my new interest in Linux and open source software.
Thank you to my family who have tirelessly tried to understand my overly technical rants, often succeeding. Thank you mom and dad for tirelessly setting up an office in your living room whenever I needed a quieter space to work.
A special thank you to my mother in law Hanne Ingmer for the support in rewriting this thesis and taking care of my girls the many nights and weekends when I could not be there myself.
Lastly, thank you to my beautiful and very patient wife Karen for always knowing when to support my work and when to remind me of life outside the simulations. Thank you for being an awesome mom to our daughters Luna and Lily while also supporting me at the same time. I hope I can repay the favor now that you have started your career in research, but mostly so I can win back some precious time with our girls.

Luna and Lily, I miss you both. Now daddy's back!

List of Figures

List of Tables

Symbols

ρ	Density, kg/m^3
μ	Dynamic viscosity, $Pa * s$
ν	Kinematic viscosity, m^2/s
∇	Del operator
∇^2	Laplace operator
$\vec{x}$	set of coordinates in 3D spatial frame, m
x	x-coordinate in spatial frame, m
y	y-coordinate in spatial frame, m
z	z-coordinate in spatial frame, m
$\vec{X}$	set of coordinates in 3D material frame, m
X	x-coordinate in material frame, m
Y	y-coordinate in material frame, m
Z	z-coordinate in material frame, m
$\vec{u}$	Velocity vector, m/s
u	x-component of $\vec{u}$, m/s
v	y-component of $\vec{u}$, m/s
w	z-component of $\vec{u}$, m/s
p	Pressure, Pa
$\vec{d}$	Displacement field vector, m
d_x	x-component of $\vec{u}$, m
d_y	y-component of $\vec{u}$, m
d_z	z-component of $\vec{u}$, m

Abbreviations

1D	One dimensional
2D	Two dimensional
3D	Three dimensional
4D	Four dimensional, often as 3D + time
BMF	Blood Mimicking Fluid
BPM	beats per minute
CFD	Computation Fluid Dynamics
CMR	Cardiac Magnetic Resonance
CT	Computational Tomography
CTA	Computational Tomography Angiography
CVD	Cardiovascular Disease
DC	Direct Current
DHP	Dynamic Heart Phantom
FDA	U.S. Food and Drug Administration
FFR	Fractional Flow Reserve
HU	Hounsfield Units
KE	Kinetic Energy
LV	Left Ventricle
MRI	Magnetic Resonance Imaging
PIV	Particle Image Velocimetry
PWM	Pulse Width Modulation
RH	Rigshospotalet
RV	Right Ventricle
SI	Sphericity Index
TKE	Turbulent Kinetic Energy
US	Ultrasound
VFI	Vector Flow Imaging
VFT	Vortex Formation Time
VL	Votex Length
VT	Vortex Trasversal
VW	Vortex Width
WSS	Wall Shear Stress

Part I

Introduction

CHAPTER 1

Introduction

Cardiovascular diseases (CVD's) are the leading cause of death globally, estimated to kill 17.9 million people worldwide in 2019 by WHO (World Health Organization 2017), which represents 32% of global deaths. 85% of theses deaths were due to heart attack and stroke. Most cardiovascular diseases can be prevented by addressing behavioral risk factors such as tobacco use, unhealthy diet and obesity, physical inactivity, and harmful use of alcohol. Early detection of cardiovascular diseases is therefore crucial, so that management with counseling and medicines can be started as early as possible. Over three quarters of CVD deaths take place in lower- and middle-income countries.

Blood flow patterns inside the heart is already recognized as a way of detecting heart disease (G.-R. Hong et al. 2008; Mohiaddin 1995). CVD diagnostic today is largely based on detecting the damage caused by the disease, such as enlarged heart, ischemia, blood pressure, fluid in lungs, etc. Being able to detect the underlying disease early, ideally before any severe symptoms even arise, would make it possible to manage the disease and perhaps even avoid some of the severe symptoms entirely. if there truly is a relationship between intra cardiac blood flow patterns and and cardiac function. Therefore intra cardiac blood flow patterns have the potential to provide so-called subclinical markers of impaired LV function (Eriksson et al. 2013). Detection of early changes in blood flow patterns is therefore a possible new tool in detecting the very early stages of cardiac disease and prediction of prognosis.

1.0.1 Motivation

Intra cardiac blood flow patterns are expected to bring new metrics to diagnostics, prediction of prognosis, treatment decision, and surgery planning. The motivation for this work is to contribute to the low-level end of the science by describing a pipeline for obtaining 4D intra cardiac blood flow patterns by simulation. Furthermore simulation based metrics will only find their way to clinical use if they are reliable, accurate and precise enough to base diagnostics on. This thesis aims to contribute to the need of a low-level validation of the geometry prescribed computational fluid dynamics (CFD) method, with the purpose of quantifying the reliability of the method itself. In the early stages of developing a pipeline, this is a crucial step before in-vivo validation, although in-vivo validation is a planned part of the project as well.

1.0.1.1 The emerging trend of simulating intra cardiac flow patterns

The use of intra cardiac flow patterns for diagnosis is a relatively new tool in clinic. These flow patterns are measured using a variety of medical imaging techniques and show a promising potential for early detection of disease. Simulating intra cardiac blood flow patterns has become an emerging trend in several fields of research. There already exists a large number of publications on the topic, including many different approaches, implementations, and possible use cases. These are elaborated in Section 2.2. No clinical implementation of intra cardiac CFD has been found in the literature search during the presented work. CFD does however exist in the clinical cardiology. Most noteworthy is the FDA approved CFD estimate of fractional flow reserve (FFR) in the coronary arteries based on computed tomography angiography (Taylor, Fonte, and Min 2013), (Zarins, Taylor, and Min 2013), (Leipsic et al. 2014), (Norgaard et al. 2014). FFR measurement normally requires cardiac catheterization which is an invasive procedure.

1.0.1.2 Currently used flow based diagnostic metrics for CVD's

Intra cardiac blood flows have been investigated for diagnostics for a long time. As the methods for measuring and estimating intra cardiac blood flows have evolved, the diagnostic flow metrics have multiplied. It is well established that using intra cardiac blood flow patterns as a diagnostic metric is feasible (Mohiaddin 1995)(G.-R. Hong et al. 2008). Some of the currently investigated metrics are based on flow velocity and volume flow rate. Often in the form of peak velocity over the heart valve, or cardiac output. Outside the heart, peak velocity is used for assessing the severity of stenosis in arteries. For this purpose wall shear stress (WSS) is also a recognized metric. Energy based metrics are often used as an overall metric of heart function, and often related to ventricular heart function. This might be in the form of an overall kinetic energy (KE), but also in the form of turbulent kinetic energy (TKE) to assess severity of stenosis in blood vessels. The most widely investigated blood flow pattern based phenomenon inside the ventricles is vortex formation. A variety of vortex based metrics have been correlated with heart dysfunction. Examples of vortex based metrics are vortex depth (VD) which represents the vertical position of the vortex core/center relative to the long axis of the left ventricle (LV). Similarly vortex transversal position (VT) indicates the relative position on the posteroseptal axis. These vortex location based metric have been shown to be correlated to cardiac dysfunction in (G. R. Hong et al. 2013). Furthermore vortex morphology based metrics have also been proposed in (G. R. Hong et al. 2013). Examples of vortex morphology based metrics are vortex length (VL), vortex width (VW), and sphericity index (SI). VL is measured on the longitudinal axis, VW on the horizontal axis, and SI is the ration of VL to VW. These shape based measurements change during the cardiac cycle, and vortex morphology based measurements at specific points in time in the cardiac cycle have been shown to be correlated to LV systolic and diastolic dysfunction. Another

flow based metric that requires 4D flow is ratios of the four flow components which are defined in (Eriksson et al. 2013) as direct flow, retained flow, delayed ejection and residual volume. Direct flow is the volume of blood that enters the LV in diastole and exits in systole within the same heart beat. Retained flow is the volume of blood that enters LV during diastole, but does not exit in the following systole. Delayed ejection flow is the volume of blood that already exists in the LV, i.e. did not enter during the previous diastole, and exits during systole. Residual volume is the volume of blood that does not enter nor exit LV during the heart beat. The ratio between these four flow types provide an indication of cardiac health.

1.0.2 Objective

The objective is to develop and test a pipeline that estimates the 4D intra cardiac blood flow well enough to enable extraction of the above mentioned metrics. It is expected that the pipeline will be able to exceed the quality of existing measurement techniques. The objective is therefore first to provide an alternative to existing measurement methods of intra cardiac blood flow patterns. Then, when the quality of the blood flow pattern estimation becomes greater than existing techniques, new metrics can be based on the simulated flow patterns. As there already exists published work on implementation and in-vivo validation of intra cardiac blood flow pattern simulations, this work will focus on validation using a phantom. This allows for a more detailed comparison because of the nature of the phantom compared to in-vivo. The pipeline shall be based on geometry prescribed CFD, based on 4D medical imaging. The main tools are volumetric image registration using MATLAB (The MathWorks, Inc.), and numerical simulations in COMSOL Multiphysics (COMSOL AB Stockholm, Sweden). It is the ambition to make choices that ease automation when possible, as an end goal for the pipeline is to be independent of operator and usable for clinicians which are not CFD experts. The goal of the presented work is to answer whether such a pipeline can be made, and whether the pipeline produces flow patterns similar to ground truth measurements. The objectives can be condensed into the following research questions which will be addressed in this thesis.

- Can the blood flow patterns inside the human heart be predicted based on patient specific movement of the heart?
- How can the movement of the human heart be estimated from 4D medical imaging for the purpose of estimating the blood flow patterns?
- In addition to estimating the patient specific movement of the heart, what elements are required in a pipeline for setting up a patient specific geometry prescribed CFD that is based on 4D medical imaging? Note that the pipeline should developed with automation in mind.
- How can a pipeline that estimates blood flow patterns based on moving geometry of the heart be validated?

1.1 Scientific Contributions

Below is a list of scientific contributions resulting directly from work during this project.

1.1.1 Publications

List of written published work during the project, including posters, conference papers and journal articles.

- **Paper 1** "Validation Platform for Development of Computational Fluid Dynamics of Intra-Cardiac Blood-Flow"
  ***Rasmus Hvid**, Jørgen Arendt Jensen, Matthias Bo Stuart, Marie Sand Traberg*
  Proceedings of IUS 2019
  Summary: Simulation of dynamic heart phantom and comparison with ultrasound VFI measurement. Movement in simulation is prescribed by known analytic function.

- **Paper 2** "Intra-Cardiac Flow from Geometry Prescribed Computational Fluid Dynamics: Comparison with Ultrasound Vector Flow Imaging"
  ***Rasmus Hvid**, Jørgen Arendt Jensen, Matthias Bo Stuart, Marie Sand Traberg*
  Cardiovascular Engineering and Technology (CVET) *(In review)*
  Summary: Simulation of dynamic heart phantom and comparison with ultrasound VFI measurement. Movement in simulation is prescribed by a displacement field estimated from volumetric image registration on 4D CTA of dynamic heart phantom.

- **Poster 1** "Image based, geometry prescribed CFD of intra-cardiac flows on a dynamic heart phantom"
  ***Rasmus Hvid**, Marie Sand Traberg*
  Technical conference: COMSOL conference 2020 Europe
  Summary: Technical implementation of prescribing 4D displacement field to geometry in COMSOL. Won best poster by popular vote at conference.

- **Poster 2** "A New Technique of Reconstructing 3D Geometries From CT Images - A CFD Study"
  *Masoud Meskin, **Rasmus Hvid**, Marie Sand Traberg*
  Congress of the European Society of Biomechanics
  Summary: Presentation of method for creating simplified 3D geometries based on the human left atrial chamber as preparation for CFD study.

1.1.2 Presentations

- **Talk 1** "Validation Platform for Development of Computational Fluid Dynamics of Intra-Cardiac Blood-Flow"
  ***Rasmus Hvid**, Jørgen Arendt Jensen, Matthias Bo Stuart, Marie Sand Traberg*
  Oral presentation at IUS 2019
  Summary: Simulation of dynamic heart phantom and comparison with ultrasound VFI measurement. Movement in simulation is prescribed by known analytic function.

- **Talk 2** "Image based, geometry prescribed CFD of intra-cardiac flows on a dynamic heart phantom"
  ***Rasmus Hvid**, Marie Sand Traberg*
  Technical conference: COMSOL conference 2020 Europe
  Summary: Technical implementation of prescribing 4D displacement field to geometry in COMSOL.

1.1.3 Student projects

- **Master thesis 1**
  "Constitutive Modeling of the Heart"
  Student: Marion Lopez

- **Master thesis 2**
  "Effect of Boundary Conditions on the Prediction of Blood Flow Patterns in the Human Left Ventricle"
  Student: Pernille Højgaard Petersen

- **Master thesis 3**
  "Biomechanical Modelling of the Right Ventricle"
  Student: Morgane Garreau

- **Master thesis 4**
  "Development of a Bi-ventricular Heart Model"
  Student: Alberta Zaja

- **Bachelor thesis 1**
  "Investigation of Material Properties and Outlet Conditions in Carotid Phantoms"
  Student: Frederikke Hübenbecker Poulsen

- **Bachelor thesis 2**
  "Flow Investigation in a Heart Phantom Model"
  Student: Josefine Harbo Arleth

1.2 Outline of Dissertation

The main goal of this ph.d. is to develop and validate a CFD pipeline for simulating human intra cardiac blood flow patterns from 4D medical imaging. The dissertation is split into parts to describe the steps behind the pipeline validation. The phantom study, which is described in [Paper 2] , is the main result and is described further in Part III. More work is planned with the phantom as well as with in-vivo MRI data acquired during the ph.d. Part IV is dedicated to describing current state and next step.

Part I - Introduction

Chapter 1: Introduction
This chapter provides an introduction to relevant topics as well as motivation, objectives, research questions, list of scientific contributions, and this outline of the dissertation.

Chapter 2: Background
This chapter provides background information about the human heart and state of the art for intra cardiac blood flows. The basis of the most important technical tools are described as well, these include: image modalities, fluid dynamics, discretization, and volumetric image registration.

Part II - The Pipeline

Chapter 3: The Pipeline
This chapter provides a holistic description of the entire pipeline divided into sections; 4D imaging, registration, segmentation, boundary conditions and CFD. The purpose of this chapter is to show how the sections interact. The implementation of the sections are described in the following chapters.

Chapter 4: Dynamic Heart Phantom
This chapter provides a description of the dynamic heart phantom used for validation, the problems encountered, and future plans, including a new setup jig for the DHP, and a robot arm setup.

Chapter 5: Moving Geometry and Registration
This chapter provides an overview of how volumetric image registration is implemented in MATLAB to estimate the displacement of the left ventricle based on 4D CTA.

Chapter 6: Implementation in COMSOL
This chapter provides a detailed description of how the CFD was implemented in

COMSOL.

Chapter 7: Data Acquisition
This chapter provides an overview, description and presentation of all data acquired during the project.

Part III - Results and Discussion

Chapter 8: Results
This chapter provides an overview and extended discussion of the main results obtained using the dynamic heart phantom.

Part IV - Outro

Chapter 9: Discussion and Future Perspective
In this chapter the main points of the dissertation are summarized and discussed. Advantages and limitations of the pipeline are presented, discussed and the future perspective is outlined.

Chapter 10: Conclusion
Conclusion on the presented research.

CHAPTER 2

Background

This chapter provides the background theory and information that serve as a foundation to the methods, results and choices made in the presented research. The topics are not going to be exhaustively explained, but rather described as concepts. The descriptions in 2.1 is based on (OpenStax 2021).

2.1 The Human Heart

The human heart is a vital organ that pumps oxygenated blood from the lungs to all body parts and back to the lungs again. Besides oxygen, blood also transports hormones, nutrients, waste, immune cells, etc. In addition to transportation, the heart is also responsible for maintaining blood pressure, which is necessary to pump blood up to the head, against gravity, and for keeping differential pressure around the body for other functions. The heart must be able to react to different circumstances coming from the outside, such as increasing the blood flow during sports to provide more oxygen to the muscles. The regulation of the heart is very complex and is the results of many factors from blood pressure to activity, and even psychological pressure like giving a presentation in front of an audience.

The human heart is always at work with a very little permissible error rate. If a human heart on average beats 75 times per minute, it contracts about 108,000 times per day, which is over 39 million times per year. After 75 years that amounts to nearly 3 billion contractions. If the heart stops beating efficiently, even for a few minutes, it can cause permanent damage or even death.

2.1.1 Anatomy

The healthy human heart is about the size of a fist, located within the thoracic cavity between the lungs, and points slightly to the left. The heart is protected by the rib cage and a pericardial sac inside the pericardial cavity. The pericardial sac, besides protection, also ensure free movement for contractions with low friction. The top of the heart is referred to as the base and the bottom tip of the heart is referred to as the apex.

The human heart consists of four chambers, see Fig. 2.1; two lower chambers, the left and right ventricles (LV, RV), and two upper chambers, the left and right atria. The inner layer of the heart is referred to as the endocardium. The inner walls of the ventricles are lined with trabeculae carneae, ridges of cardiac muscle covered by endocardium.

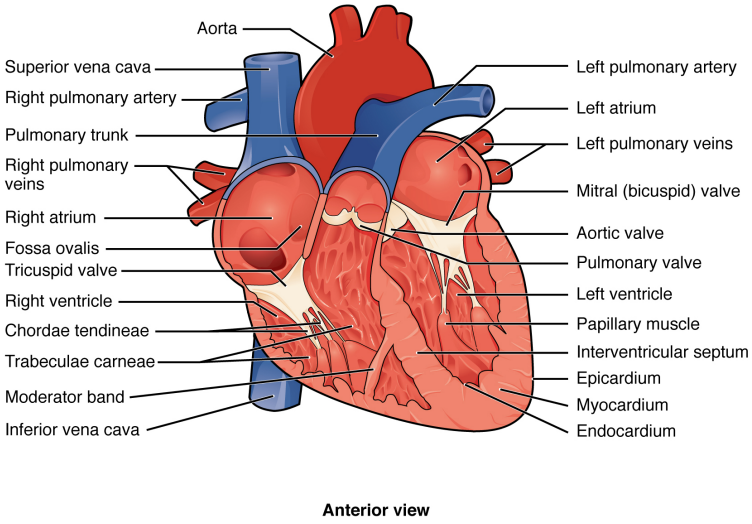

Figure 2.1: Cut plane view of the human heart with all four chambers and all four valves visible. Modified from (OpenStax 2021)

The human heart is often divided into the "right heart" (right atrium, right ventricle) and the "left heart" (left atrium, left ventricle). This makes sense because the left heart and right heart function as two parallel pumps. The right ventricle pumps blood to the pulmonary circuit for oxygenation. After oxygenation the blood enters the left atrium, which is connected to the left ventricle, which pumps the oxygenated blood to the rest of the body through the systemic circuit. The systemic circuit terminates in the right atrium which is connected to the right ventricle, where the now deoxygenated blood is pumped to the lungs for oxygenation once again. See Fig. 2.2.

2.1.1.1 Heart valves

The heart has four valves. Two heart valves, located between each atrium and ventricle, are referred to as the atrioventricular heart valves. The atrioventricular valve between the left atrium and left ventricle is called the mitral (bicuspid) valve. The atrioventricular valve between the right atrium and right ventricle is called the tricuspid valve. The remaining two valves are the ventricle outlets, also called the semilunar heart valves. The semilunar heart valve at the right ventricle outlet to the pulmonary circuit is called the pulmonary valve. The semilunar valve at the left ventricle outlet to the systemic circuit via the aorta is called the aortic valve. The atrioventricular valves are reinforced by the chordae tendineae which are connected to papillary muscles in the ventricles, see Fig. 2.1.

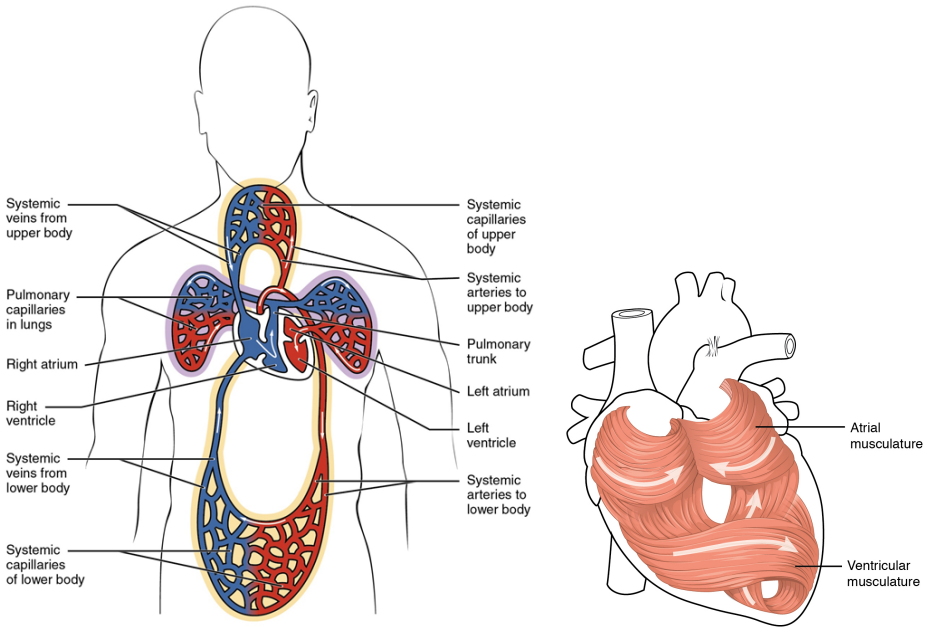

Figure 2.2: Left: Illustration of the systemic circuit and pulmonary circuit and their connections to the left and right heart. **Right:** Illustration of the orientations of the cardiac muscle fibers. The illustrations are modified from (OpenStax 2021)

2.1.2 Physiology

The left and right heart pump blood by contracting cyclically while the heart valves unify the flow direction. The contractions are initiated and timed by an electrical conduction system. The electrical signals are measurable externally by placing electrodes on the chest. The signal from 12 standardized leads are called an electrocardiogram (ECG). While the pipeline in this work does not model electrophysiology, the ECG signal is used for timing the acquisition of medical images. The cardiac phases are usually defined from the ECG (see Fig. 2.3).

2.1.2.1 The Cardiac Cycle

The cardiac cycle is generally divided into ventricular systole and diastole, where systole is the contraction phase and diastole is the relaxation phase. See Fig. 2.3. The myocardium is arranged in a twisted path which causes the ventricle to twist as they contract. See Fig. 2.2. The ventricular systole can be further subdivided into isovolumetric contraction which is

the start of the systole where all of the heart valves are closed, and ventricular ejection when the semilunar valves open. The diastole can be subdivided into isovolumetric relaxation which is the start of the diastole where all of the heart valves are closed. When the atrioventricular heart valves open the ventricular filling phase, or passive filling phase, starts. In the end of the ventricular systole, the atria contract, in the atrial systole. Naturally the pressure is highest during systole and lowest during diastole. The left ventricle operates at approximately four times the pressure of the right ventricle. Therefore the myocardial wall of the left ventricle is thicker on the left side. For timing reference of pressures and valve operation in relation to the ECG, see Fig. 2.4.

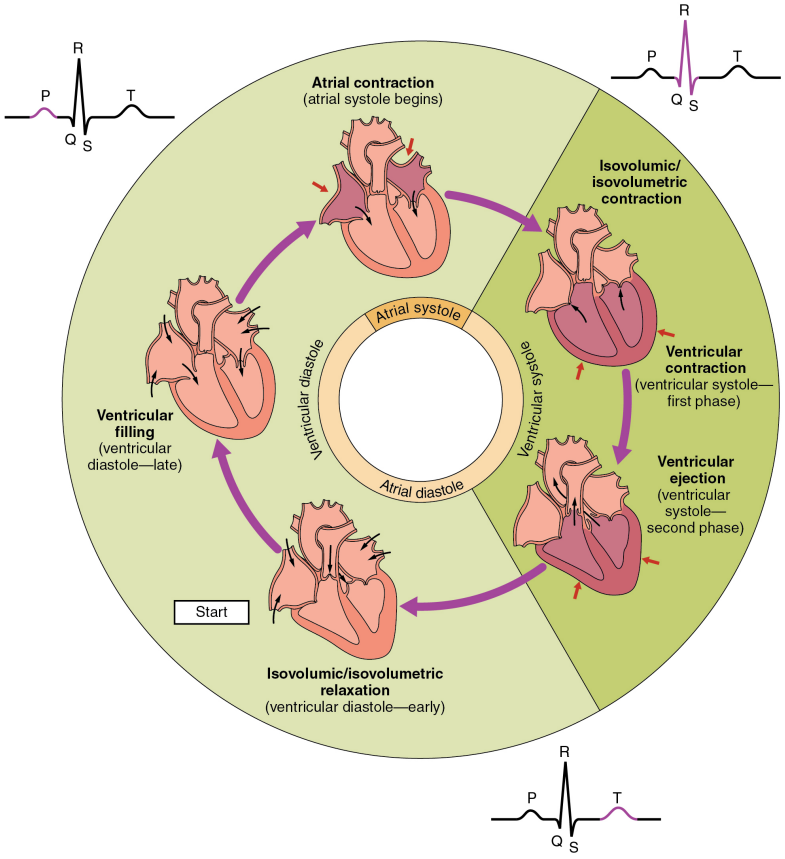

Figure 2.3: Overview of the cardiac cycle. Modified from (OpenStax 2021)

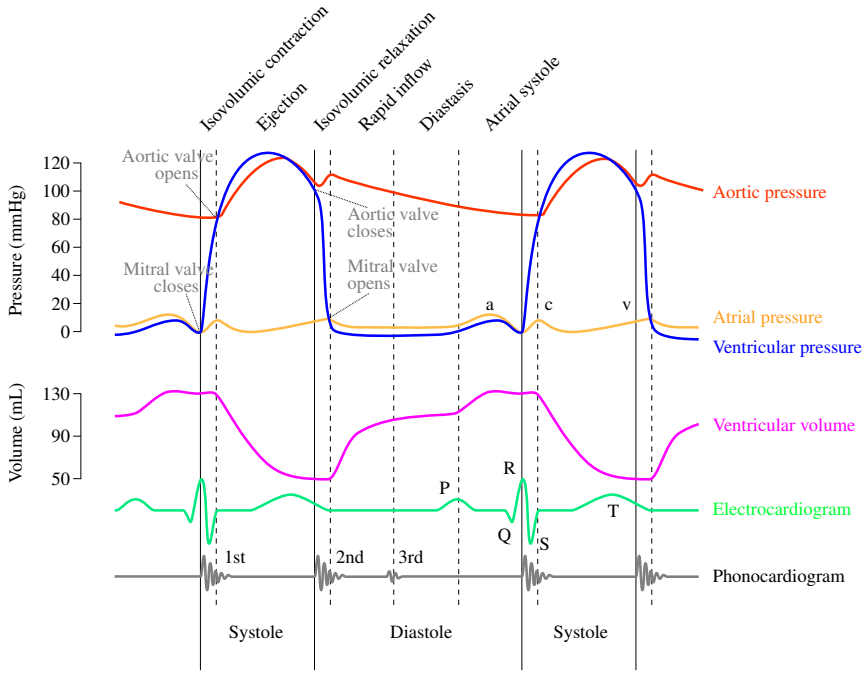

Figure 2.4: Wiggers Diagram. A famous diagram illustrating the relationships between pressures, volumes and valve states over the cardiac cycle. Modified from Wikipedia.

From Wikipedia. *By adh30 revised work by DanielChangMD who revised original work of DestinyQx; Redrawn as SVG by xavax - Wikimedia Commons: Wiggers Diagram.svg, CC BY-SA 4.0, https://commons.wikimedia.org/w/index.php?curid=50317988*

2.2 Flow Simulation in the Human Heart

The earliest literature describing the flow patterns inside the heart dates back to year 1513. Here Leonardo da Vinci describes the flow inside hearts from animal studies, which is commented on in (Keele 1951). The anatomical descriptions were accurate, but some assumptions were made about the circulation and cardiovascular functions based on intuition alone. Later, attempts of describing the flow patterns inside the heart were made in various phantom studies by a combination of direct observations and direct measurements. The earliest found were (B. Bellhouse and F. Bellhouse 1969; B. J. Bellhouse and F. H. Bellhouse 1968; B. J. Bellhouse and Talbot 1969) which are phantom studies of fluid mechanics around and through the mitral valve and the aortic valve. Phantom studies are still very relevant today, as they provide superior repeatability and

measurement conditions compared to in-vivo studies. In (Vedula et al. 2014), flow inside a moving transparent phantom is simulated and compared to particle image velocimetry (PIV) measurements of the phantom, which serves as a validation of the method under simplified conditions. This approach to validation is similar to the work presented in this dissertation, although the dynamic heart phantom (DHP) is better suited for this pipeline as it mimics the human heart more truthfully in computed tomography angiography (CTA).

In their study (Lopez-Perez, Sebastian, and Ferrero 2015) provide an excellent overview of the development of intra cardiac CFD through time. In summary, two events have had a major impact of the personalized intra cardiac CFD simulations: computer power and medical imaging. Before computer power and patient specific imaging were readily available, the cardiac models were based on mathematically defined boundaries. First the boundaries were curves in 2D which over time became surfaces in 3D. Next the surfaces went from being static surfaces, to dynamic moving surfaces. An early adaptation of a moving 3D patient specific geometry is (Segars et al. 1999) which used non-uniform rational basis splines (NURBS) to define the inner and outer walls of the atria and ventricles. Applying patient specific moving geometry is in itself not novel anymore, however the implementation and benefits of different model types are still being investigated for different purposes.

2.2.1 Model choices and computational methods

The pipeline presented in this project has the purpose of estimating the intra cardiac blood flow patterns as precisely and accurately as possible based on the moving geometry of the heart. In cardiac modeling several modeling approaches can be utilized depending on the purpose of the model and the availability of input data. It is the assumption in this project that all parameters affecting the blood flow patterns are captured by the movement of the heart. A model based on this approach is however not capable of directly simulating the specific cause of blood flow pattern changes such as ischemia or electrophysiological defects. Taking these specific changes into account would require a different modeling approach and another type of input data. It is an important point for all simulation models in general that the most complicated and comprehensive model is not necessarily the best choice. Generally it is a rule of thumb to keep it as simple as possible for the given purpose. A comprehensive multiphysics simulation might provide more information, but it has the trade-off of requiring more input data, more computational resources, and in general such a model has more sources of error.

Below are listed the overall categories for model choices as categorized in (Lopez-Perez, Sebastian, and Ferrero 2015). Note that these categories are based mainly on the mathematical model choice, and not discretization methods. Often the discretization method itself has a great influence on the model choice as the different discretization methods have different limitations. Of course any discretization method should converge towards the same solution when applied to the same mathematical model once mesh

independence, or grid independence, is achieved. Depending on the chosen mathematical model some discretization methods achieve this faster, and easier, than others.

2.2.1.1 Pure CFD

This model type is the subject of this dissertation. Pure CFD models are often geometry prescribed with moving boundaries based on 4D medical imaging, but can be stationary as well. In the case of moving geometry the simulation can also technically be defined as a one-way coupled FSI model. For modeling movement, two popular numerical formulations are competing; arbitrary Lagrangian Eulerian formulation (explained in Section 2.4.4) and immersed boundary method (IBM) which is a numerical approach based on the Eulerian formulation alone. See (Peskin 1972). Investigations of using smoothed particle hydrodynamics is also being investigated. See (Caballero et al. 2017). The main purpose of pure CFD simulations is often to provide an estimation or measurement of blood flow patterns that is patient specific and non-invasive. Clinicians are still skeptical of CFD in the clinic (Zhong et al. 2018), however some CFD methods are already in use. An example is fractional flow reserve (FFR) which is mentioned in Section 2.2.3. The clinical application, and reception, of left ventricular fluid mechanics is discussed in (Pedrizzetti and Domenichini 2014) titled: "The long way from theoretical models to clinical applications" which underlines the difficulty of applying functioning simulation models to provide clinical value.

2.2.1.2 Fluid Structure Interaction

Fluid structure interaction (FSI) cardiac models is a subcategory of multiphysics cardiac models which simulate both the intra cardiac fluid dynamics and the solid mechanics of the myocardium. In a two-way coupled FSI model, the effect of the myocardium on the blood as well as the effect of the blood on the myocardium is simulated. FSI models are more complex when compared to pure CFD models, but they do offer more flexibility and information. Additionally FSI models need more model inputs, as the geometry and, possibly anisotropic, solid material properties needs to be characterized. FSI models are also useful for modeling heart valves as seen in (Mao et al. 2017).

2.2.1.3 Multi-physics

FSI is only one form of multiphysics simulations which takes the interactions between fluid and solid into account. Other types of multiphysics cardiac simulations could include interactions from even more physics, such as electrophysiology, calcium concentrations, perfusion, and more. Examples of cardiac multiphysics simulations can be found on the (Technology 2022) , and in the Alya Red simulation in (Vázquez et al. 2015).

2.2.1.4 Total Heart Function

Simulating total heart function, especially patient specific total heart function, is a long way ahead. The clinical value of patient-specific total heart function simulation is small compared to patient specific pure CFD or FSI simulations. Simulating total heart function does however suggest some interesting research options. An example of an ideal scenario could be replacing a cohort of patients in a clinical trial, of a new drug or intervention, with a cohort of total heart function simulations in an in-silico trial. An example of this is presented in (Sarrami-Foroushani et al. 2021) where the authors were able to replicate the results of a clinical trial using simulations, referred to as in-silico trials, of endovascular medical devices. An example of total heart function simulation can be found at the living heart project and (Hunter, Pullan, and Smaill 2003): "Modeling Total Heart Function".

2.2.2 Validation

Validation is an important part of a simulation pipeline, as it is a necessary step before trusting the simulation results. Validation of intra cardiac blood flow patterns is usually done in one of two ways. One way of validation is in-vivo as in (Lantz, Gupta, et al. 2018) where a simulation pipeline is applied on human subjects and compared to 4D flow magnetic resonance imaging (MRI) as ground truth on clinically relevant metrics. The other way of validation is by phantom study, where a pipeline is applied on a phantom and compared to measurements of the phantom as ground truth as in [Paper 1] and [Paper 2] . Using a phantom for validation has several advantages over in-vivo. One advantage is that a phantom can be measured in more ways than a human. This is demonstrated in [Paper 1] and [Paper 2] where highly controlled ultrasound flow measurements can be made, which would have been otherwise impossible in-vivo. Even optical PIV, which has a better spatiotemporal resolution compared to the in-vivo state-of-the-art techniques, can be used as ground truth in a phantom study, as demonstrated in a study by (Vedula et al. 2014). In phantom validation, comparing the CFD to the ground truth becomes easier because landmarks can be utilized for co-registration. Furthermore the phantom movement is controlled and repeatable, which eliminates many uncontrolled deviations between CFD and ground truth originating from in-vivo data.

2.2.3 Existing Published Work on Intra Cardiac Flow Simulation

4D CFD from CT has been done before - even validation studies using quantitative methods (Lantz, Henriksson, et al. 2016) and (Lantz, Gupta, et al. 2018). In the latter, Lantz et. al. focus on validation against clinically relevant metrics such as stroke volume, peak flow rate, and KE at various phases of the cardiac cycle. This type of validation is a crucial step from research to actual clinical use. While these clinical metrics are important, they are averaged over either large volumes, large time spans, or both. If geometry prescribed simulation models are going to provide a better spatiotemporal resolution of the blood flow patterns when compared to the current gold standard, the validation of

these models must be based on other than the gold standard itself. This is achievable by developing a reliable and repeatable test setup and utilizing ground truth measurement modalities that provide a higher spatiotemporal resolution than the current gold standard.

The use of 4D flow, and flow visualization is presented in (Munoz et al. 2013) which explains the role of the vortex and introduces the vortex formation time (VFT) metric.

Effects caused by papillary muscles in the LV has been tested before by Lantz et. al. in (Lantz, Henriksson, et al. 2016), where it is concluded that it does affect the resulting flow patterns. At least on "resident time". In (Lantz, Henriksson, et al. 2016) segmentation is performed by an experienced user, and registration is overseen by an experienced user.

Several relevant review have been published. Among them is (Zhong et al. 2018) which includes an exhaustive list of research about patient specific CFD simulations of heart ventricles from 2018. In this review it is concluded that "even if FFR is FDA approved, there is an understandable hesitancy to embrace the approach due to the methods being new and fairly undeveloped still." Which is discouraging at first, however they also conclude that there is good reason to push through with simulation methods, since acceptance is slowly on the way. Another influential review is (Doost et al. 2016), which is a perspective review that covers a lot of areas, including inlet/outlet handling as well as non-Newtonian fluid properties which is shown to have an effect on WSS measurements in similar simulations with Newtonian and non-Newtonian fluid properties respectively. Also worth mentioning is the relatively old review (Khalafvand, Ng, and Zhong 2011) which is a CFD simulation perspective review which concludes that FSI is the most "profound and promising one" of the heart simulation methods. (Lopez-Perez, Sebastian, and Ferrero 2015) presents a comprehensive flowcharts based on 60 models dating 50 years back. The models are however focused primarily on geometry and electrophysiology. Another review, (Mittal et al. 2016), addresses computer hardware and show hardware scaleability plots and discusses advantages and disadvantages of different imaging modalities. Here, segmentation tools are discussed as well, and it is stated that in "virtually no case" can segmentation be automated.

2.3 Imaging modalities

This section provides a brief overview of the imaging modalities used. For the phantom study (see Chapter 4) CTA was used for obtaining the 4D images for the geometry prescribed CFD. Ultrasound VFI was used to measure flow inside the phantom for validation. Furthermore B-mode imaging was used for navigating the vector flow imaging (VFI) measurements and for co-registration between the CFD and VFI for validation. MRI data were acquired as well although the pipeline has not been implemented on this yet. The section is based on information from the books: (Prince and Links 2006) and (Nishimura 2010).

2.3.1 Ultrasound

Ultrasound is a widely used imaging modality because of the relatively low cost and portability. For most types of ultrasound there are virtually no risks for the patient, which is is emphasized by the fact that ultrasound is a standard examination during pregnancy. See Fig. 2.5. While ultrasound is portable and relatively low cost, it does require training of the operators as the findings often need interpretation during the scan, unlike CT and MR where the interpretation can be made after the scan is finished.

Figure 2.5: Example of B-mode fetal ultrasound.

Medical ultrasound is built on the foundation of sending ultrasound pulses through tissue and recording the echoes that return from scatters in the tissue. An image can be calculated based on the time delay of these echoes. An ultrasound system requires

a transducer probe, a computer, and a monitor. The ultrasound transducer must be in contact with the skin via a special gel to help the ultrasound pulse propagate through the tissue.

2.3.1.1 B-MODE

Ultrasound B-mode, or brightness mode, shows contrast based on changes in acoustic impedance in the tissue. This is the most know type of ultrasound. Fig. 2.5 is an ultrasound B-mode image. B-mode imaging can be achieved on most US systems and is often used for "navigation" for other US modalities as an overlay. See Fig. 2.6.

2.3.1.2 VECTOR FLOW IMAGING

Vector flow imaging (VFI) is based on phase shift estimation from a scatter field obtained by transverse oscillation (Jensen and Munk 1998). The technique provides a real-time B-mode image with a real-time color and vector overlay, showing direction and magnitude of the blood inside a sub-region on the B-mode image. See Fig. 2.6. The wider the overlay region is, the lower the effective VFI framerate becomes. Depth has little impact on effective framerate.

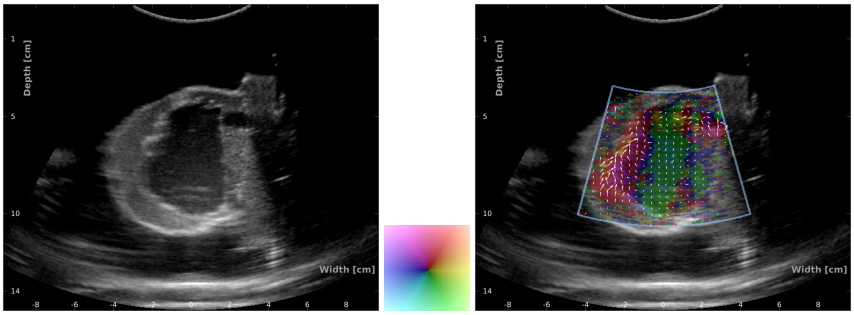

Figure 2.6: Example of ultrasound vector flow imaging. **Left:** B-mode image of the right ventricle of the DHP. The ventricle outlet is visible in the top right of the cavity. **Center:** Colorwheel which is the color legend of the VFI overlay on the right image. The colors are angle-dependent, and the brightness is magnitude dependent. The maximum velocity is determed by the scanner settings, and is not included in this illustration. **Right:** The same B-mode image as the left, but with VFI color overlay from colorwheel in center image. The white arrows point in the flow direction, and the arrowlength is proportional to velocity magnitude.

2.3.2 Computed Tomography

Computed tomography (CT) is an x-ray based image modality which calculates a slice, or a stack of several slices in a volume, from x-ray images taken from multiple directions. The output data from CT are usually slices or volumes with contrast based on x-ray attenuation measured in Hounsfield Units (HU). Because CT is based on x-rays, it exposes the patient to ionizing radiation.

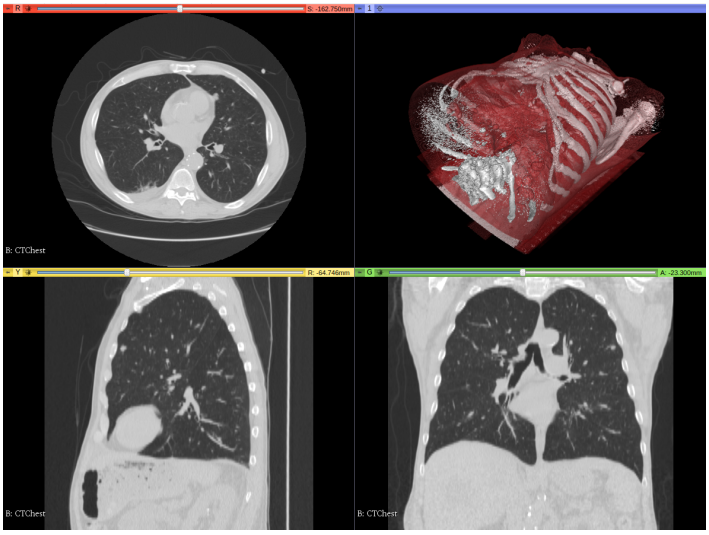

Figure 2.7: Chest CT from 3D Slicer's sample data.

2.3.2.1 Cardiac CT

Cardiac CT, often in the form of CT Angiography (CTA), is like regular CT, but with ECG based gating to time the acquisition. The gating is necessary to acquire an image of the heart in the intended phase of the cardiac cycle. Usually CTA only acquires a single volume at late diastole where the heart is the most stationary. If the pulse is high (above 65 bpm for the Canon Aquilion ONE) the CT system needs to patch measurements from several heart beats to get enough angles for an image, where the limitation is the revolution time of the system. By predicting the heart position from the ECG, the acquisition can be limited to a very small time instance. This is called prospective gating. To acquire data from the entire cardiac cycle, a continuous acquisition, including the ECG signal, can be made. The data are automatically divided into phases, usually in 5% increments, in post processing. This process, called retrospective gating, results in 20 time sequential volumes over one cardiac cycle. Often contrast fluid is injected intravenously to better view the coronary arteries and cardiac anatomy.

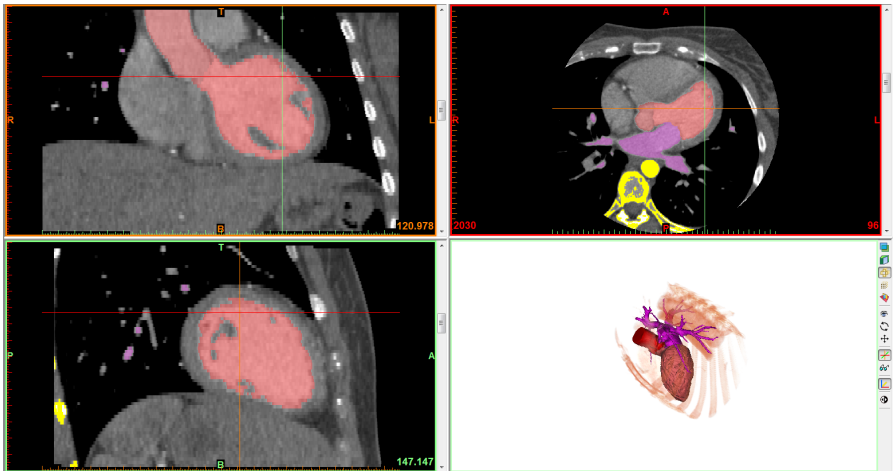

Figure 2.8: Example of CTA: screenshot from Mimics Research. Visible is three orthogonal planes of a volume of a human heart. A volume rendering is seen in the bottom right corner. A segmentation is visualized in colored surfaces. See Fig. 5.2. Modified from (Hvid 2018).

2.3.3 Magnetic Resonance Imaging

MRI is an imaging modality with many uses due to the many available types of acquisition sequences. MRI is best known for the excellent soft tissue contrast and the fact that there is no ionizing radiation involved like there is in CT. However compared to CT, MRI is more expensive and the acquisition takes more time.

An MRI scanner has a large stationary magnetic field which causes protons to precess at a specific frequency, proportional to the strength of the field, when excited. After excitation at the given frequency, the relaxation time of the protons depends on the tissue type. This is what provides the contrast in MRI. Many different sequences can provide different contrasts types depending on what anatomy is visualized. The image is obtained by spatially encoding the protons using gradient coils which adds changing gradients to the static magnetic field. The gradient in the magnet field causes the protons to precess at different frequencies which is detectable and used for spatial encoding.

2.3.3.1 Phase contrast

Phase contrast MRI (PC MRI) takes advantage of the effects flow has on the phase of the MRI signals. By obtaining two images with different gradient encoding, flow in a single direction can be visualized, and even quantified. To obtain 3D flow, this has to be repeated three times in total with orthogonal gradient encoding. See Fig. 2.9. When encoding the images a velocity encoding is defined, which is the maximum measurable velocity, ± 120

cm/s for example.

4D flow MRI can be obtained by phase contrast MRI with cardiac gating, with velocity encoding in three orthogonal directions for each plane in a stack of planes covering the heart. See Fig. 2.9.

4D flow MRI is constantly being developed and can be obtained from several methods. See (Markl et al. 2012). The pipeline in this thesis is developed for CTA but with 4D flow MRI based on phase contrast MRI with cardiac gating in mind as an alternative.

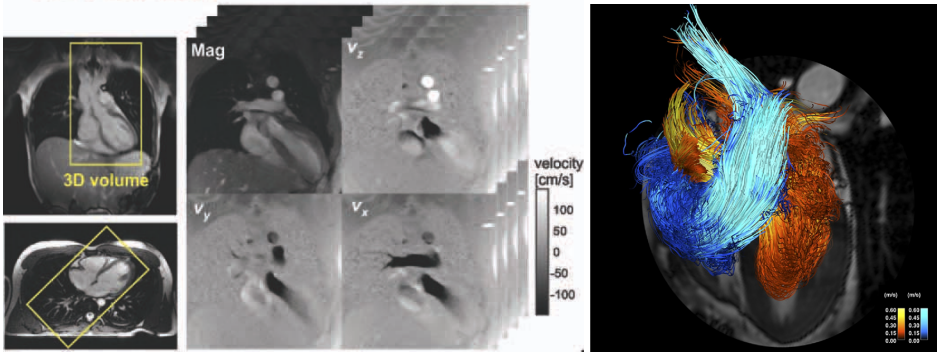

(a) (Markl et al. 2012) (b) (Sengupta et al. 2012)

Figure 2.9: (a): Example of 4D flow data. The 3D bounding box of the heart is visualized to the left. To the right, the raw data are visualized; The anatomical image "Mag", and the velocity along the 3 primary axes; v_x, v_y, and v_z from ca. -120 cm/s to 120 cm/s. Modified from (Markl et al. 2012). **(b):** A 3D visualization, modified from (Sengupta et al. 2012). *"In this figure, the pathlines of the blood flow are traced from the left atrium to the aorta (red-yellow) and from the right atrium to the pulmonary arteries (blue-turquoise) during a cardiac cycle."*

2.4 Computational Fluid Dynamics

This section covers the theoretical background for the assumptions, governing equations, discretization and numerical solvers which have been used in the CFD pipeline developed in this thesis.

The purpose of the numerical simulation is to describe a set of physical rules that governs the fluid movement inside a fluid domain in three dimensions with a time dependent inlet condition, time dependent outlet condition and time dependent boundary movement. These physical rules are described in partial differential equations (PDE's), and discretized in a way that can be solved by a computer in a numerical framework.

2.4.1 Fluid mechanics

The governing equation of the fluid is the Navier Stokes equation which in convective form, assuming constant dynamic viscosity μ, is expressed as:

$$\rho\left(\frac{\partial \vec{u}}{\partial t} + (\vec{u}\cdot\nabla)\vec{u}\right) = -\nabla p + \mu\nabla^2\vec{u} + \tfrac{1}{3}\mu\nabla(\nabla\cdot\vec{u}) + \rho\vec{g} \tag{2.1}$$

$$\frac{\partial \rho}{\partial t} + \nabla\cdot(\rho\vec{u}) = 0 \tag{2.2}$$

where ρ is the density, $\vec{u}$ us the fluid velocity vector, p is pressure, μ is dynamic viscosity, and $\vec{g}$ is the gravitational acceleration.

The compressible Navier Stokes equations in 2.1 and and 2.2 can be simplified by applying the following assumptions: incompressible flow, laminar flow, Newtonian fluid, negligible effect from gravity.

2.4.1.1 Assumptions and Simplifications

Incompressible flow means that ρ is constant. Since ρ does not change over time or space we have

$$\frac{\partial \rho}{\partial t} = 0 \quad , \quad \nabla\rho = 0 \tag{2.3}$$

from substituting 2.3 into the the continuity equation in 2.2, it follows:

$$\frac{\partial \rho}{\partial t} + \nabla\cdot(\rho\vec{u}) = 0 \quad \Rightarrow \quad \nabla\cdot\vec{u} = 0 \tag{2.4}$$

and from substituting 2.3 into the 2.1 a term is removed, leaving the Navier Stokes equations for incompressible fluid:

$$\rho\left(\frac{\partial\vec{u}}{\partial t}+(\vec{u}\cdot\nabla)\vec{u}\right)=-\nabla p+\mu\nabla^2\vec{u}+\rho\vec{g} \tag{2.5}$$

$$\nabla\cdot\vec{u}=0 \tag{2.6}$$

Laminar flow is a flow characteristic which can be expressed as "no two streamlines crossing", also sometimes referred to as the flow moving in sheaths or laminae. Opposed to laminar flow is turbulent flow, which requires some extra steps in the governing equation to solve. While equation 2.5 can solve turbulent flows, provided a super fine grid and computer- and time resources towards infinity. This means that 2.5 cannot realistically be applied on a turbulent flow. Turbulence can be modeled by adding terms to the equation system, however the definitions are out of the scope of this work. Since 2.5 can only solve laminar flow, it is an important assumption to define. To defend the assumption of laminar flow in a CFD, two things can be done: **1)** Determine experimentally by measuring the flow in a similar setting and assess turbulence. **2)** calculate Reynold's number for the flow under the relevant conditions. The Reynold's number is a non-dimensional number defined by the ratio of inertial forces to viscous forces. The larger Reynold's number is, the greater the chance of turbulent flow. There is no defined cutoff value, rather there is a transition interval. Furthermore this interval is different from system to system. I.e. different geometries. The Reynold's number where a system is transitional must be determined experimentally.

Reynold's number, or Re, is defined as:

$$Re=\frac{Inertial force}{Viscous force}=\frac{|\vec{u}|L}{\nu}=\frac{\rho|\vec{u}|L}{\mu} \tag{2.7}$$

While the Re at which the laminar-turbulent transition begins is depending on the system, the magnitude of Re is still a good indication. For the dynamic heart phantom (DHP) under the conditions described in [Paper 2] , the Re is calculated as:

$$Re=\frac{\rho|\vec{u}|L}{\mu} \tag{2.8}$$

$$=\frac{1037[\frac{kg}{m^3}]0.45[\frac{m}{s}]0.01[m]}{0.0041[Pa*s]} \tag{2.9}$$

$$=1138 \tag{2.10}$$

which is lower than the turbulent transition for a pipeflow (Fung 1990). This indicates that the flow could be laminar. Another indication of laminar flow is the fact that the numerical solver is able to find a solution. Solving for a laminar flow under conditions that should be turbulent can cause numerical errors.

Negligible gravity Since the effect of gravity is negligible, the body force term in 2.5 can be ignored. The final governing equation is:

$$\rho\left(\frac{\partial\vec{u}}{\partial t}+(\vec{u}\cdot\nabla)\vec{u}\right)=-\nabla p+\mu\nabla^2\vec{u} \tag{2.11}$$

$$\nabla\cdot\vec{u}=0 \tag{2.12}$$

Newtonian fluid A fluid being Newtonian means the shear stress to shear rate relationship is proportional. The proportionality factor is the coefficient of viscosity. In a non-Newtonian fluid the viscosity is a function of shear rate, or shear rate history. Note that "Newtonian" can be a fluid property, but a non-Newtonian fluid can behave as a Newtonian fluid under certain conditions. In that case the flow can be said to be Newtonian.

2.4.2 Discretization

This is the "Computational" part of CFD. Once the governing equations are defined for a system, they must be applied and solved. Some geometries are easily defined mathematically as surface expressions, or a collection of surface expressions, or patches, to represent a fluid domain. Simple geometries with assumptions, such as symmetry, can be solved analytically without the need for numerical methods. A famous example is the fully developed steady parabolic flow profile in a tube, also known as Poiseuille flow. By formulating the pipe geometry in a polar coordinate system and assuming no slip and rotational symmetry, the differential equation describing the flow profile is reduced to one dimension and can be solved by hand. For more complicated geometries, the problem must be reduced to a system of partial differential equations which is not feasible to solve by hand. A famous, and very early, description of a numerical framework for solving CFD was proposed before the era of digital computation by Lewis Fry Richardson in 1922 for weather forecasting. Here Richardson refers to a large number of people as "computers" that sit in a large room and calculate their own equations while passing information between neighbors. To make use of the "computers", the fluid domain must be split into smaller pieces with their own solutions and dependencies. The first step if discretization is meshing, which essentially splits the spatial domain into several smaller domains or "nodes". Governing equations are applied to each node, and the boundary conditions of each node is defined by the neighbor nodes or boundary conditions at domain boundaries. Mesh types will not be discussed in a broad sense, but the most common mesh elements are mentioned in the following paragraphs. The meshing approach applied to the pipeline is defined in chapter 6.

The next step in discretization is to define how the system of equations are formulated. Depending on the type of problem (solid, fluid, chemical, electromagnetic, etc.), one method might be better suited, and many variations exist of each method. The following is an overview.

Finite Difference works on regular grids, and is the simplest implementation of the three. The biggest disadvantage is in curved boundary handling, as the regular grid is not always intersecting precisely at the boundary if it is curved. Another disadvantage is the lack of ability to do local mesh refinement. The discretization works by estimating the differences at node levels.

Finite Element The finite element method is most generally applicable of the three, and is applicable to many types of physics which makes it great for multiphysics where several governing equations interact. It is easy to increase the order of the elements, which can increase the accuracy of the solution without the need to recalculate a refined mesh. This is an advantage for multiphysics, because it allows different orders for different types of physics while still keeping the coupling on the same mesh. Finite element is usually the hardest to implement of the three, and is often applied through commercial software.

Finite Volume The finite volume (FV) method is good for flux formulations, in that they solve an equilibrium based on surface integrals over "cells". In other words this method solves the "what comes in, must come out" equation. This is great for nonlinear problems as it automatically includes a looser formulation. FV is great for irregular grids / meshes as well which is a great advantage in biological shapes, and for local mesh refinement at volumes of interest. FV is not easy to make higher order, which is the case for FD and FE.

2.4.3 Verification and Validation

Every model needs validation to prove its accuracy. And whenever any parameter is changed more than a little, the specific problem must be verified. In short: Verification is checking "are we solving the equations right?" and validation is checking "are we solving the right equations?".

2.4.3.1 Verification

Verification in the context of "are we solving the equations right" is to test whether the model is independent on the numerical framework. At the very least, the solution should be independent of the discretization. This can be tested by performing a mesh independence study. A mesh independence study solves the same exact model with increasing number of degrees of freedom which is usually obtained by refining the mesh. Once the mesh is refined sufficiently, another mesh refinement should not change the solution much. This is why a mesh independence study is also referred to as a "mesh convergence study". Usually a significant scalar metric is chosen for comparison to produce a plot like in Fig. 2.10.

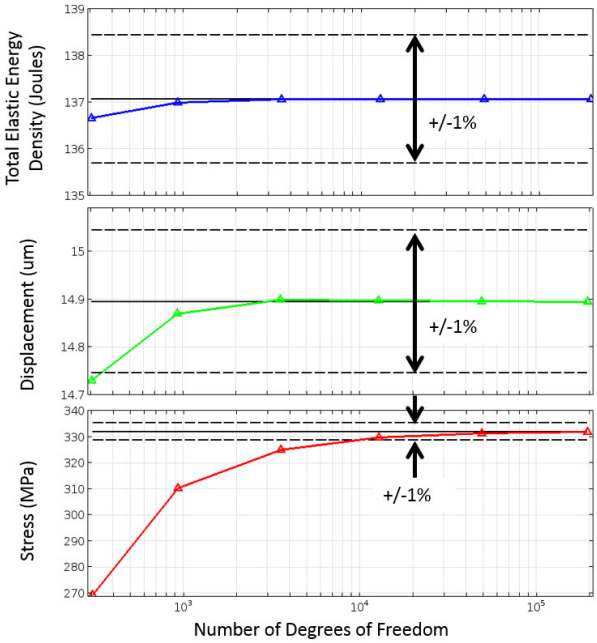

Figure 2.10: An example of how different metrics converge when the computational mesh is refined. Note that the different metrics converge at at different rate, and note that the rate of conversion is not directly depending on the number of degrees of freedom, but rather how the mesh is refined. Modified from (COMSOL Multiphysics 2017)

2.4.3.2 Validation

Validation in the context of "are we solving the right equations" is done by comparing the, now verified, simulated solution to its real world equivalent system. If the model is adequate, i.e. if it contains the right equations and boundary conditions, the simulation result should be similar to the measured ground truth from the real world system. Validation is an important part of this thesis.

2.4.4 The Arbitrary Lagrangian Eulerian formulation

With the system of equations set up, one thing still needs to be addressed, which is how to handle moving mesh nodes. Generally when working with moving solids, such as a bending beam or a deforming rubber gasket, the computational nodes are fixed to the material in a reference configuration and the mesh nodes move with the material deformation. Their position and orientation change relative to the "world" (spatial frame) coordinate system, but stay exactly the same relative to the reference configuration of

the material. This is an advantage for defining anisotropic material properties, as these become independent of the material orientation in the Lagrangian formulation. However, the Lagrangian formulation is no good for describing fluid flow, as it is a continuum, and it makes little sense to try and define the relationship between two particles as the deformations become very large. Instead, the Eulerian formulation is used, which describes physics in points/nodes which are fixed in space relative to the "world" (spatial frame) coordinate system. These nodes define what "material" goes through the point instead of following the movement. This is how equation 2.11 is defined. This approach is great for stationary fluid domains, even for time dependent flows, but is problematic once a moving boundary is introduced.

The solution is a combination of the two, called the arbitrary Lagrangian Eulerian (ALE) formulation, where Euler points are moved around like Lagrangian points. For this to work one must take into account the movement introduced by moving the Euler points around relative to the spatial coordinate system. This movement can be explained as the Euler nodes are going to experience changes in physics that are not caused by the fluid flow, but rather the movement itself. The PDE's (here: equations 2.11 and 2.12) assume no observer velocity, and therefore have to be corrected. This is done by modifying the convective term ($\vec{u} \cdot \nabla \vec{u}$) so it takes the mesh velocity, $\vec{u}_{mesh}$, into account. This results in the "ALE friendly" version of NSE:

$$\rho \left(\frac{\partial \vec{u}}{\partial t} + (\vec{u} - \vec{u}_{mesh}) \cdot \nabla \vec{u} \right) = -\nabla p + \mu \nabla \vec{u} + \rho \vec{g} \tag{2.13}$$

A word about coordinate systems As described in section 2.4.4, simulations of moving domains often require at least two coordinate systems; a "world coordinate system" that is unchanged over time, and a "material coordinate system" that describes the reference configuration of a material. When the material moves, the material coordinate system moves with it, relative to the spatial coordinate system. In this dissertation the naming conventions from COMSOL is used:
Spatial frame, written as (x, y, z), is the "world coordinate system"; fixed in space, and all material points move relative to this coordinate system. This can be thought of as a rigid and stationary.
Material frame, written as (X, Y, Z), is the reference configuration of the material. In the simulations presented in this dissertation, the spatial frame is equal to the material frame at t=0, where there is no deformation. The fluid domain is considered an elastic material, and its movement is defined relative to the spatial frame.
Other frames are defined in COMSOL, called geometry frame and mesh frame. These are however not directly in use for the simulations presented in this thesis.

2.5 Image registration

Image registration is any process that aligns two or more images by transforming them to the same coordinate system in a way that aligns landmarks or specific features from both images. Registration can be performed on 2D images as well as 3D volumes. Image registration is a critical tool for several tasks in medical imaging. These tasks can be divided into three topics (Sotiras, Davatzikos, and Paragios 2013).

- Merging images from different modalities to create multi-modality images.
- Comparing images of the same subject over time from a time series of images.
- Creating statistical atlases for population studies.

Furthermore the type of registration can be divided into inter-modality registration and intra-modality registration. The former is registering images from several imaging modalities, such as CT and MRI, and the latter is registering images of the same modality, such as CT to CT. Inter-modality registration introduces some unique challenges that are not present for intra-modality registration. These challenges occur because the contrast of the different modalities might present identical anatomical structures very differently. In this case the similarity metric must be chosen accordingly. For intra-modality registration, the similarity metric can often be as simple as evaluating the sum of difference at all pixels/voxels.

The registration task in this project falls under the time series category, however with a much shorter time between acquisitions than the usual case for same-subject registration which can have months, or even years, in between acquisitions. The time interval between acquisitions in this project is fractions of a second which naturally limits the registration type to intra-modality. The very short acquisition interval also means that the registration from one acquisition to another can be interpolated with a direct physical meaning to the time dimension. The same is in some sense also true for longer acquisition intervals, however the movement represented by the interpolation is representing changes over long time and is not physically meaningful as it does not represent the true movement of the subject.

2.5.1 Image registration - a 2D example on photographs

The photos and plots for this example are modified from MATLAB's documentation of the `imregdemons` function (imregdemons documentation, MathWorks 2022). The goal of this registration is to warp the right image in Fig. 2.11 so the hand is in the same pose as the hand in the left image. In this example, which is two monochrome 2D images, the difference can be plotted by comparing pixel intensity. This comparison is visualized in figure Fig. 2.12 where the left image is a comparison of the two images in Fig. 2.11 before warping, and the right image in Fig. 2.12 is a comparison of the same images after warping. Lastly inf Fig. 2.13 are seen the same images as in Fig. 2.11 after warping of the

image to the right. Compared to the unwarped image, the fingers are spread out a bit more, and they have been stretched to appear longer. Furthermore the image appear brighter than the unwarped image which is caused by a pre-processing step which is not directly a part of the registration itself. Note the borders of the warped image have been zero padded where the image borders have been displaced towards the center of the image.

Figure 2.11: Two monochrome images of the back of a hand laying flat on a surface. The position of the hands are not exactly identical. Modified from (imregdemons documentation, MathWorks 2022)

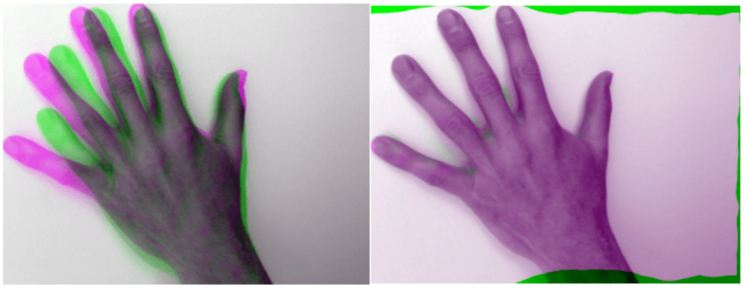

Figure 2.12: Left: The two images from Fig. 2.11 superimposed. Differences are highlighted with magenta and green. **Right:** Same as *left* but after one of the images has been warped using MATLAB's `imregdemons` function. Modified from (imregdemons documentation, MathWorks 2022)

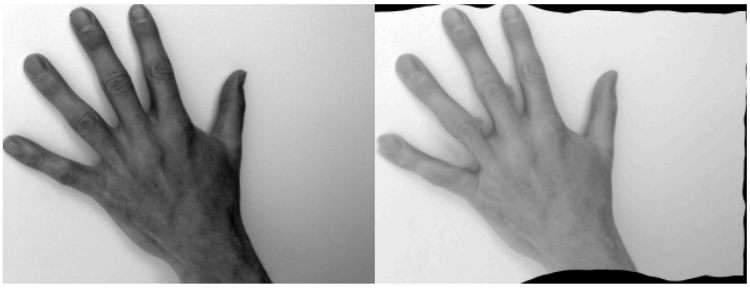

Figure 2.13: Left: The same image as the left image in Fig. 2.11 **Right:** The warped version of the right image in Fig. 2.11. Modified from (imregdemons documentation, MathWorks 2022)

2.5.2 Image registration - a 3D example on synthetic data

This registration example is based on a synthetic three dimensional dataset consisting of 20 isotropic volumes of binary scalar values. The volume background is zero values, and in the center of the volume is a sphere with varying radii. In Fig. 2.14 isosurfaces from two such volumes are plotted. Note the radius of the sphere in the left volume (i=1) is smaller than the radius of the sphere in the right volume (i=10).

A volumetric registration between the two spheres is performed by applying MATALB's `imregdemons` function. This results in a displacement field that warps one volume to match the other volume. In this case the volume with the smallest sphere is warped to match the larger sphere. The displacement field is three dimensional but only a two dimensional slice is plotted in Fig. 2.14(c).

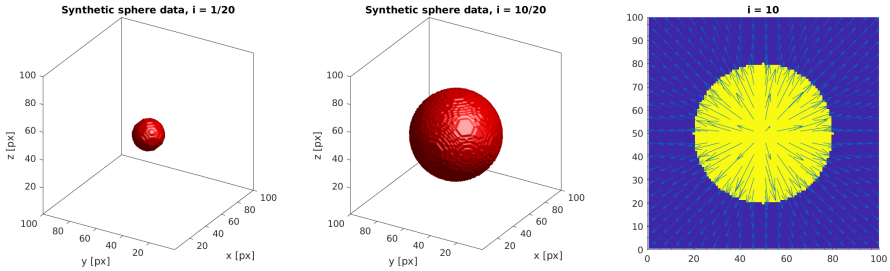

(a) (b) (c)

Figure 2.14: Two time instances from the synthetic dataset consisting of several cubic isotropic volumes of binary scalar values. The volume background is zero, and every time instance volume has a sphere in the center with varying radius. **(a):** Isosurface plot of the sphere in the first time index. **(b):** Isosurface plot of the sphere in the tenth time index. **(c):** 2D slice of the tenth volume where dark blue is background (0), and yellow is the sphere (1). The light blue arrows indicate the displacement the sphere in *(a)* undergoes to be registered onto the sphere in *(b)*. These arrows are the displacement field.

2.5.3 Transformation Model

Image registration is realized by warping a *moving* image to a *fixed* image. The warping is achieved by a transformation. The type of transformation, the transformation model, should be selected based on the expected movement. A rigid transform is suitable for aligning two images of the same object under the same conditions. An example where a rigid transform is the right choice is the alignment of two cranial CT images of the same subject. In most cases the cranium is not deformed, and a rigid transform suffices. In fact using a transformation model with more parameters might enable the registration to result in a displacement which is physically impossible based on prior knowledge.

Parametric transformation models are not necessarily rigid. A parametric model which is elastic is presented in (Hvid 2018). The movement in this model is based on the works of (Evans, Bloor, and Wilson 2001). The three parameters in this transformation model are axial contraction, radial contraction, and axial rotation. These are illustrated in Fig. 2.15.

Opposed to parametric transformation models are free transformation models. These can be viewed as a parametric transformation with a very high number of parameters. The transformation can be described using splines or, in the most "free" form, a displacement vector for each pixel/voxel. The vectors are however not necessarily independent as this could lead to overlaps and other undesired properties. The displacement resulting from the diffeomorphic demons algorithm is a free displacement which is smooth. In

`imregdemons` the smoothness can be given as an input and should be based on prior knowledge.

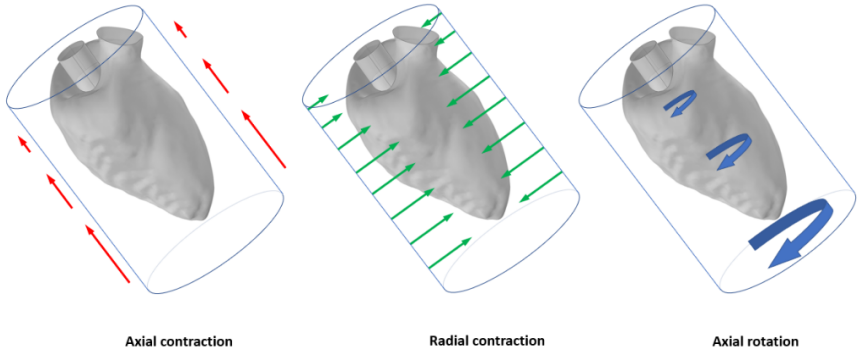

Figure 2.15: Illustration of a 3D parametric deformation model for human left ventricle by three parameters: axial contraction, radial contraction, and axial rotation. The illustration is modified from (Hvid 2018).

2.5.4 Similarity Metric

The similarity metric can be viewed as the "cost function" to optimize in a registration. Different metrics exist for different cases.

The simplest metric is to align control points that have been manually selected in both images (*fixed* and *moving*). Now the *moving* image is transformed, or warped, using the given transformation model until the mean distance between control points is minimized. Optimization methods are out of scope for this thesis. It should however be noted that the methods are often numerical, and that several solutions often exist. The optimization increases in complexity and computational demand with an increasing number of parameters. Usually similarity metrics are divided into intensity-based and feature-based.

Intensity based similarity metrics are mostly applicable for intra-modality registration as the same structures can be expected to have a similar voxel intensity regardless of position. CT is a great example of this, because the unit of CT images is HU which is an absolute unit describing an attenuation coefficient calibrated to water and air. Therefore intensity-based similarity metrics are often a good choice for registering CT to CT. Note however that the magnitude of intensity will impact the weight of the metric unless corrected. Therefore something with a high intensity contrast will be prioritized over something with a low intensity contrast by an intensity-based metric. The metric can of course be written to prioritize contrast in a given intensity window.

For inter-modality registration intensity based similarity metrics will most likely fail because each modality shows different contrasts. As an example a T1 weighted MRI shows water as a low voxel intensity where a T2 weighted MRI shows water as a high voxel intensity. In these cases feature-based similarity metrics perform better. Feature based metrics are however more complicated and often need to be specified according to the specific features and modalities in question.

2.5.5 Registration on multiple sequential image volumes

For simplicity registration has been described between two 2D images to this point. Mathematically speaking, going from 2D-2D registration to 3D-3D registration is trivial, however computational complexity increases rapidly due to the curse of dimensionality. Computational schemes and optimization strategies for registration is out of the scope of this thesis since available tools exist to solve this problem to a sufficient degree. This thesis utilizes the MATLAB function `imregdemons` which supports GPU acceleration and is implemented in a parallelizable method to decrease computation time.

Furthermore registration has been described as registration between a single image volume to another single image volume, however in the presented pipeline there are 20 time sequential volumes. Depending on the purpose registration on a sequential time series of volumes can be achieved in several ways. Several publications have suggested methods applicable to the human heart with different goals in mind; (Peyrat et al. 2010) for CTA and (Craene et al. 2012) for US strain detection. The difficulty in registering a time series of volumes is to incorporate all known information, as all volumes are inter-dependent. The registration approach can either register each volume to its neighbor volumes, or register one volume to all other volumes. Another approach is to perform registration directly on the temporal dimension like presented in (Peyrat et al. 2010) which essentially is an approach that takes advantage of the entire dataset.

Independently of the temporal registration method, the representation of the registration should be in the form of a displacement field $\vec{d}(\vec{X}, t)$, defined as:

$$\vec{d}(\vec{X}, t) = \begin{bmatrix} d_x(X, Y, Z, t) \\ d_y(X, Y, Z, t) \\ d_z(X, Y, Z, t) \end{bmatrix} \tag{2.14}$$

where the coordinate system notation follows COMSOL's conventions as described in section 2.4.4. Note that the subscript of each component of the displacement vector in equation 2.14 is lowercase. This signifies that the direction of the displacement is defined in the spatial frame; not to be confused with the material frame where the location of the displacement is defined.

The required specifications for the displacement field are discussed below.

2.5.5.1 Representation of displacement field

For the displacement field to be suitable in the presented pipeline several requirements have to be met. The requirements are listed and discussed briefly. In the presented pipeline, any displacement field that fulfills these requirements can be substituted directly in as described in chapter 3.

A displacement field is defined in this thesis as a 3D+t space where displacement is defined for each direction in the spatial frame (x, y, z) in any arbitrarily chosen point in the material frame (X, Y, Z) and time (t) within the span of the 3D+t space which is the bounding box of the ventricle. A displacement field like this can be represented in several ways. This could be a parametric transformation with time dependent parameters, or even as a sum of spatiotemporal B-Spline kernels, see (Craene et al. 2012). Using functions, or a sum of functions, has the advantage that continuity can be controlled by the choice of functions. This is the approach in the displacement fields in (Hvid 2018) and [Paper 1] , however these time dependent parameters were not estimated from imaging. Although these displacement fields could have been estimated from a registration based on a parametric transformation model. This would however introduce a risk of oversimplifying the movement. The numbers of degrees of freedom in a parametric displacement field is reduced to the number of parameters. Therefore the functions might unintended constraint some of the very displacements that are being investigated in the first place.

A simple example of a continuous displacement field is a rigid transform with time dependent parameters. A rigid transform can be thought of as a parametric transformation model with six degrees of freedom; translation in three dimensions and rotation in three dimensions. These six numbers provide a displacement in one time instance. Were each of these six parameters is defined as a continuous function, it would fit the definition of a continuous displacement field. A time dependent rigid transform like this is however too constrained to describe the cardiac movement.

Using a time dependent free deformation transformation model does enable all movement to be described, provided the right functions. However this would require a time dependent function for displacement in each direction in the spatial frame, x, y, z, for each voxel in the 3D space. Furthermore these must be reasonably smooth in space and continuous in time.

Discrete representation A continuous displacement field can be represented discretely by sampling the 3D+t space, however a discrete displacement field cannot necessarily be represented as a continuous displacement field. If a discrete displacement field is obtained, which indeed is a sampling of a continuous displacement field with adequate sampling density, the discrete displacement field can be expressed continuously by either approximating the discrete displacement field with a number of functions or the discrete displacement field is interpolated in a way that makes it continuous even though it is not expressed analytically. Note that this is only possible if the discrete data is obtained from

a continuous dataset. Otherwise smoothing, which would result in loss of data, would be necessary.

A discrete representation of the displacement field is essentially like a model based transform with as many degrees of freedom as voxels times three, one for each direction of the displacement, see 2.14. This is the most general way of defining a displacement field without loss of information. The downsides of using a discrete displacement field is the potentially large amounts of data (and data not used) which can lead to performance issues during interpolation by requiring more memory, more CPU hours, or both. A discrete displacement in the context of this thesis is defined as $\vec{d}(\vec{X}, t)$, see (2.14).

Cyclic displacement The CFD simulation in the pipeline is run for several cycles. Therefore the displacement must be cyclic. Even if the 4D input image is cyclic per definition, a small numerical error in registration could cause issues when running the simulation for more than a single cycle. This requirement can be defined by considering an arbitrary point in the material frame. In this arbitrary point two things must be true: 1) The displacement must be equal at the first time instance and the last time instance. 2) The first time derivative of displacement, the displacement velocity, must be equal at the first and last time instance.

If these two conditions are not true, the initial conditions for heart cycle number 2, and all following heart cycles, will be ill-posed, and the solution will most likely not converge.

Smooth displacements The displacement field from a DD algorithm registration is inherently spatially smooth from the nature of the diffeomorphic demons (DD) algorithm ((Thirion 1998; Vercauteren et al. 2009)). As each registration is independent of each other the temporal smoothness is not guaranteed. To assure temporal smoothness a sliding window is applied over the temporal dimension of the displacement field. Another way of ensuring smoothness is in the choice of interpolation method of a discrete displacement field. Choosing, for example, cubic spline interpolation is going to ensure the first order derivatives are continuous. This is not guaranteed in a linear interpolation. Cubic spline interpolation does come with the risk of overshooting and a significant increase in memory requirement. A 4D displacement field of the size in this thesis could easily require several hundred gigabytes of memory to interpolate with a cubic spline in MATLAB. However with a reasonably smooth initial displacement field with a reasonably good spatiotemporal sampling rate in combination with applying the sliding smoothing window in the temporal dimension, linear interpolation can be applied with success.

2.5.5.2 Alternative Registration Approaches

The pipeline CFD takes a moving surface as input. Therefore the method of obtaining this representation can be substituted by any method that represents the endocardium correctly. The more accurate the input is, the more accurate the output can be expected. Some alternative approaches are mentioned and referenced here.

A good overview of the existing cardiac registration strategies is presented in (Makela et al. 2002). This overview focuses on all types of registration, including rigid inter-modality transforms which is not suitable for the purpose of this thesis. A review of shape based registration is presented in (Tavakoli and Amini 2013). An example of a registration approach focused on intra-modality spatiotemporal registration on CTA is presented in (Peyrat et al. 2010) which treats time as a dimension in the registration, using the information that all volumes are consecutive time instances. A similar method optimized for US motion and strain quantification is presented by (Craene et al. 2012). Another option is utilizing a machine learning based approaches which is discussed in (O'Regan 2020).

Obtaining movement without using a registration approach is also an option worth mentioning. Techniques exist that can measure the movement of the myocardium directly. This includes implantation of markers to be tracked, but can also be achieved in a less invasive manner by a technique called cardiac magnetic resonance (CMR) tagging. This technique "tags" regions of the myocardium and is able to track the tagged regions in a short period of time, thereby extracting the actual movement. These techniques are discussed in a review by (Ibrahim 2011).

Part II

The Pipeline

CHAPTER 3

The Pipeline

This chapter is a high level description of the CFD pipeline to provide a general overview and a reference. The function of each major part of the pipeline is outlined and the input/output requirements for each major part of the pipeline is defined in the end of each section. The technical implementation details of registration and CFD are described in separate chapters (Chapter 5 and Chapter 6).

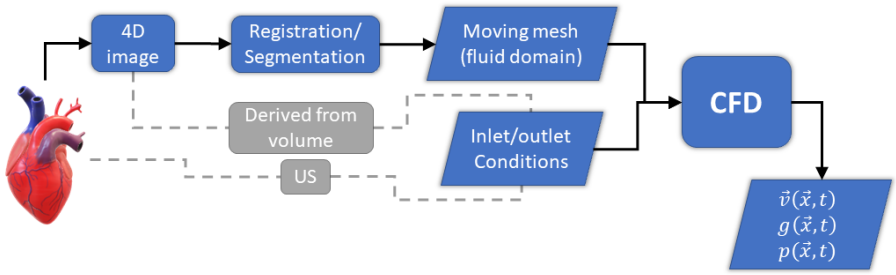

Figure 3.1: Flowchart of the CFD inputs and outputs. Rectangular boxes are actions, slanted boxes are data. Gray indicates either/or. The pipeline output is a three-dimensional time-dependent velocity field $\vec{v}(\vec{x},t)$, and pressure field $p(\vec{x},t)$ inside a moving geometry expressed by $g(\vec{x},t)$

The aim of the pipeline is to produce a time dependent velocity field that accurately represents the intra ventricular blood flow patterns from 4D medical imaging. Ideally the finished pipeline can be automated to a degree where it can be thought of as "a button that a clinician can push" to produce the time dependent velocity field from a 4D image of the heart. As described in the background Section (2.2) there are many ways of approaching this goal. The presented pipeline is based on: geometry prescribed CFD, ALE formulation, finite element modeling (FEM), inlet as velocity boundary condition, outlet as pressure boundary condition.

Based on these choices the pipeline can be divided into the processes of: acquiring 4D data, extracting the moving boundary of the ventricle, defining inlet/outlet conditions, and lastly applying the acquired data as boundary conditions to the simulation. These

processes are illustrated in a flowchart in Fig. 3.1.

In the current iteration of the pipeline the heart valves are not modeled directly. The effect of the valves can be incorporated to the pipeline by capturing the inlet velocity field which naturally is a direct result of the valve. This could be done with US VFI, but would of course require additional acquisitions on the patient.

3.1 4D Imaging

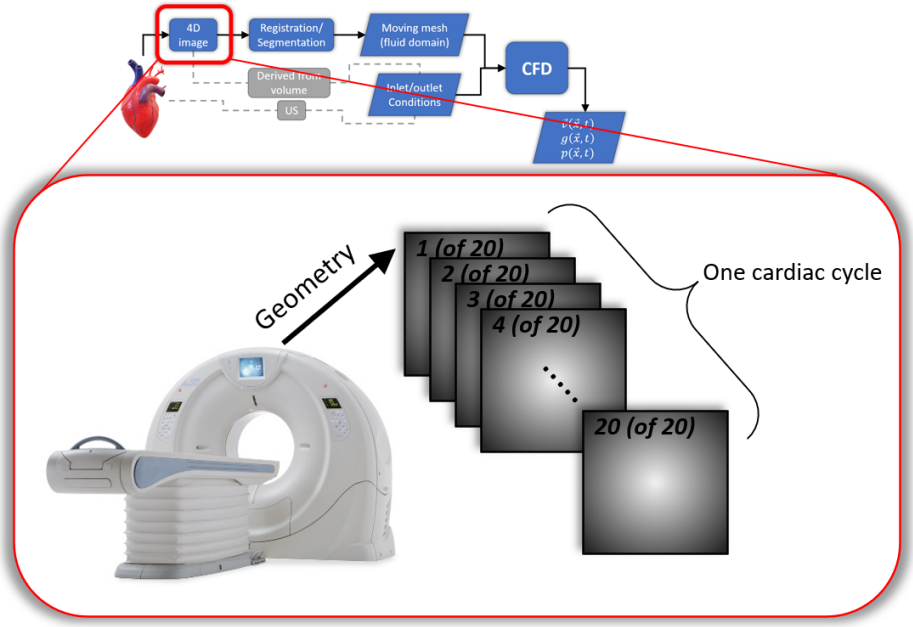

Figure 3.2: Illustration of the CTA output form. Each square represents a volume at a given time instance in the cardiac cycle.

The 4D imaging in figures 3.1 and 3.2 is defined in this thesis as output from any imaging technique that produces sequential 3D volumes as a function of time with a regular time interval. Such "4D image" is represented discretely as a matrix with the dimensions $N\ x\ M\ x\ P\ x\ T$ where $N\ x\ M\ x\ P$ express voxel intensities on an isotropic grid, at a given point in time indexed by T with a regular time interval. See Fig. 3.2.

Generally, temporal resolution is an important factor to take into consideration. it should be noted that temporal resolution is not necessarily equal to volume rate, as the time of acquisition for each volume is what determines the maximum velocity of the

motion which can be captured. Of course, the volume rate still has to at least satisfy the Nyquist theorem. CTA is easily capable of exceeding the Nyquist frequency for the large movements of the human ventricles. Assuming the ventricle movement in a heartbeat roughly has the shape of a sine wave, the Nyquist frequency is "half a heartbeat". This corresponds to (more than) two samples per heart beat. Considering CTA is capable of sampling a single heartbeat into 20 volumes (see Section 2.3.2.1) this volume rate is almost an order of magnitude above the Nyquist frequency. Of course the heart does not move exactly like a sine wave. Faster movement and higher frequencies are especially seen at the heart valves which are also hard to image with CTA due to the spatial resolution of CTA. For the purpose of this pipeline it makes sense to not have overlapping acquisition of volumes, meaning that the acquisition time should be less than the inverse of the volume rate. Spatial resolution is covered in Section 2.3. As the 4D image is being used as input for a cyclic simulation, the movement must be cyclic. In practice this means that the anatomical displacement between the first volume (at t_0) and the last volume (at t_{N-1}) should not be larger than between any two sequential volumes i.e. between volumes at t_n and at t_{n-1}.

As the output format from a medical scan is typically DICOM, post-processing is necessary before using the 4D image as an input to the pipeline. Post-processing is performed in MATLAB and includes stacking the individual slices to 3D volumes and sorting the order of the timestamps (also referred to as "phases"). Furthermore the physical coordinates should be determined from the DICOM headers before interpolating onto an isotropic 3D grid. Furthermore the contrast is enhanced by a linear pixel process, i.e. histogram stretching, and lastly the values are converted to a 4D matrix of 8-bit unsigned integers.

4D Imaging input requirements Any subject to be studied must resemble the human heart in these regards: must have at least one cyclically moving cavity, the cavity(ies) must have an inlet and an outlet. Depending on the imaging modality the subject to be studied must be able to produce an electrical signal with a distinctive peak at the same time of in each cycle. In a human subject this corresponds to the ECG R-peak, in the DHP this is the simulated ECG.

4D Imaging output requirements A 4D image suitable for this pipeline must be a 4D matrix with sufficient contrast for imaging the ventricles. The spatial resolution should be sub-millimeter in all directions, and the temporal resolution should be at least 20 non-overlapping acquisitions per heart cycle. The 4D image should be interpolated in an isotropic grid before applied to the pipeline. For the best result with this iteration of the pipeline the voxel intensity between volumes should be comparable. This is the case with most 4D CTA, but not always the case for 4D MRI where either pre processing or a change in the registration similarity metric could be necessary. In addition to the 4D image matrix, three 3D matrices should be created to define the physical coordinates in

the unit [m] as floats. Lastly an array containing the physical time stamps of each volume which can be derived from the DICOM header data.

3.2 Registration/Segmentation

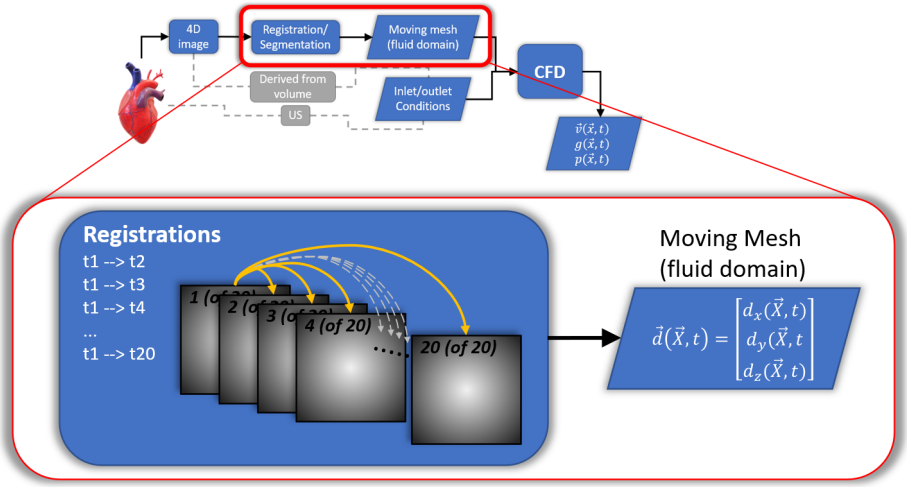

Figure 3.3: An expansion of the registration block in the flowchart in 3.1 and 8.1. The squares represent volumes similar to the squares in Fig. 3.2.

This part of the pipeline has two separate tasks. They are depicted as a single step because they work together to achieve the single goal of extracting a moving geometry from the 4D image.

3.2.1 Segmentation

Segmentation is defined in this thesis as the process of extracting a 3D surface from a 3D image. This corresponds to a single point in time. Therefore, by this definition, a segmented surface is static and only represents the geometry at a single point in time. A 4D image represented by a matrix of the size $NxMxPxT$ can have T individual surfaces segmented. With a sufficiently high volume rate these segmentation surfaces can be plotted sequentially as frames in an animation with the illusion of having a single moving surface. However this perceived movement is still useless as simulation input which is why the steps described below in Section 3.2.2 are necessary. In this pipeline such a surface is represented discretely as STL meshes (see Fig. 5.1).

Segmentation input requirements The input for segmentation should preferably be the same 4D image as the input for the registration to ensure the coordinates match. Note that the segmentation is only necessary for a single point in time which is usually the first 3D volume. The 3D volume must of course have sufficient spatial resolution and contrast between the ventricle and surrounding tissue.

Segmentation output requirements A segmentation of a single ventricle (left or right) performed on a single volume (one point in time), resulting in a single watertight surface represented discretely as a mesh in STL format. Note that the segmentation should be performed on the first volume of the same 4D image as the registration is performed to ensure the resulting displacement field from the registration applies directly to the segmented surface.

3.2.2 Registration

Movement can be imitated from a series of sequential surface meshes by considering them as "frames" in an animation. The segmented surfaces in this example are however independent, and the "animation" is only creating an illusion of a moving surface from a series of T independent surfaces. The geometry prescribed CFD pipeline requires a single moving surface with point-to-point correspondence which the "animation" example cannot provide. Furthermore the movement must be continuous and cyclic. This can be obtained in several ways which are discussed in Chapter 5. The presented pipeline estimates the movement of a surface segmented from a single volume by warping the same volume to match all other volumes individually using 3D image registration. This is illustrated in Fig. 3.3. The registration is implemented in MATLAB using the `imregdemons` function. The output from this registration is a discrete displacement field describing the displacement of each voxel in each direction (x, y, z) at each time point. This displacement field can be applied on the segmented surface from the same volume, resulting in a single surface. To achieve a continuous displacement field the field is smoothed temporally and interpolated smoothly. If the movement is not cyclic at this point, regularization can be added. See chapter 5.

Registration input requirement Preferably the same 4D image the segmentation was performed on. Otherwise the coordinate systems need to be aligned. Each 3D volume (time instance) must be isotropic to make sure deformation in all directions are weighted equally. The voxel intensities must be comparable for all 3D volumes. Otherwise it might be necessary to either pre-process the 4D image or use a feature based similarity metric in the registration instead of voxel intensity based.

Registration output requirement Ideally a continuous displacement field as described in equation (2.14). In reality the pipeline interpolates a discrete displacement field which can be represented as a 5D matrix of the size: `(N)x(M)x(P)x(T+1)(3)` where N,M

and P are number of voxels in the x, y and z directions, and T is the number of time instances. The `+1` in this dimension is because the first time instance is appended to make the displacement field cyclic. Note that temporal smoothing and regularization might be necessary. See chapter 5. This is illustrated in the flowchart in Fig. 3.3 in a parallelogram, which in the flowchart represents data.

3.3 Boundary Conditions

A simulation is only as good as the simulation inputs. The pipeline itself is only a method for processing inputs to provide a desired result output. The geometry and it's corresponding boundary conditions are the only information the simulation pipeline has to estimate the flow patterns. Obtaining accurate boundary conditions is therefore just as important as the simulation itself, it not more important. The three boundary domains; wall, inlet, and outlet, are shown on two example geometries in Fig. 3.4.

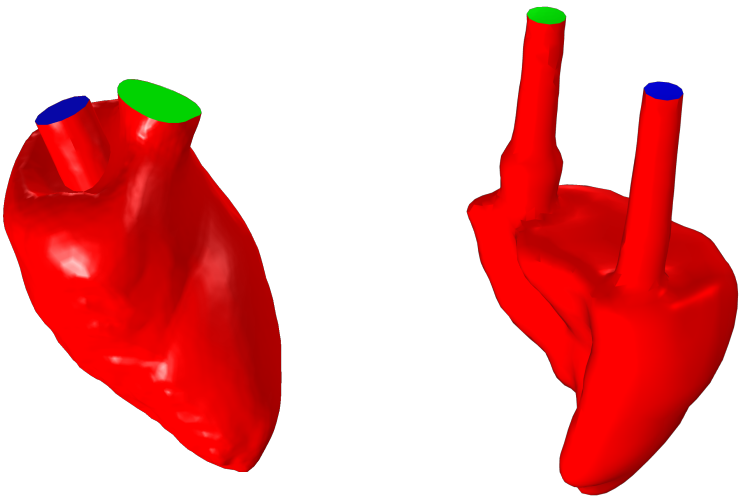

Figure 3.4: Two ventricle geometries with boundary type annotation. The geometries are not plotted to same scale. **Red:** wall, **Blue:** inlet, **Green:** outlet. **Left:** Left ventricle from simulations in (Hvid 2018). This geometry is obtained from the segmentation in Fig. 5.2. **Right:** Right dynamic heart phantom ventricle from simulations in [Paper 2] . This geometry is obtained from segmentation of the data presented in Section 7.1.1

3.3.1 Wall Boundary Condition

The wall boundary condition in the pipeline is "no slip". This means that at wall:

$$\vec{u}_{blood} = \vec{u}_{mesh}$$

This is handled automatically in the newest releases of COMSOL, which detects the mesh velocity at the boundary automatically when "no slip" boundary condition is set.

Wall BC input requirements The wall BC is defined by applying displacement from the temporal displacement field obtained by volumetric image registration to the surface of the reference geometry obtained by image segmentation.

3.3.2 Inlet Boundary Condition

The inlet boundary condition is flow velocity defined by three dimensional, time dependent vectors on the inlet boundary surface. This does not take the valve mechanics into account directly, however valve aperture can be represented by prescribing zero flow. This is possible for a fully closed heart valve as well as a partially closed heart valve. In this way the dynamics of the heart valves can be accounted for indirectly. In the presented phantom study the flow direction can be assumed to be perpendicular to the inlet surface.

The effect of boundary conditions at the inlet in CFD of the left ventricle was investigated in a master project in collaboration with this project. The project investigated the differences by applying the inlet flow directly at the mitral valve and comparing to applying inlet flow through a simulated extended tube. See (Petersen 2019). This question is further investigated in (Su et al. 2019) which compares the extended tube method with a realistic geometry of the left atrium.

Inlet BC input requirements Stationary surface of temporal 3D vectors representing flow velocity. This can be simplified by assuming perpendicular plug flow in a flat plane with known area and prescribing a 1D volume flow function of time.

3.3.3 Outlet Boundary Condition

Because the CFD simulation models incompressible fluid in a non-compliant geometry with an inlet defined either by velocity or volume flow rate, the outlet volume flow rate must match the inlet volume flow rate plus the volume change of the ventricle. Even if it does, numerical error might cause problems. This is solved by applying a pressure condition at the outlet. The way the pipeline simulation is set up makes absolute pressure values insignificant to the final flow patterns. What matters is pressure gradients and pressure change over time. Therefore the outlet boundary condition can be defined as a constant pressure of 0 Pa. It should be noted again that any constant would produce the same flow patterns and pressure differences.

3.4 CFD

The CFD is set up and run in COMSOL Multiphysics version 5.6 (COMSOL AB Stockholm, Sweden). The process of setting up the CFD requires multiple steps which are defined further in Chapter 6. The most important steps for setting up the simulation are importing BC's, importing geometry, importing displacement field, defining and generating computational meshes, defining domains, and defining physics in the given domains.

Generally the CFD can be viewed as a black box that fulfill the following requirements:

CFD input requirements Moving surface represented by STL and corresponding displacement field. Since the field is not strictly continuous, a function for interpolating the field as well as regularize the movement is also necessary. Inlet and outlet conditions must be as specified above. Furthermore the fluid properties of blood must be specified.

CFD output requirements Time dependent velocity field and pressure field inside moving domain, including a definition of the moving domain as a function of time. As illustrated in Fig. 3.1.

In the presented pipeline the CFD is defined as described above but is solved in three separate simulations or "studies".
The first part is a study that calculates the cyclic mesh movement according to the displacement field at discrete time intervals for the entire cycle. The movement in all other studies will be interpolated from this solution.
The second part is a stationary fluid simulation that provides a better posed initial condition for the third part. This is achieved by running several simulations starting with a "zero flow" solution and then incrementally increasing the inlet flow condition towards the initial condition of the final simulation, reusing the last solution for every step.
The third part is running the simulation with the movement from the first part and initial conditions from the second part. This simulation is repeated for several cycles, using the last time frame of one cycle as initial conditions for the first time frame of the next cycle until the solution between cycles converges.

CHAPTER 4

Dynamic Heart Phantom

This chapter provides a description of the dynamic heart phantom used for validation of the pipeline. The phantom is a specialized tool with many moving parts. Understanding how it works, what to maintain, and verify correct operation has been vital to the project. The description here includes a general description of the dynamic heart phantom, how it is programmed, and the issues encountered during the project.

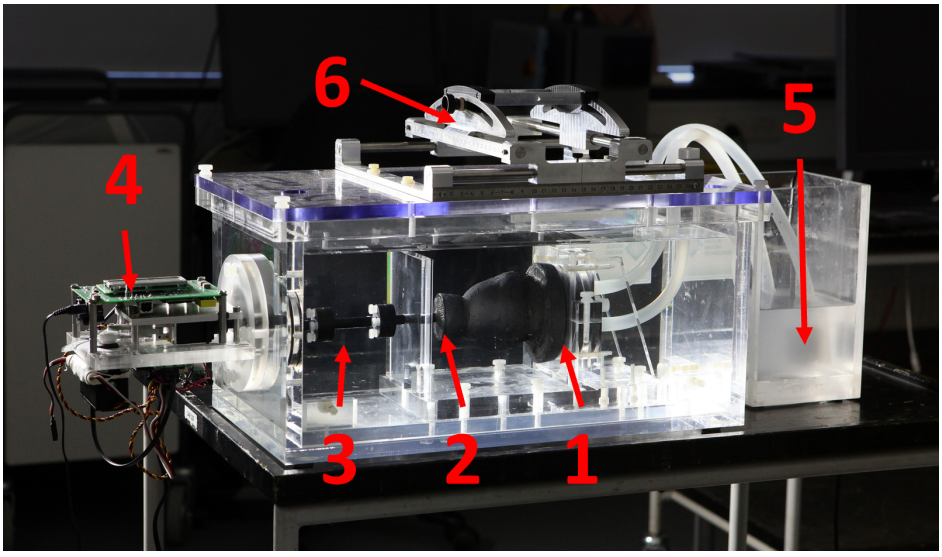

Figure 4.1: Photograph of the DHP, modified from [Paper 2] . **1:** Base of the heart phantom with inlet and outlet tubing. **2:** Apex of the DHP. **3:** Actuator rod for transfer of motion. **4:** Servo motors and micro-controller to apply the motion. **5:** Fluid reservoir. **6:** Fixture for the ultrasound probe where angle and position is adjusted.

The Shelley DHP-01 (Dynamic Heart Phantom) is a two-ventricle phantom of the human heart developed by Shelley Medical Imaging Technologies (Toronto, Canada). The two ventricle cavities (left and right) are anatomically realistic. Each of the ventricles have two tube connectors where the heart valves would have been located. The phantom ventricles are made of polyvinyl alcohol (PVA) with additives. The additives make the

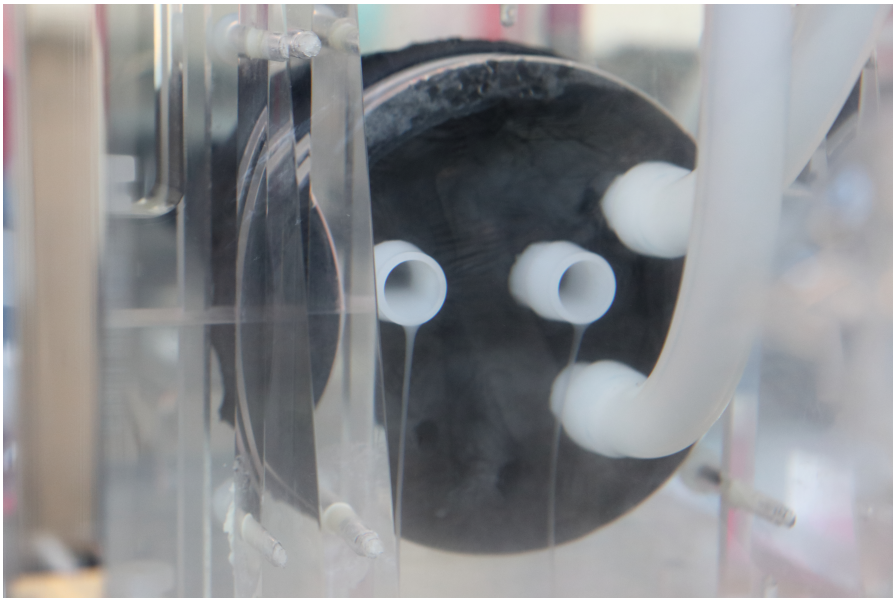

Figure 4.2: DHP inlet/outlet connectors. Tubes are connected to the LV, pumping BMF. The BMF leaking from the RV is caused by a defect in the phantom.

ventricles appear as myocardium on computed tomography (CT) and ultrasound (US). The PVA heart is submerged into a water-filled tank and anchored at the base. See Fig. 4.1.

An actuator rod is attached to the apex of the PVA heart. Two servo motors are attached to the actuator rod, one pushing the rod (compression) and one rotating the rod (torsion). The servo movement is programmed on a micro-controller which has three default output channels: compression, torsion and electrocardiography (ECG) output.

4.1 Programming the DHP

The heart phantom is controlled by programming a proprietary microcontroller called a Remote Advanced Playback Unit (RAPU), using a proprietary software developed by (Brookshire Software LLC 2022), called Visual Show Automation (VSA).

The VSA software is a graphical user interface meant for synchronization of servo motors and audio files. Movement is prescribed as "events" and are visualized in the VSA GUI. These events can be imported from a `.txt` file using an event based syntax. Multiple event types exist, but they are all different ways of defining linear movement given by start time index, stop time index, start value, and stop value. The sample rate is constricted to either 20 Hz or 30 Hz. All movement defined for this project is 30 Hz. A

Table 4.1: An example of how the phantom setup can be formalized with functions. The functions here were formulated in MATLAB and converted to a .txt file in the "event format" that VSA requires. In the current version the flow function is not being prescribed. Modified from [Paper 1] .

Function name	Function expression
Flow(t)	$5l/min$
Compression(t)	$sin(\pi t/T)^2 \cdot maxDisp$
Torsion(t)	0^o
ECG(t)	$\begin{cases} 1 & \text{if}(n \cdot T) \leq t \leq (n \cdot T + 0.1s) \\ 0 & \text{otherwise} \end{cases}$
for	$n = 0, 1, ..., N_{cycles}$ $T = 0.8s$

set of MATLAB functions were defined for converting arbitrary functions into piecewise linear functions and exporting them into a `.txt` file in the VSA event syntax. See table 4.1 and Fig. 4.3 for an example of input functions. The compression values were converted to servo values before exporting the functions. The servo value is an unsigned integer that represents the target angle of the servo motor. The relationship between the compression value and the servo value is based on the geometry of the mechanical coupling and the scaling of the integer. A MATALB function was created for this purpose as well.

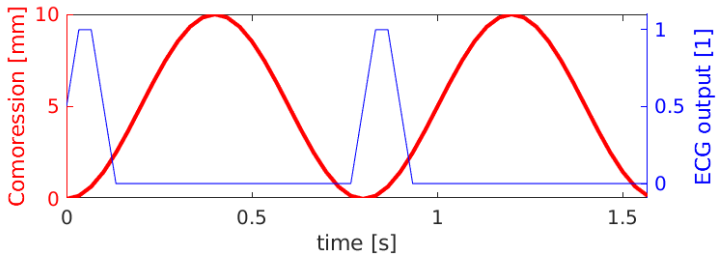

Figure 4.3: Two cycles of the compression and ECG functions applied to the DHP from table 4.1.

4.2 DHP Setup Elements

4.2.1 Repairs

As the current version is in a non-functioning state, repairs are the first step of any future plan. Creating new PVA phantoms that fit into the existing cradle and actuator system is being evaluated. Many advantages would follow, such as more control, modularity,

expandability by adding valves and other attachments. The obvious disadvantage is that it has to be designed, manufactured and maintained.

4.2.2 Visual Show Automation

A new version of VSA, VSA v6.0, has become available since last programming. The new version has new features that would ease the workflow. Especially since the old version is only supported in the outdated OS Windows 7. The RAPU has several more output channels, allowing for controlling a synchronized flow pump or a valve or even triggering an imaging system like US acquisition or a robot arm. Future setups should include imaging triggering of the ultrasound system as well as temporal flowpump waveforms that are synchronized with the motion, because everything is prescribed from same microcontroller. This is all possible in the new setup because of the rigid tubing.

4.2.3 Flow Pump

As discussed in [Paper 2] the utilized DC pump caused some issues which could be avoided by using a gear head pump which is capable of calibration and is not as sensitive to afterload. A such gear head flow pump is incorporated into the new phantom setup described in Section 4.2.6. This adds to the flexibility of the setup by adding an adjustable volume flow rate, and to the precision of the experiment by adding a calibrated volume flow rate which is much less sensitive to afterload compared to the currently used DC pump. The volume flow rate can be prescribed from a pulse width modulation (PWM) signal, and could potentially be controlled by the same sequence as the phantom movement and simulated ECG output. This is possible due to the new setup which utilizes rigid tubing. See Section 4.2.6.

4.2.4 Sliding fixture

The sliding fixture, as seen in Fig. 4.1, is a mounting system for ultrasound probes. The fixture is mounted on the top lid of the DHP tank and places the transducer part of the ultrasound probe under the water surface. The fixture has a linear translational stage in the XY-plane, parallel to the ground, with millimeter tick-marks for spatial reference. Furthermore the probe can be rotated around the y-axis with the center of rotation corresponding roughly to the actuator rod. See numbers 3 and 6 in Fig. 4.1. The sliding fixture is the first implementation of the system for controlled US measurement of the DHP. For more advanced measurements the UR3 robot arm will be used instead which has 6 degrees of freedom and is easier to calibrate to different purposes.

4.2.5 Robot arm

The robot arm is an upgrade on the sliding fixture, and is therefore an upgrade to the VFI acquisition only. Using the robot arm for acquisition allows for more degrees of freedom than the fixture does, as well as increasing the precision because the user is no longer

required to adjust positions manually by reading the positions on a ruler. This would be a powerful tool for obtaining several ultrasound measurements with precise spatial information in arbitrary directions, compared to the fixture which required re-mounting for obtaining orthogonal planes. See Fig. 4.4. The robot arm too, is incorporated into the new setup, see Section 4.2.6. The robot arm is controllable from MATLAB. If the image acquisition can be controlled from MATLAB as well, it wold be possible to automate some of the acquisitions, enabling higher precision in obtaining 3D geometry from B-mode ultrasound. This was tested by (Zaja 2020) and resulted in the CAD model seen in Fig. 4.5. This was obtained without automatic image acquisition though. Controlling the acquisition from MATLAB would also enable retrospective gating based on the DHP ECG signal which could make the acquisition easier and more reliable.

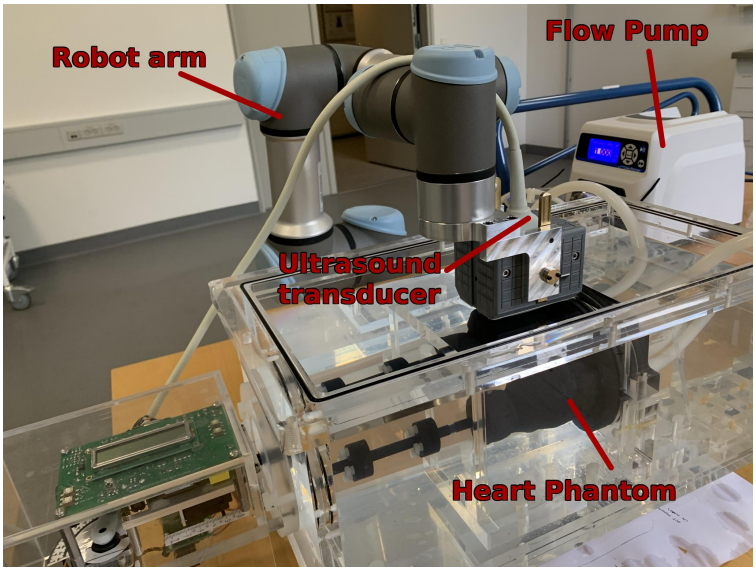

Figure 4.4: Picture of controlled ultrasound scanning of the DHP. The ultrasound transducer is mounted in a custom mount which ensures repeatability between measurements. The cavities in Fig. 4.5 are based on controlled ultrasound scans utilizing the robot arm as seen in this picture.

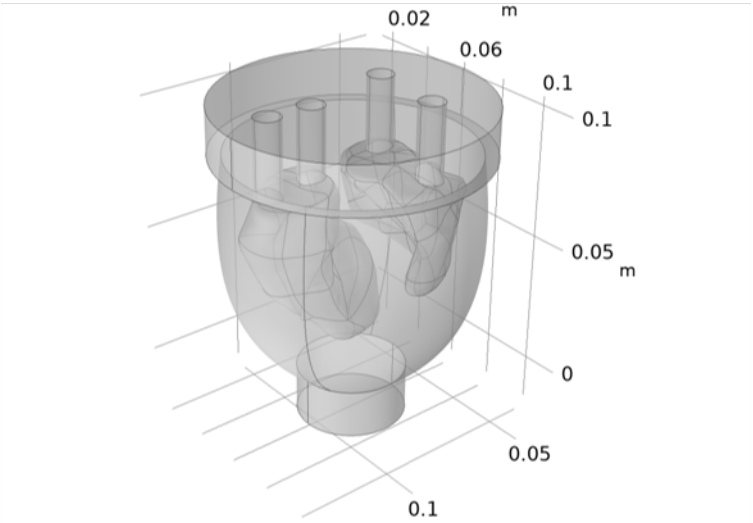

Figure 4.5: CAD model of the DHP based on B-mode data obtained using the UR3 robot arm and imported to COMSOL. Modified from (Zaja 2020).

4.2.6 Phantom setup

This new setup was developed in a bachelor project during the project with the following in mind: easy handling, easy fit in CT scanner, rigid tubing for better control over time dependent flow. Besides collecting all of the parts on a single board that fits the patient bed of a scanner, the setup includes a raised fluid reservoir with rigid tubing connected at the bottom of the reservoir to keep the afterload on the phantom ventricles as controlled as possible. Furthermore the inlet to the reservoir is off-center which facilitates the mixing of the particles in the blood mimicking fluid (BMF).

In her BSc project *Josefine Harbo Arleth* designed a setup for the dynamic heart phantom that makes data acquisition much easier with CT and US. The setup collects all essential parts on a single board that fits on the patient bed of at CT scanner. The parts are: phantom, pump, fixed pipes, fluid reservoir, "swamp", and cable management. This setup will be a part of the robot arm workflow. In Fig. 7.1 the phantom is seen in a CT scanner before the new setup which was very hard to manage due to the weight of the tank and the many cables.

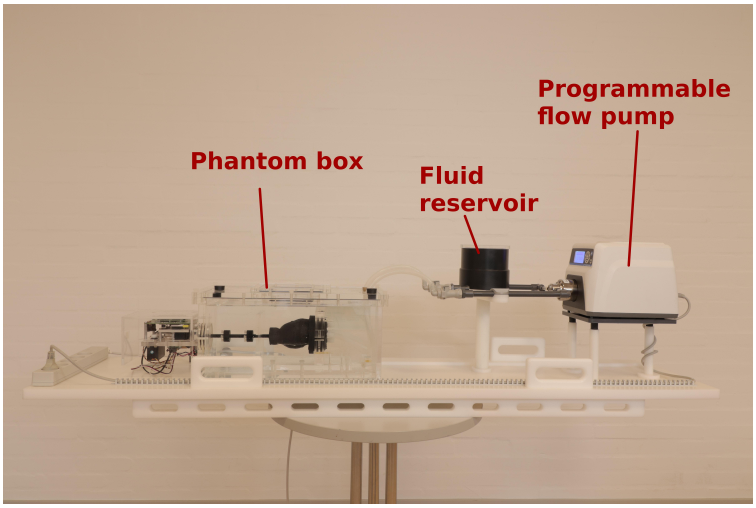

Figure 4.6: A picture of the DHP in the new setup.

CHAPTER 5

Moving Geometry and Registration

This chapter describes the implementation of the movement in the pipeline and discusses choices made when alternative approaches exist. In other words how a time series of 3D medical volumes, are expressed as a cyclic, continuously movement of a single surface. Theory and background is touched in Section 2.5.

A moving surface with continuous cyclic movement is the primary simulation input in the geometry prescribed CFD. Representing the moving geometry as accurately as possible is therefore essential for the simulation to represent reality. The moving surface is extracted from medical 4D images which are discrete in time and space. A method for converting a medical 4D image to a single moving surface is therefore a necessary part of the pipeline before 4D medical images can be used as boundary conditions in the simulation. The entire conversion from 4D medical image to moving surface requires segmentation, registration and validation.

5.1 Reference domain geometry

The reference geometry is the segmentation of the first time instance in the 4D image. This is the geometry on which the displacement field is applied on. When the reference geometry has applied zero displacement it is said to be in its reference configuration. The reference geometry is represented as a closed surface, also called watertight, as an STL mesh. A plot of the DHP's RV is seen in Fig. 5.3. Its corresponding STL mesh is plotted in Fig. 5.1.

5.1.1 Surface representation

In the presented pipeline the reference domain geometry is represented as a surface mesh which represents the myocardium of the ventricle. The STL mesh representing the right ventricle of the DHP is plotted in Fig. 5.1. it should be noted that there is a difference between this mesh and the surface of the computational mesh in Fig. 6.5 which is generated in COMSOL based on the STL mesh. The surface mesh is obtained from image segmentation which is described in Section 5.1.2. The resulting mesh is

stationary, and movement must be prescribed on each mesh node to obtain a moving surface. The surface could alternatively be formulated as splines and control points or even as a parametric expression as by (Evans, Bloor, and Wilson 2001).

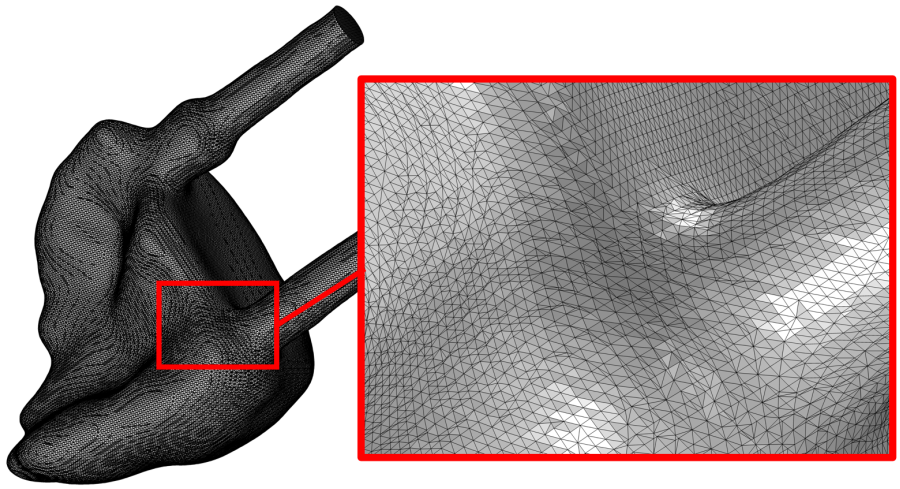

Figure 5.1: The `.stl` mesh resulting from segmentation in MATLAB using the `isosurface` function. Plotted from COMSOL.

5.1.2 Segmentation

Segmentation of human cardiac anatomy from medical imaging is, by itself, an active topic of research. The latest state-of-the-art methods for automated cardiac segmentation are based on machine learning, see (Campello et al. 2021; Sundgaard et al. 2020; Zhuang 2013).

Several factors play a role when deciding on a segmentation method: image modality, spatial resolution, temporal resolution, etc. Furthermore, if the segmented geometry is pathological, methods based on prior knowledge, such as atlases, might cause overfitting issues. Because the heart is always moving, there is also the choice of where in the cardiac cycle the segmentation is performed. Typically ventricle segmentation is performed in late diastole because this is where the ventricle is largest and most stationary. Details of segmentation strategies will not be discussed thoroughly in this dissertation, however several of the supervised master projects during the ph.d. did touch on the subject of preprocessing and segmentation from CTA and US via thresholding and active contours. See (Garreau 2019) and (Zaja 2020).

Commercial software for cardiac segmentation The following software tools have been used during the ph.d. for visualization and for cardiac segmentation:

- Materialise Mimics: commercially available. See Fig. 2.8.
- Slicer: free and open source. See Fig. 2.7.
- Synopsis Simpleware scanIP: commercially available.
- ParaView: free and open source.

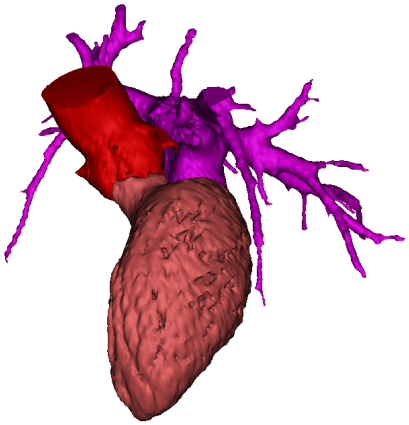

Figure 5.2: Segmentation from the data seen in Fig. 2.8. **Red:** Aorta. **Magenta:** Left atrium with pulmonary veins and protruding tree of vasculature **Bordeaux:** Left ventricle. Note the holes in the left ventricle from trabeculae carneae. This segmentation was performed as part of (Hvid 2018)

Segmentation of human LV from CMR Segmentation from CMR can be more difficult than from CTA for several reasons. Voxel intensity, contrast, spatial resolution (especially slice thickness), cycle averaging (and offsets).

5.2 Registration

The presented pipeline utilizes registration based on MATLAB's `imregdemons` function which is described in section 2.5. This section focuses on some of the details of the diffeomorphic demons and highlights the consequences of this choice in relation to the presented pipeline.

5.2.1 Transformation model

The DD algorithm utilizes free deformation, however regularized. Without regularization each voxel in one image could be mapped to any other voxel in the other image independent of the mapping of the neighbor voxel. This regularization can be described as a Gaussian of the displacement field. In `imregdemons`, the size of the Gauss kernel for the regularization can be adjusted with the parameter "AccumulatedFieldSmoothing". See the (imregdemons documentation, MathWorks 2022). The use of free deformation over a parametric deformation model is a choice made to enable capturing the actual movement of very different types of movement including pathological movement. Using a parametric deformation model could make the calculation simpler and more robust, however it might be too constrained to capture multiple types of pathology.

5.2.2 Similarity metric

The DD algorithm utilizes a voxel intensity based similarity metric. This is possible because the voxel intensity of CTA is very similar for all volumes in the same acquisition. This is also true to a degree for images in different acquisition, as the CT unit is HU, which is an absolute unit. Different acquisition settings will however affect where the dynamic range is prioritized for the given acquisition.

The use of a voxel intensity based similarity metric causes the registration to optimize not only the endocardium position, but everything within the volume of interest. This is not necessarily a bad thing as most of the surrounding tissue is expected to move along with the heart. A possible issue with this approach is the pericardial sac in which the heart can slide freely and causes a large difference in the magnitude of movement over a small distance as the tissue on each side of the pericardial sac can move in opposite directions. This motion is not going to be captured well using the DD algorithm due to the regularization which regularizes this exact type of motion. This is not assessed to be a problem for this use, as the endocardium follows the surrounding myocardium. Therefore it is important to choose a fitting smoothing kernel, `AccumulatedFieldSmoothing`, to avoid the effects outside of the pericardial sac to have an influence on the estimated displacement of the endocardium.

Because the ventricles are often filled with a contrast fluid in CTA, the ventricles and blood vessels have a high voxel value compared to the surrounding tissue. This contributes to the ventricles being "prioritized" in the voxel intensity similarity as the metric is global. The contrast between the ventricles and the rest of the tissue is greatly affected by what intensity "window" is being used. Note that the image volumes must be converted from HU to unsigned 8-bit integers before performing registration. This will greatly decrease the dynamic range as HU spans from -1024 HU to 3071 HU, and the 8-bit unsigned integer spans from 0 to 255. Therefore the conversion must be done in a way that retains the contrast between the ventricles and surrounding tissue.

A possible problem with this similarity metric is contrast fluid washout which might change the intensity of the ventricle over time. This possible effect has not been

investigated, however as long as the ventricle has significantly higher voxel intensities than the surrounding tissue the registration is expected to arrive at a similar displacement.

5.3 Temporal Registration

In this pipeline the temporal registration is achieved by performing a number of independent registrations between one time instance and all other time instances. This implementation has shown to be sufficient for the phantom data, however in-vivo data might need more sophisticated methods as described in section 2.5.5.

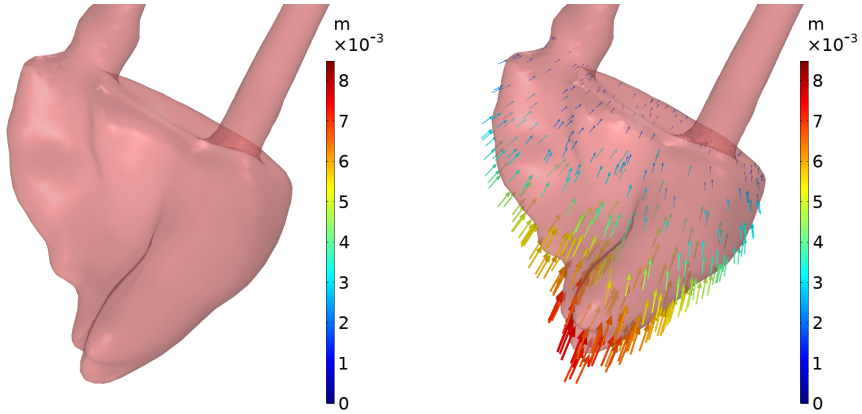

(a) t=0.00 s (b) t=0.42 s

Figure 5.3: The DHP RV surface boundary is shown at two time points in the cardiac cycle. The arrows show the deformation from the reference configuration surface in *(a)* to the current configuration surface in *(b)*. The color of the arrows indicate the displacement magnitude according to the colorbar. Modified from [Paper 2] .

5.3.1 Ensuring periodicity

The simulation is assumed to be cyclic, therefore the movement has to be cyclic. This is important for the position of the surface at first and last time instance. Furthermore, because it is a dynamic simulation, the first derivative of the motion needs to be equal at the first and last time instance of the movement.

The position of the surface is ensured by actually using the first volume as the last volume. In other words the first volume is assumed to be equal to the last volume. A

5.4 Implementation

The registration method implemented in the existing pipeline is the MATLAB implementation of the Diffeomorphic Demons algorithm `imregdemons` ((Thirion 1998; Vercauteren et al. 2009)). The algorithm is written in pseudo-code in Algorithm 1, and is sketched in Fig. 3.3. The algorithm simply performs a registration between the first input volume and all of the other volumes. The first registration is technically between the first volume to itself which is not calculated and instead assumed to be zero displacement. Note that the unit of the displacement is in the unit of the voxel size. In all implementations the input volumes have been interpolated onto an isotropic grid. The center-to-center distance between the voxels is defined in Algorithm 1 as `regParams.iso_size` in meters. Multiplying the resulting displacements with this factor converts the displacement field unit to meters. Note that all of these registrations are independent of each others and can therefore be parallelized. Furthermore the implementation of MATLAB's `imregdemons` support GPU acceleration which speeds the process up provided the necessary hardware is available.

An illustration of the resuting moving surface along with arrows indicating the displacement field at the point of application is rendered in COMSOL and ploted in Fig. 5.3.

Algorithm 1: Pseudo code in pseudo MATLAB syntax (indexing starts a 1). Note that displacements for t=1 and t=N+1 are zeroes.

function registration_DHP_rahv(V);
Input : V of size: $[m, n, p, t]$
Output : $[dx, dy, dz]$, each of size $[m, n, p, t]$
$N = t$;
$[dx, dy, dz]$ = zeros(n, m, p, N+1);
volume_moving = V(:, :, :, 1);
iter = 2;
while $iter \leq N$ **do**
    volume_fixed = V(:,:,:,iter);
    d = imregdemons(volume_moving,volume_fixed);
    dx(:, :, :, iter) = d(:, :, :, 1);
    dy(:, :, :, iter) = d(:, :, :, 2);
    dz(:, :, :, iter) = d(:, :, :, 3);
    iter = iter +1
end
dx = dx.*regParams.iso_size;
dy = dy.*regParams.iso_size;
dz = dz.*regParams.iso_size;
return dx, dy, dz

5.5 Validation of registration

The displacement fields resulting from the registration method described in this chapter are going to be one of the primary inputs to the simulation pipeline. Therefore the quality of the simulation is going to be directly dependent on how accurately the registration is representing the real movement. Therefore the registration itself needs to be validated to make sure the resulting displacement is representing the movement measurably correct. While this validation has not been formally formalized and published the first implementation has been tested on the synthetic dataset with success within the limitations of the dataset.

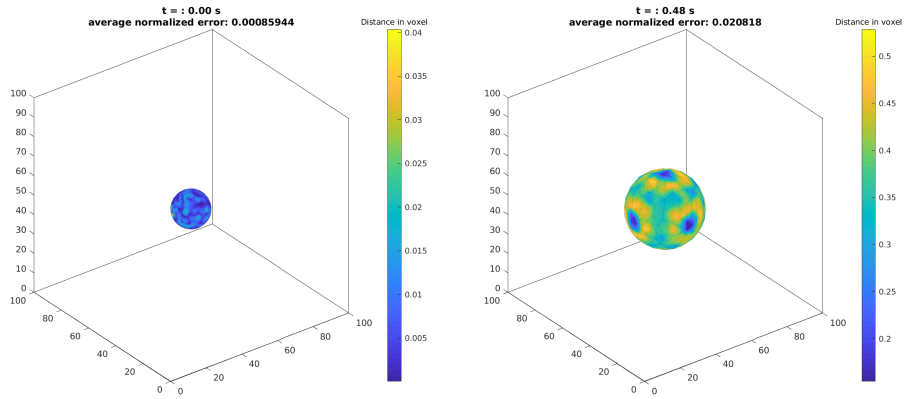

(a) index=1 (b) index=13

Figure 5.4: The movement of the from the synthetic dataset described in Section 2.5.2 when the pipeline registration and movement is applied to the synthetic data. The color represents the absolute distance between the true position (known from the dataset synthesis) and the actual position which has been estimated via the pipeline and applied in COMSOL.

In Fig. 5.4 are the results from applying the registration pipeline on the moving sphere from the synthetic dataset and visualizing the movement in COMSOL. As further described in Chapter 3 the displacement field based on the MATLAB registration is imported to COMSOL and applied to a surface mesh of the sphere from the first time index of the synthetic dataset. Because the expected movement of the sphere is known, due to the dataset being constructed synthetically, the distance between the moving sphere in COMSOL and the expected position of the sphere can be calculated and visualized with colors and a color legend, just as seen in Fig. 5.4. Note that the unit here is absolute

distance in the unit of the voxel size. Please note that the relatively large errors shown is a result of the surface segmentation not being as smooth as the ideal position which it was being compared to. This is because the dataset the synthetic dataset is spatially undersampled.

The validation data are also presented more quantitatively in the boxplots in Fig. 5.5. Here the error of each mesh-node in the surface is plotted as a boxplot for each time index. It should be noted that since the movement is continuous, these errors could be plotted for any arbitrarily chosen time between these discrete time indices.

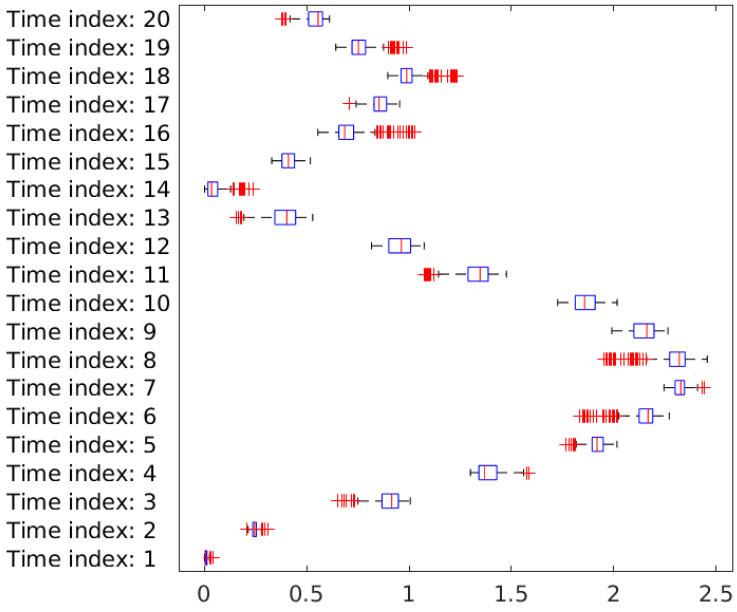

Figure 5.5: A boxplot for the same errors as plotted in Fig. 5.4. The error for each mesh-node in the sphere is added to the boxplot (x-axis) for each time index (y-axis). Note that the unit is defined by the voxel size.

CHAPTER 6

Implementation in COMSOL

This chapter will focus in the implementation of the CFD pipeline in COMSOL. The method is designed to be generally applicable to moving geometries, but only the phantom implementation for [Paper 1] and [Paper 2] are shown here.

COMSOL Multiphysics is a commercially available software for setting up and solving multiphysics models numerically. Ideally the mathematical models and their solutions are independent of the software tool used to calculate the solution. Therefore any software, commercially available or custom code, should always yield similar results when given the same model and model parameters to solve. Therefore, even though the model inputs in this project have been formulated to fit into the COMSOL way of defining models, the software choice was made based on availability and convenience. Hence, similar results are expected if the same model were to be solved using another software, as long as good practices for verification, such as performing a mesh independence study, are followed.

6.1 What COMSOL does

COMSOL handles all of the numerical computations of the mathematical model which consists of: governing equations, fluid properties, domain geometry, domain movement (displacement field), and boundary conditions in the form of inlet flow velocity, outlet pressure, and no-slip at the myocardium. it should be noted that all of these elements are defined independently of COMSOL. What COMSOL does is to create a convenient model that defines the domain and boundaries based on the inputs. To solve the mathematical model in COMSOL the following is done (in COMSOL):

- a computational mesh is generated for the domain geometry
- The time dependent and cyclic domain movement is calculated based on the displacement field
- the initial conditions are estimated in a stationary study by using the model values at t=0
- the time dependent study is solved for several cycles, until the solutions have converged

Once the mesh and physics are defined all of the above could be calculated in a single step. However, for simplicity and stability, they are split into several COMSOL *studies*. The implementation, including verification, is described in the sections below.

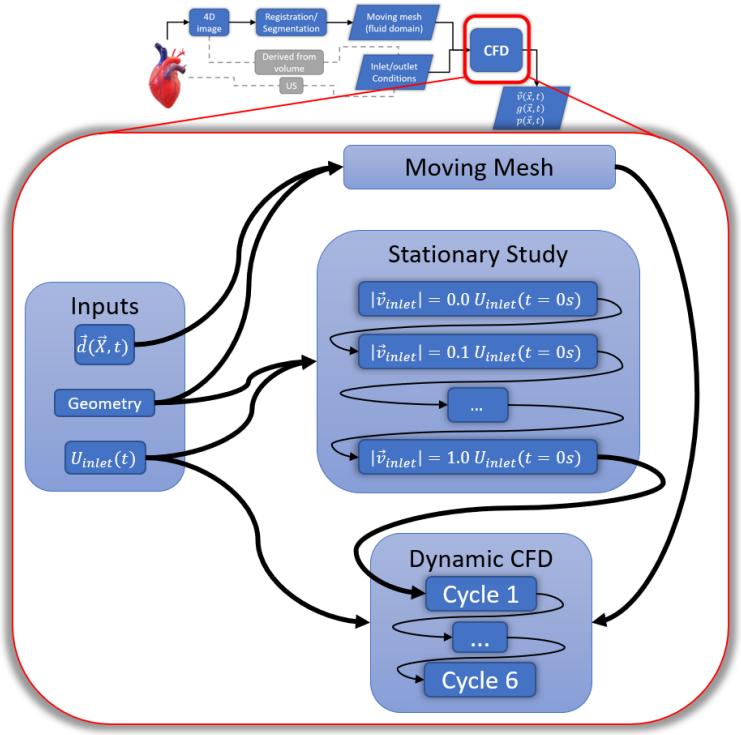

Figure 6.1: Flowchart describing the steps involved in the geometry prescribed CFD. It is an expansion of the CFD block in the flowchart in Fig. 3.1

6.2 Inputs

The mathematical model is formulated in a format that can be used as inputs in COMSOL to create a model. In Fig. 6.1 this formulation is referred to as "Inputs". The inputs to the model presented in [Paper 2] are presented here.

6.2.1 Geometry

The domain geometry is represented as a stationary and "watertight" surface. The input geometry surface is the result of segmentation of a single time instance from CTA (see Chapter 7) which corresponds to a stationary volumetric image. The surface is exported as an .stl mesh. It is important that the surface mesh is defined in the exact same coordinate system as the displacement field. See Fig. 5.1. The import feature in COMSOL accepts .stl meshes, and is capable of repairing most small mesh imperfections. When the geometry

is imported, it is "turned into a solid". In this step the wall boundary, inlet boundary, and outlet boundary are defined as well, as seen in Fig. 6.5.

6.2.2 Displacement field

The displacement field is represented discretely as three vector components per voxel in each of the CTA volumes. This displacement field is the result of the volumetric image registration.

6.2.3 Inlet velocity

The inlet velocity is interpolated from measurement data in .csv format. The first column of the .csv file contains time points, and the rest of the columns specify spatial coordinates and flow velocity. In the presented case it can be assumed that the spatial velocity profile is uniform and perpendicular to the inlet surface. Therefore the .csv file needs only to contain two columns; time in seconds, and absolute velocity in meters per second. This input is defined as an interpolation function i COMSOL and is applied as an inlet condition in the time dependent CFD study. The COMSOL function, called `inletFunc(t)`, is plotted in Fig. 6.2. Note that it is important that the value(s) at the first and last time instance are equal, and that the time derivative are close to equal at the first and last time instance as well. Otherwise numerical instabilities would follow when running the simulation for several cycles.

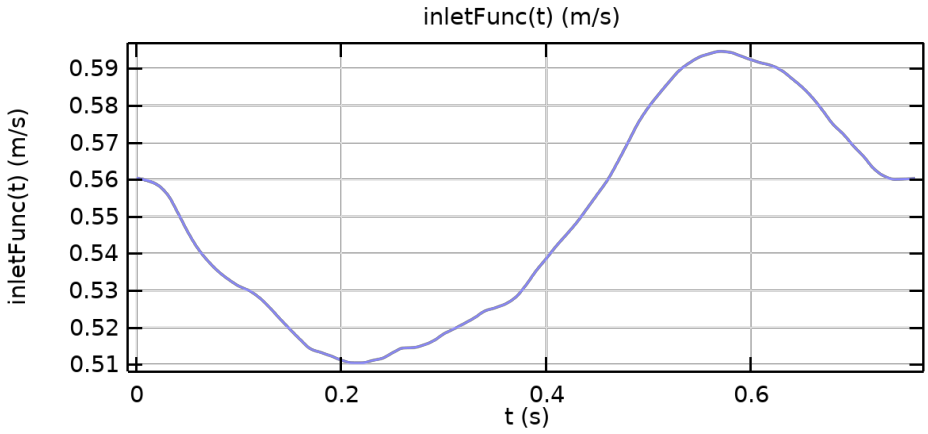

Figure 6.2: Temporal inlet velocity profile as applied to the inlet in [Paper 2] .

6.3 Studies

Several steps have to be calculated to obtain a solution from the defined mathematical model. The steps are, as seen in Fig. 6.1, the moving mesh, a stationary CFD, and a dynamic CFD. These are solved separately in separate "COMSOL studies". It is technically possible to calculate everything all at once, however splitting the calculation into separate studies have several advantages. Firstly, the movement is calculated separately for a single cycle. The movement of the wall boundary is known from the displacement field, however this study calculates the position of the nodes inside the domain. This solution is identical for each cardiac cycle and therefore only needs to be calculated once. Secondly, the initial conditions for the first cycle are unknown. Starting with a bad initial guess might cause the computation time to increase, or in worst case not converge towards a solution at all. Therefore the initial conditions are estimated in a separate study as well. This ensures the problem to be more well posed. Finally the dynamic CFD is divided into a study per cycle. Each cycle study uses the last time frame of the previous cycle study as initial conditions. For this reason the CFD studies cannot be run in parallel. It is however an advantage to separate each cycle into a separate study to evaluate cycle convergence. See Section 6.3.3.1.

6.3.1 Moving mesh

In this study the displacement field is applied to the wall boundary. Therefore, even though the displacement field is already known for the boundary, the movement of the domain volume is calculated in this step. This has no direct physical meaning as the domain volume is fluid filled cavity. The movement of the domain is used only to move the mesh nodes to be in the most appropriate position at all times. This is, in principal, achieved by assuming the domain volume is an elastic solid material. In practice this is achieved by applying a smoothing function on the domain volume. The choice of smoothing method is depending on the application. For the expected deformations in the cardiac cycle *hyperelastic smoothing*, which minimizes mesh deformation energy inspired by neo-Hookean materials, has been the most reliable choice. Note that this study is calculated on a coarser computational mesh (Fig. 6.4) compared to the CFD mesh (Fig. 6.5) for efficiency and stability. See section 6.4.

6.3.1.1 External MATLAB function for interpolation

COMSOL does not support 4D interpolation as a built in functionality. It is however possible by calling an external MATLAB function `pipelineInterp(X,Y,Z,t,dim)` that interpolates any number of arbitrarily queried points by COMSOL at simulation time. The queried points are defined in the geometry frame, hence the capital letters `X,Y,Z` for input coordinates. `t` is time, and `dim` specifies what direction of displacement the output specifies. The reason is that the *Moving Mesh* interface in COMSOL defines displacement per basis vector component in the spatial frame. Instead of defining three

almost identical interpolation function, one for each vector component, the queried vector component is defined by a fifth input. Please note that the deformation is defined in the spatial frame, hence the lowercase `x` in $d\vec{x}$ in (6.1). For the interpolation function to be clear and efficient, the displacement field is stored as a MATLAB struct with a field for the texttttX, Y, Z coordinates of the geometry frame at each of the discrete points in time, and the corresponding `dx, dy, dz` displacements in the spatial frame at each of the time instances. The implementation of `pipelineInterp` has been written out in the code box below.

```
function [dOut] = pipelineInterp(X, Y, Z, t, dim)
%PIPELINEINTERP loads a displacement field with the variables dx, dy, ↩
    dz,
%on the ndgrid X, Y, Z into the struct V, and interpolates either dx, ↩
    dy,
%or dz, in the query poinds provided by the inputs X, Y, Z, t and "dim↩
    ".
%"dim" is a switch that determins if dOut interpolates dx, dy, or dz.
% This function is an external function to be called from COMSOL.
%   % Last edited 2021-08-18 , rahv@dtu.dk
persistent V

if isempty(V)
    fileName = '< path to data >/displacementField.mat';
    V = load(fileName);
    V.t = (0:20)/(20)*0.76;
end

if dim ==1
    dimName = 'dx';
elseif dim==2
    dimName = 'dy';
elseif dim==3
    dimName = 'dz';
end

dOut = interpn(V.X(:), V.Y(:), V.Z(:), V.t(:),V.(dimName),X,Y,Z, t, '↩
    linear', 0);

end
```

`pipelineInterp`: External MATLAB function used for interpolation of the discrete displacement field at simulation time in COMSOL. Note: the `<path to data>` has to be replaced with the absolute path to the displacement field struct which can be read by COMSOL at computation time.

$$d\vec{x}: \begin{bmatrix} pipelineInterp(X[1/m], Y[1/m], Z[1/m], t[1/s], 1) \\ pipelineInterp(X[1/m], Y[1/m], Z[1/m], t[1/s], 2) \\ pipelineInterp(X[1/m], Y[1/m], Z[1/m], t[1/s], 3) \end{bmatrix} \tag{6.1}$$

6.3.2 Stationary study

The stationary study is run to estimate the initial conditions for the dynamic studies as realistically as possible. This is done by running several sequential stationary studies on the reference configuration of the geometry domain with increasing inlet velocity until the inlet velocity reaches the inlet conditions at t=0 for the dynamic studies. Each stationary study uses the previous solution as an initial guess, and the first study uses zero pressure and zero velocity everywhere in the domain geometry as initial guess. The process is sketched in the flowchart in Fig. 6.1.

6.3.3 Dynamic studies

This is the actual simulation of the heart cycle(s). Each heart cycle uses the solution from the moving mesh to prescribe deformation to the fluid domain and walls. The wall boundary is assigned as "no slip", the outlet is "constant pressure", and the inlet is defined as the function plotted in Fig. 6.2. The initial conditions for the first cardiac cycle is defined as the solution of the stationary study. From here, each consecutive cardiac cycle uses the last time frame of the previous solution as an initial condition. The number of cycles to solve depends on how quickly the solutions converge towards the same solution. This is important to make the final solution independent on the initial conditions. The cycle convergence is estimated by calculating how much several metrics of the solution changes between each cardiac cycle solution. See Section 6.3.3.1.

6.3.3.1 CYCLE CONVERGENCE

The blood flow patterns in the solution are presumed to be cyclic. It is therefore expected that the solution for each cardiac cycle converges towards the same solution when simulating several consecutive cardiac cycles. The necessary number of cycles to calculate before reaching convergence depends on the accuracy of the initial conditions for the first simulated cardiac cycle. To evaluate when convergence is achieved, the velocity magnitude is stored at the same time index for all cycles at several corresponding spatial locations. These velocity magnitudes are compared to the previous cardiac cycle by subtraction, and visualized in a box plot for each cardiac cycle in Fig. 6.3.

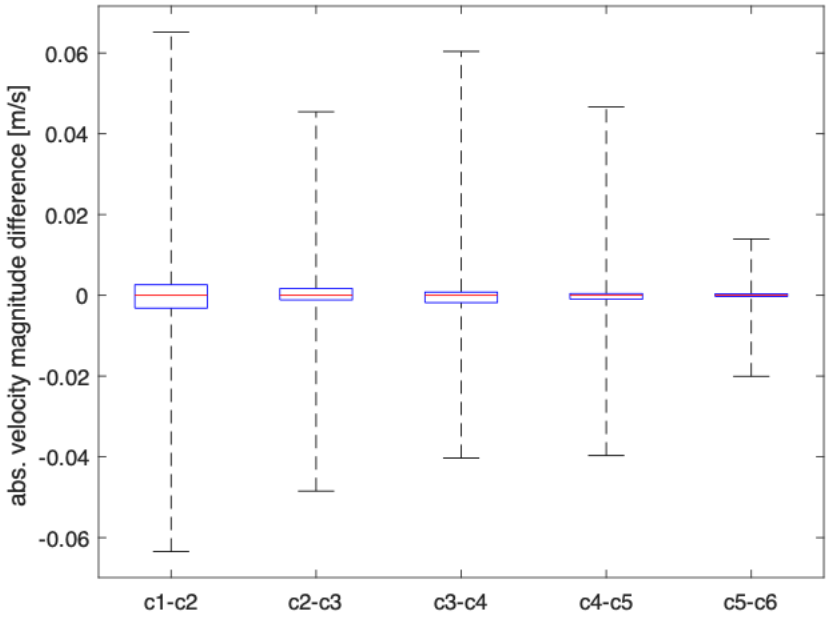

Figure 6.3: Cycle convergence evaluation. Each box plot visualizes difference in velocity magnitude between consecutive cycles measured in 97,831 points. Modified from [Paper 2] .

6.4 Meshing

The appropriate mesh element type and mesh size typically depends on the solution. Everything from governing equations and multiphysics coupling to spatial scale and time scale matters. Even the solution itself can be used to optimize the computational mesh. This is obviously not always possible to take into account directly, since the mesh us used to estimate the solution. However some things can be optimized based on prior knowledge, such as relatively larger spatial velocity gradients occurring close to boundaries. This is automatically taken into account in COMSOL when a boundary in a fluid flow problem is defined as a no-slip wall. This will cause the COMSOL mesher so suggest adding specialized boundary layers along those wall boundaries. See Fig. 6.5. Based on the physics being solved, COMSOL is able to suggest a so-called "physics controlled mesh" with the single user input parameter: "element size". Two separate computational meshes have been implemented in the presented model; one for the *moving mesh* study, and one

for the CFD studies.

6.4.1 Mesh for Moving Mesh Study

The mesh for the *moving mesh* study is the COMSOL "physics controlled mesh" with *normal* element size. The result is a mesh consisting of 10,057 tetrahedra and 3,610 triangles, see Fig. 6.4.

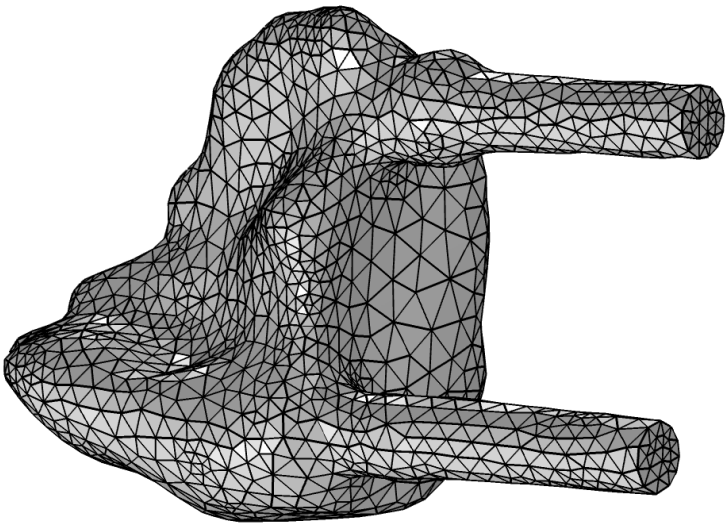

Figure 6.4: Computational mesh for the "Moving Mesh" study in COMSOL used in [Paper 2] . The mesh is consisting of 10057 tetrahedra and 3610 triangles. The computational mesh for the CFD is plotted in Fig. 6.5.

6.4.2 Mesh for CFD Studies

The same computational mesh is used for the stationary CFD and the dynamic CFD. The mesh is generated as a *physics controlled mesh* based on fluid dynamics, but with the following changes: The surface elements size is defined as *fine*, the volume element size is defined as *normal*, the number of boundary layers has been defined as three. These changes to the mesh have been determined by running the simulation on several mesh types and sizes in a mesh independence study (Section 6.4.3). The final mesh consists of 303,270 tetrahedra, 80,784 prisms, 27,208 triangles, and 168 quads. The final mesh is plotted in Fig. 6.5.

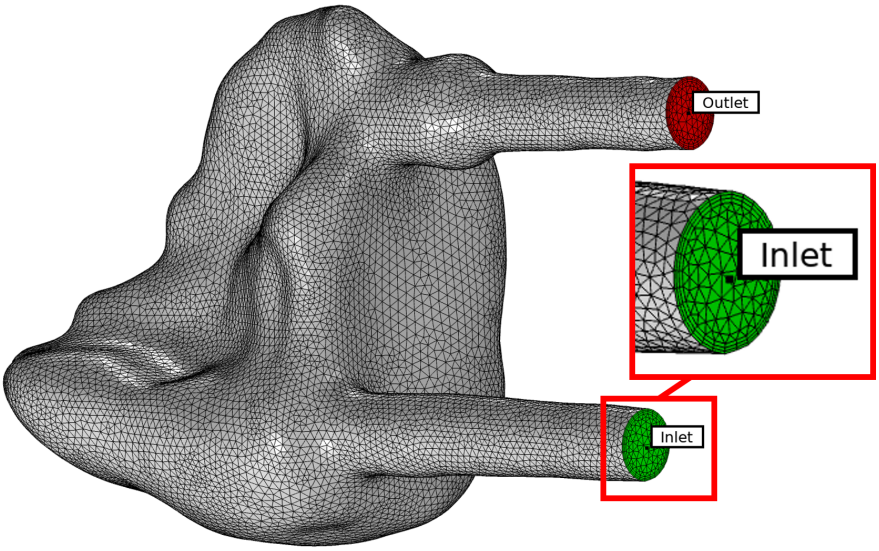

Figure 6.5: Computational mesh for CFD. **Gray:** Wall boundary **Green:** Inlet boundary **Red:** Outlet boundary. The red zoom box highlights the three boundary layers visible at the inlet. The mesh is consisting of 303,270 tetrahedra, 80,784 prisms, 27,208 triangles, and 168 quads. Modified from [Paper 2]

6.4.3 Mesh independence

A mesh independence study is performed by solving the full model with four different mesh sizes for the computational mesh. It is important to remember that the mesh independence is not only related to the number of mesh elements or the number of degrees of freedom. The location of the mesh nodes and the mesh element types play a role as well. In the presented mesh independence study the boundary layer elements are kept in the same configuration for all four meshes because the numerical methods are unable to find a solution at the wall boundary with an insufficient mesh size. The meshes were generated in COMSOL as described in Section 6.4.2, with the only difference being the volume mesh elements size. The volume mesh size for mesh 1-4 respectively is: extra coarse, coarser, coarse, and normal. These are plotted in Fig. 6.6. Note also in Fig. 6.6 that the tetrahedral mesh elements close to the boundary is relatively small compared to the rest of the tetrahedral mesh elements. This is because they must match the size of the boundary layer mesh elements. This "transition layer" helps keeping the computational mesh close to the wall boundary more refined, even extending out from the boundary layer mesh elements.

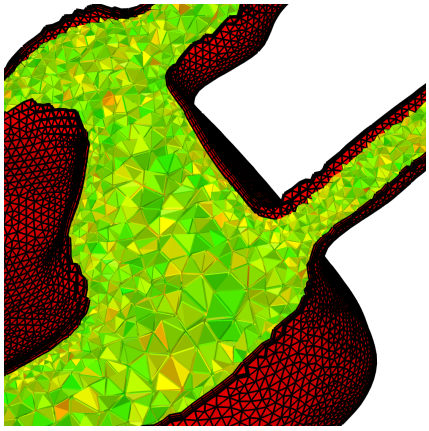

(a) mesh 1: Extra coarse

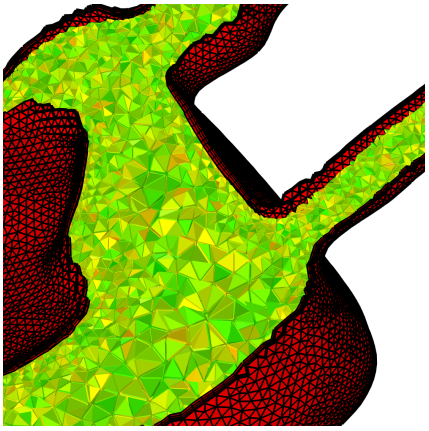

(b) mesh 2: Coarser

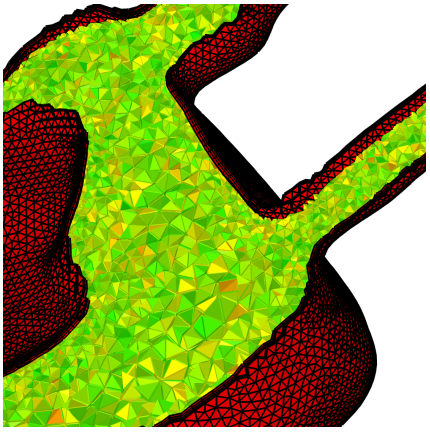

(c) mesh 3: Coarse

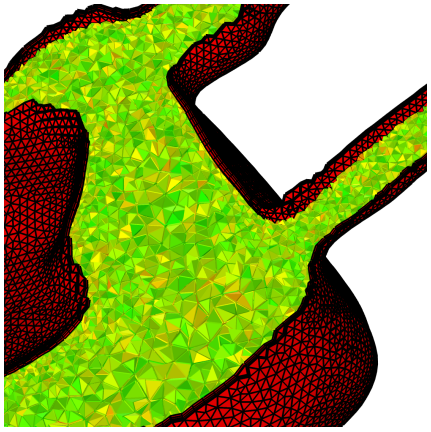

(d) mesh 4: Normal

Figure 6.6: The four meshes used for mesh independence study. The convergence of a global parameter in the solutions from the four meshes is plotted in Fig. 6.7. Note that the boundary layer elements are kept at a consistent size while the size of the volume elements is decreasing gradually. **Red w. black edges:** Boundary layer elements consisting of triangle and prism elements **Green/red with no edges:** volume elements consisting of tetrahedral elements.

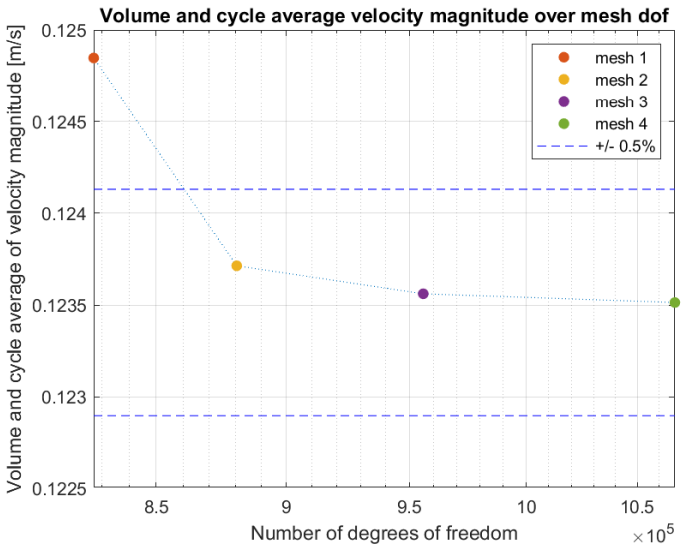

Figure 6.7: Mesh independence convergence curve. The four meshes are plotted in Fig. 6.6. Modified from [Paper 2]

CHAPTER 7

Data Acquisition

This chapter describes the data acquisition for the project. The main data were acquired at Rigshospitalet (Copenhagen, Denmark), DTU (Lyngby, Denmark), and at St. Olavs University Hospital of Trondheim (Trondheim, Norway). The acquisitions are divided into two main sections; phantom data, and in-vivo data.

Summary The dynamic, time dependent data described here have been used for [Paper 1] , [Paper 2] , and [Poster 1] . Some of the data, specifically the stationary data, have been obtained for student projects and have been a valuable stepping stone to understanding the pipeline before applying it to the more complex time dependent data. Three groups of phantom data are defined in this chapter; 4D image from CTA for the simulation, ultrasound VFI for ground truth, and CFD simulation output from pipeline. The aim of the phantom study is to validate the pipeline by comparing the pipeline output with the measured VFI ground truth. The pipeline is applied to the DHP in the same way it would be applied in-vivo.

7.1 Phantom data

The main results of this project are obtained from data acquired from the DHP (Chapter 4). The advantage of using the phantom is the repeatability it provides. The repeatability makes it possible to measure data over several different acquisitions and expect the inter-measurement variability to be low. This is a great advantage over in-vivo data because the cardio-physiology cannot be controlled which in turn provides a relatively high inter-measurement variability. The DHP has another advantage, which is that the movement can be programmed to be simpler than the living heart. Lastly, and obviously, the movement of the DHP is known simply because the operator programs the movement. This makes the DHP a great tool for low-level validation of the presented pipeline.

7.1.1 Computed Tomography - phantom data

Two scan types were performed; static CT scans and dynamic retrospectively gated CTA scans. Two acquisitions were made for each scan type. The static CT scan were acquired twice; first without contrast fluid, and afterwards with contrast fluid in the fluid reservoir which was connected to the phantom RV. The contrast fluid is very clearly seen in Fig. 7.2, which is from one of the dynamic acquisitions.

The dynamic scan was acquired while the dynamic heart phantom was moving as defined in Table 4.1 plotted in Fig. 4.3. The dynamic scan was retrospectively gated using the simulated ECG output. ECG electrodes were attached to a dedicated box that simulates the R-peaks of the ECG as if the electrodes were attached to the chest. The ECG box is visible in the lower left corner of Fig. 7.1 with the ECG electrodes attached. The rendered volume in Fig. 7.2 is one volume out of the 20 volumes with 5% phase increase in the cardiac cycle as illustrated in Fig. 3.2.

Data output series of dicom volumes from retrospectively gated CTA. 20 volumes within one cardiac cycle. The reconstruction used for [Paper 1] and [Paper 2] has a voxel size of: 0.6 0.6 0.5 mm, although other reconstructions are available. The dicom volumes are interpolated to 20 isotropic matrices, or one "4D matrix", before segmentation and registration.

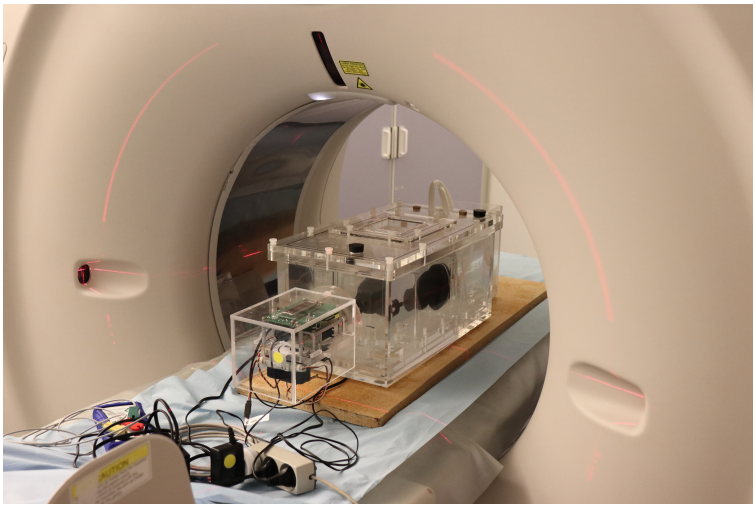

Figure 7.1: DHP in CT scanner at Rigshospitalet, Denmark. Notably this acquisition was performed before the new DHP setup was designed (see 4.2.6).

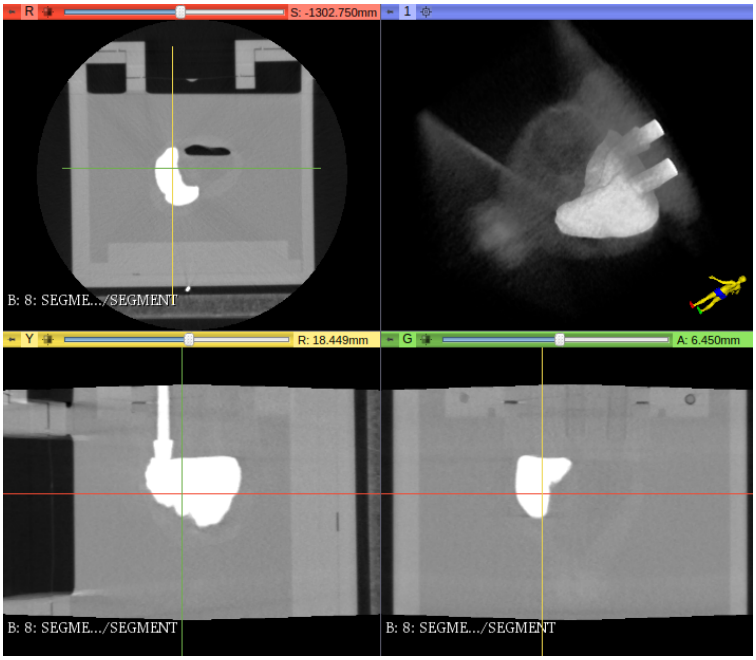

Figure 7.2: View of CT volume from 3D-Slicer. X-, Y-, and Z-plane, and a volume rendering.

7.1.2 Ultrasound - phantom data

Several ultrasound acquisitions of the DHP have been performed during this project. In this section is an overview and examples of the data types that were acquired.

7.1.2.1 B-MODE - PHANTOM DATA

Every time any US acquisition was made, B-mode acquisitions were also made. This is because the B-mode images are being used to navigate the anatomical location of the oter types of acquisition, such as VFI. Three B-modes acquisitions that provided insight to this project were; the volumetric B-mode acquisitions using the sliding fixture, the volumetric B-mode acquisitions using the UR3 robot arm, and the VFI acquisitions, where the B-mode images were essential for synchronizing the phase of each VFI acquisition and between VFI flow and the CFD output flow. See Section 7.1.2.2.

The "volumetric B-mode images" are obtained as planer 2D ultrasound. The third dimension of the volume is obtained by acquiring several parallel planes with a precise, and known, spatial relation. This can be obtained by either the sliding fixture (see Fig. 4.1) or the UR3 robot arm (see Fig. 4.4). an example of a 3D volume resulting from this approach is rendered in Fig. 7.3. Note this volume contains two orthogonal acquisitions

of the same heart phantom.

Figure 7.3: Volume rendering from a series of B-mode scans in the sliding fixture. See (Garreau 2019). This data were acquired using a convex probe with an output pixel size of (0.15 mm, 0.15 mm) and an inter slice distance of 2 mm.

7.1.2.2 VFI - PHANTOM DATA

The VFI dataset used for [Paper 1] and [Paper 2] was acquired from an ultrasound probe attached to the sliding fixture (see Fig. 4.1) with 5 mm inter-plane distance. This results in 8 parallel planes, covering the entire right ventricle during repeated contractions as illustrated ind Fig. 7.6. All of the acquisitions are stitched together in MATLAB, resulting in an, almost volumetric, time dependent dataset. Examples can be seen in Fig. 8.3. Note that VFI only measures in-plane velocities, and therefore only two of the three dimensions are measured in this dataset.

The acquisition is similar to the "volumetric B-mode" acquisition except for the movement of the heart phantom. The 2D acquisitions are therefore not still images, but rather short video acquisitions. This generates two problems that must be solved before the VFI data can be "stitched" together to form a volumetric dataset.

The first problem is the phase of the cyclic phantom movement which is not likely to be the same in each acquisition. As a result of this each acquisition has its own phase of the phantom movement which needs to be aligned between all acquisitions by time-shifting each acquisition with an appropriate time interval. This could have been

solved by using the ECG signal for gating just like in the CTA acquisition, however the ultrasound equipment does not have that capability. Instead the phase of each acquisition is estimated based on the deformation of the corresponding B-mode images which are acquired in parallel with each of the VFI acquisitions. This phase synchronization is performed on all data, inter-slice as well as intra-slice. The reason for acquiring several intra-slice acquisitions is caused by the second problem with the time dependent data.

The second problem is the frame-rate of the VFI acquisition which is limited by the width of the VFI acquisition; the wider the VFI region, the lower the frame-rate. To cover the entire flow region of interest at at reasonably high frame-rate it is therefore necessary to perform several "narrow" VFI acquisitions within the same 2D slice. In Fig. 7.5 an example of these narrow regions are plotted for a single time frame in a single slice. The regions are overlapping and can therefore be stitched together spatially to a single slice. Note that the frames in Fig. 7.5 have been phase synchronized.

Figure 7.4: Example of setup for VFI acquisition. The scanner monitor provides la live preview of the flow direction and magnitude as an overlay to a B-mode image. Note the fluid in the fluid reservoir is milky white. This is the blood mimicking fluid which is necessary for performing VFI measurements.

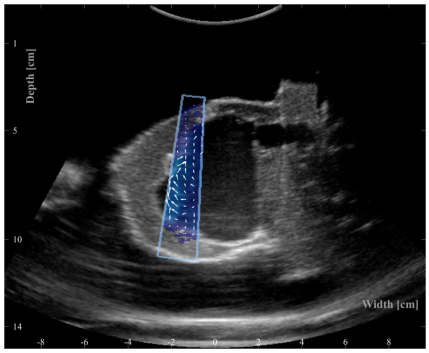

(a) t=0s, Line 2 of 4

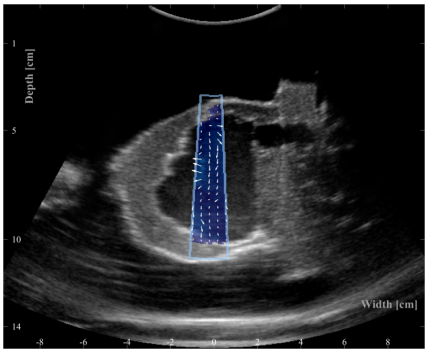

(b) t=0s, Line 1 of 4

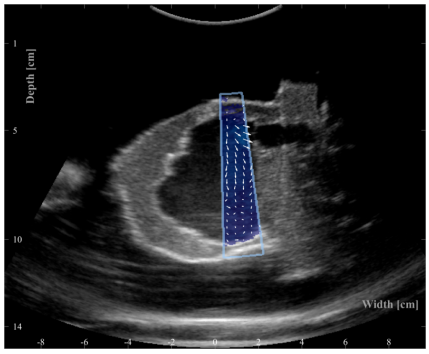

(c) t=0s, Line 3 of 4

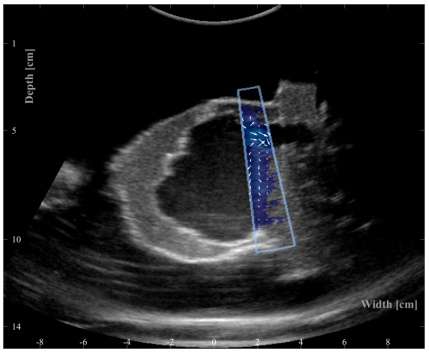

(d) t=0s, Line 4 of 4

Figure 7.5: Example images of "narrow VFI acquisition" within the same plane. The cardiac phase has been synchronized between the four acquisitions from the movement of the B-mode image. The four separate "narrow VFI acquisitions" are overlapping, and can therefore be stitched together to a single plane that represents in-plane velocities.

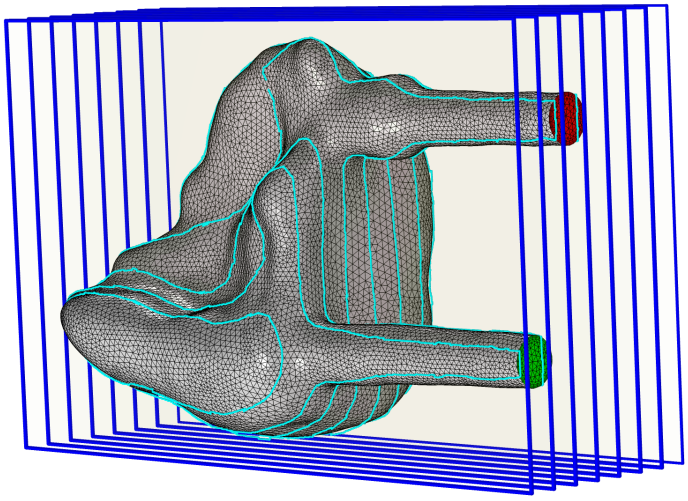

Figure 7.6: Illustration of the position of the ultrasound scan planes. Modified from [Paper 2] .

7.2 In-vivo data

The in-vivo dataset presented in this section has been acquired on three subjects with no known cardiovascular disease during a research stay at SINTEF/NTNU in Trondheim, Norway. The dataset for each subject consists of 4D flow MRI, including the 4D cardiac anatomy, and 4D ultrasound flow imaging. The initial plan for the dataset was to first apply the simulation pipeline on the anatomical MRI acquisitions of each of the three subjects and then compare the pipeline flow patterns to the measured flow patterns from 4D flow MRI and 4D ultrasound flow imaging. However due to unforeseen circumstances and lock-downs it was not possible to perform these actions on the dataset within the project timeline. This in-vivo dataset is however still a key part in demonstrating the potential of the pipeline, and is therefore presented as part of this dissertation.

7.2.1 Ultrasound - in-vivo data

The ultrasound has been acquired in `.dicom` format as well as in the raw "data dump" format `.h5`. As it was not possible to post-process the raw data within the timeline of the project, the presented example data in Fig. 7.7 is created based on the available `.dicom` data, which only contains screen-dumped information as opposed to the full three dimensional and time dependent flow field.

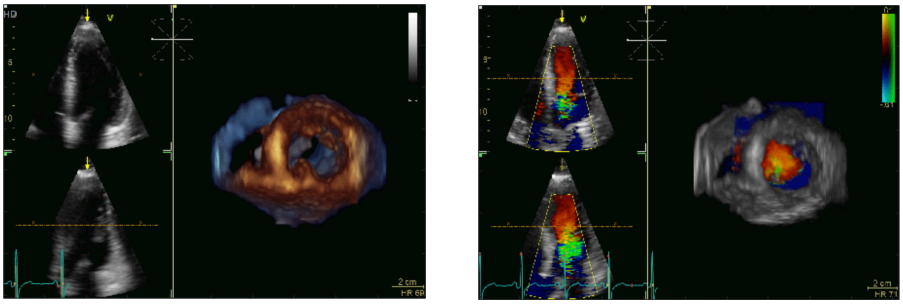

(a) 3D+t ventricle geometry

(b) 3D+t ventricle Doppler flow

Figure 7.7: Example of in-vivo ultrasound anatomy and flow acquisition. The two images are standard views, however raw data has been captured as well which can be translated into a generalized time dependent three dimensional field. Note that (a) and (b) is not in the same cardiac phase.

7.2.2 Magnetic Resonance - in-vivo data

The MRI acquisitions were all performed on the same Siemens MR scanner using a body coil. The US and MRI acquisitions were all made within two months which is deemed sufficient to avoid large changes in the heart anatomy and physiology.

7.2.2.1 Anatomy

Several anatomical acquisitions were made with the TRUFI_CINE acquisition type, which is a type of T2-weighted MR fast imaging. This type of acquisition was made with the following slice directions, or views: short axis (SAX) view, long axis (LAX) view, 2-chamber view, and 4-chamber view. The most easily identifiable is the SAX stack, which consists of a number of parallel slices of the heart with a thickness of 6mm and a total voxel size in mm of `[1.33, 1.33, 6.00]`. Each of these SAX slices has 25 time instances which are obtained from retrospective gating based on an ECG signal. The slices are stored as a series of `.dicom` files, one for each time instance, in a folder for each slice.

To obtain a three dimensional and time dependent dataset each voxel in each SAX slice can be assigned a spatial and temporal coordinate based on the dicom header. In Fig. 7.8 a single time frame from the SAX stack of subject 1 is rendered.

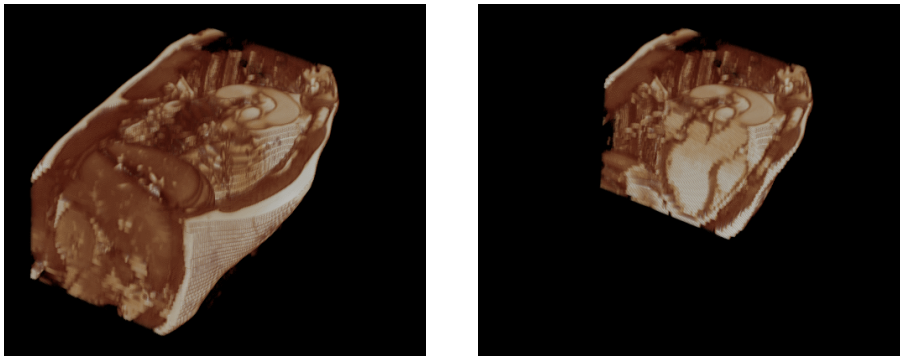

(a) Subject 1, uncut (b) Subject 1, cut through LV

Figure 7.8: 3D rendering of the first time instance (late diastole) of subject number 1. Based on the TRUFI_CINE SAX stack. **Left:** The entire volume acquisition. **Right:** The same volume as *right* with a cut to see inside the left ventricle.

7.2.2.2 Flow

In addition to the anatomical acquisitions the intra-ventricular flow was estimated as well using phase encoding. The acquisitions are made in so-called "two-slice" stacks which, for the SAX acquisition, consists of stacks of acquisitions alternating between anatomical contrast and phase encoded contrast, which is the flow velocity in the direction perpendicular to the image plane. This is referred to as "through flow". The voxel size in mm for all of the flow acquisitions is `[1.77, 1.77mm, 5.00mm]`. In Fig. 7.9 two neighbor SAX slices are plotted; one shows the anatomical contrast, and the other shows the velocity encoded contrast.

Several two-slice stacks like the SAX stack have been acquired as well. The different directions of the stacks provide multiple directions of flow, and the dicom header provides means of assigning each voxel value to a spatial coordinate and time instance. This information is sufficient to create a three dimensional and time dependent field of 3D vectors which represent the intra-ventricular blood flow patterns. This could be used as ground truth data for the output of the simulation pipeline if the pipeline were applied to the anatomical data. Because the anatomical data are in the same coordinate system as the above described MR-based vector field, the two fields to compare would already be in the same reference coordinate system.

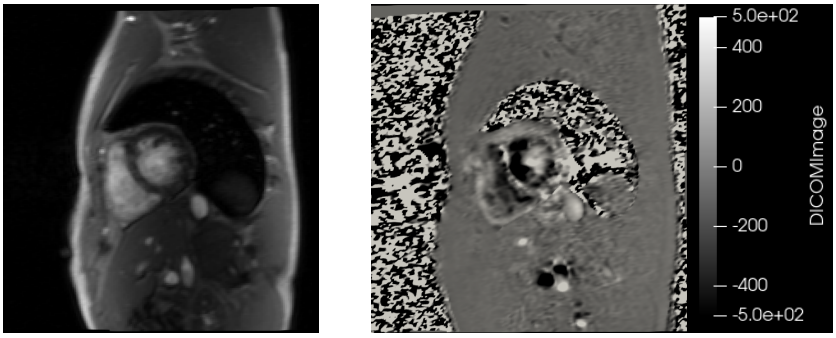

Figure 7.9: Two slices from the through-flow 2-slice SAX stack of subject number 1. **(a):** Anatomical contrast **(b):** Through flow **(c):** Legend for through flow in *(b)* in unconverted dicom values. The voxel values are converted to velocities by taking the velocity encoding (VENC) and the maximum bit depth of the voxel values into account.

Part III

Results and Discussion

CHAPTER 8

Results

This chapter is an extended presentation and discussion of the results presented in [Paper 2] . The methods and results are summarized in this chapter. Please refer to [Paper 2] in the appendix for the full descriptions.

The main result of this project is the validation of the pipeline based on phantom data. While defining and creating the simulation pipeline is part of answering the research questions defined in the objectives in Section 1.0.2, the validity of the answers rely heavily on the validity of the pipeline.

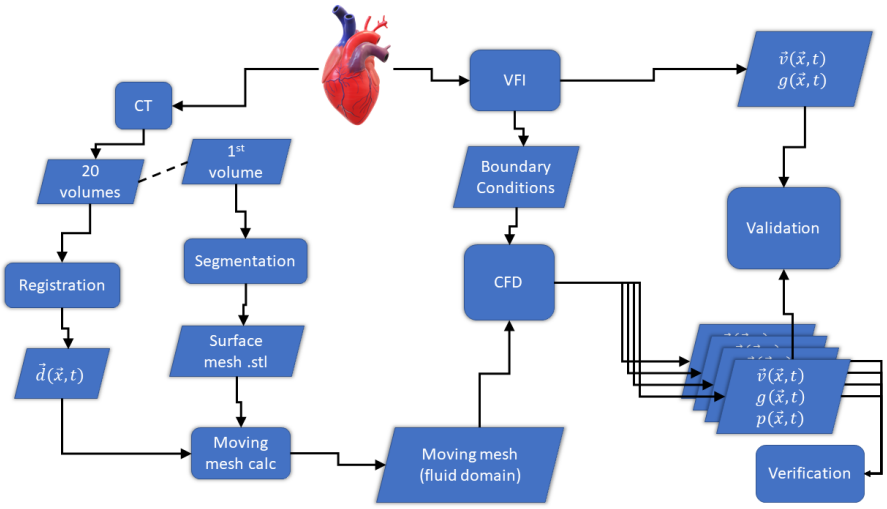

Figure 8.1: Flowchart of the procedures in the phantom study. Rectangular boxes are actions, slanted boxes are data. The flowchart includes the steps from Fig. 3.1, with the validation steps as well. The flowchart has been modified from [Paper 2] .

8.1 Summary of [Paper 2]

The purpose of the work in this paper is to propose a way of validating a pipeline like the one presented in Chapter 3 in a controlled and repeatable setup. This is achieved by applying the pipeline to the DHP (Chapter 4) and comparing the flow patterns produced by the pipeline with actual measurements of the flow patterns from ultrasound VFI. The validation strategy is sketched in the flowchart in Fig. 8.1. The input to the simulation pipeline is based on a CTA scan of the DHP and inlet conditions from the VFI measurements. The VFI measurement was done with the US transducer mounted in a sliding fixture. This made it possible relate all of the US acquisitions spatially to each other. The VFI data could be collected into 8 planes containing the time dependent, in-plane velocity components of the flow. The corresponding planes were exported from the simulation results (Fig. 7.6 and compared directly to the VFI measurements in MATLAB. A qualitative comparison was described, and a quantitative comparison was made by comparing velocity magnitudes in stationary regions of interest over time. The quantitative comparison is summarized in Fig. 8.4.

8.2 Qualitative Results

The output of the simulation is a time dependent flow field in three dimensions. The simulation contains information about geometry and pressure. This is the output defined in the flowchart in Fig. 8.1 as $\vec{v}(\vec{x}, t)$, for the velocity field, $g(\vec{x}, t)$ for geometry/domain information, and $p(\vec{x}, t)$ for pressure. To present the flow fields visually there is literally an infinite amount visualizations that qualitatively represents the flow patterns. As an example the visualizations on the cover of this thesis are presented in Fig. 8.2. Here, three different visualizations of the same volume at the same time instance have been plotted side by side. The left is a cut-plane where color indicate velocity magnitude. The center is a streamline representation with origin at the inlet and outlet. The color of the streamlines indicate velocity magnitude in the same color mapping as the cut-plane to the left. To the right is the computational mesh, where a portion of the boundary layers are plotted in red, and the tetrahedra are colored after quality of the computational mesh based on skewness of the individual mesh elements where green is highest quality and red is lowest quality. The prism elements at the boundary layer have been colored red with black edges and some of them have been removed to reveal the tetrahedral elements. While these plots subjectively look great on the cover of a thesis they are complicated to use for direct comparison.

For direct comparison it is often advantage to reduce the number of dimensions. In the qualitative comparison of [Paper 2] this is achieved by comparing a single slice at a single time instance from the pipeline and the VFI measurement respectively. This reduces the information to something that can be described by directions, magnitudes and trends, such as vortices. Some of the 2D plots from [Paper 2] have been reproduced in Fig. 8.3.

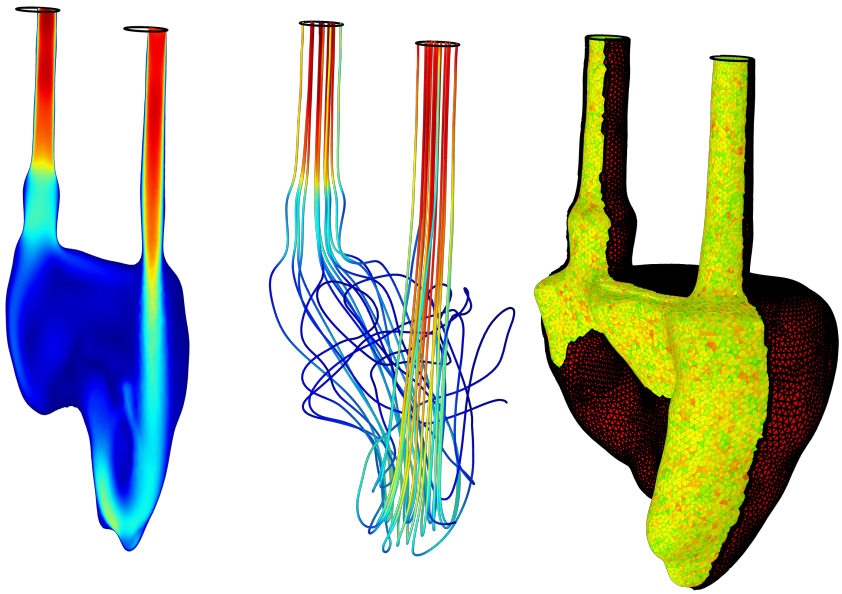

Figure 8.2: Three simulation visualizations from the dynamic heart phantom study in [Paper 2] . This plot is the same as the cover of the thesis. **Left:** Velocity magnitude in a single plane. **Center:** Streamlines from the inlet and outlet. The colors represent velocity magnitude with the same color map as for the plane (left). **Right:** Computational mesh; the boundary- and surface layers are red with black edges. The volumetric mesh (tetrahedrons) are colored after mesh quality where green is best and red is worst.

8.3 Quantitative Results

The quantitative results are obtained from the same philosophy of reducing dimensions. This is achieved in two ways. First, 16 regions of interest are chosen equally distributed between the 8 planes. Within each of the 16 regions of interest the mean velocity magnitude is calculated for every time instance, providing the curves seen in the right column of Fig. 8.5. Note that the VFI measurement is an average over several cycles, and therefore the mean velocity magnitude for the VFI regions of interest is reported as the mean value plus/minus one standard deviation. These curves can be compared directly and described qualitatively, see [Paper 2] , but for the quantitative analysis each of the curves are split into 11 separate time-bins. The mean value within each bin is calculated, which provides 11 velocities per region of interest of which there are 16, totaling in 176 velocities from the pipeline and 176 corresponding velocities from the VFI measurement.

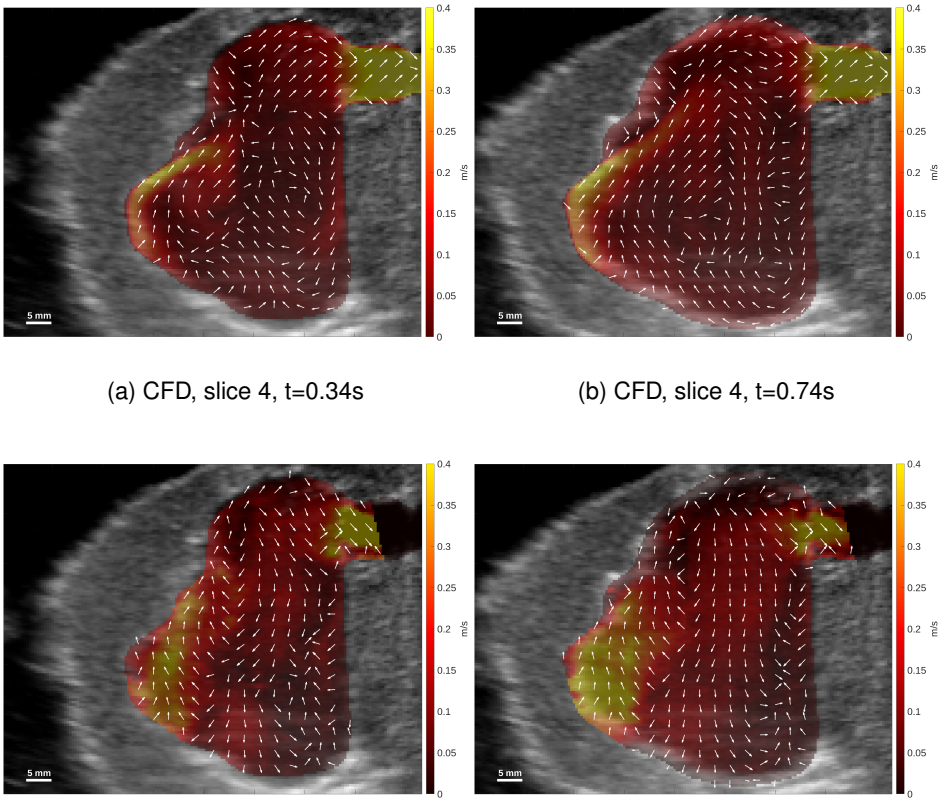

(a) CFD, slice 4, t=0.34s

(b) CFD, slice 4, t=0.74s

(c) VFI, slice 4, t=0.34s

(d) VFI, slice 4, t=0.74s

Figure 8.3: 2D slices from the pipeline (CFD) and VFI measurement for qualitative comparison. The colormap indicates velocity magnitude and arrows indicating the direction of flow. The full qualitative comparison of the plots are found in the pre-print in the appendix, see [Paper 2] . Modified from [Paper 2] .

These velocities are compared quantitatively by linear regression which are reported in Table 8.1 and Fig. 8.4. Note that the scatters from a single ROI (ROI#11) have been circled to indicate that they have been ignored in one of the analyses.

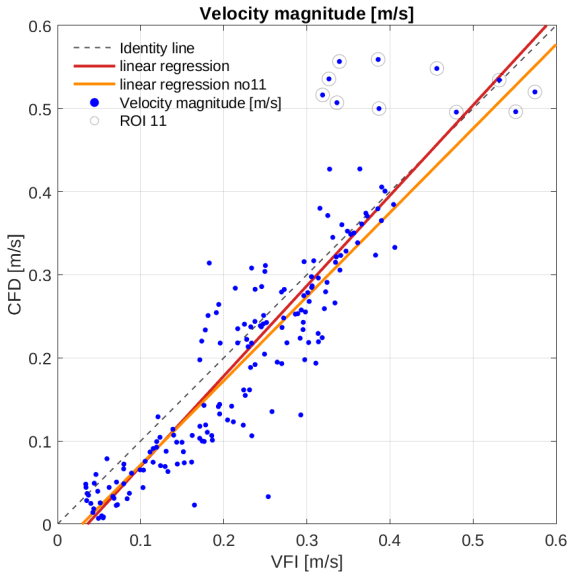

Figure 8.4: Scatter plot modified from [Paper 2] . The regression values are presented in table 8.1.

Table 8.1: Regression numbers

	R^2	intercept [m/s]	slope	SD [m/s]
All ROI's	0.8090	-0.0391	1.0861	0.0603
Excluding ROI#11	0.8227	-0.0299	1.0117	0.0482

8.4 Verification and Validation

The pipeline method is verified by the mesh independence study and cycle convergence study which are already presented in Sections 6.4.3 and 6.3.3.1.

The validation of the simulation is based on a both qualitative and quantitative comparison between the simulation and VFI measurement. For a more statistical approach, 16 regions of interest (ROI's) are chosen, and the time dependent spatial mean velocity magnitude within each ROI is divided into 11 non-overlapping time bins. These temporal means of the resulting 176 time bins are compared between CFD and VFI. See Fig. 8.4. The validation is quantified in a linear regression and a calculation of standard deviation (SD). The regression numbers are presented in table 8.1.

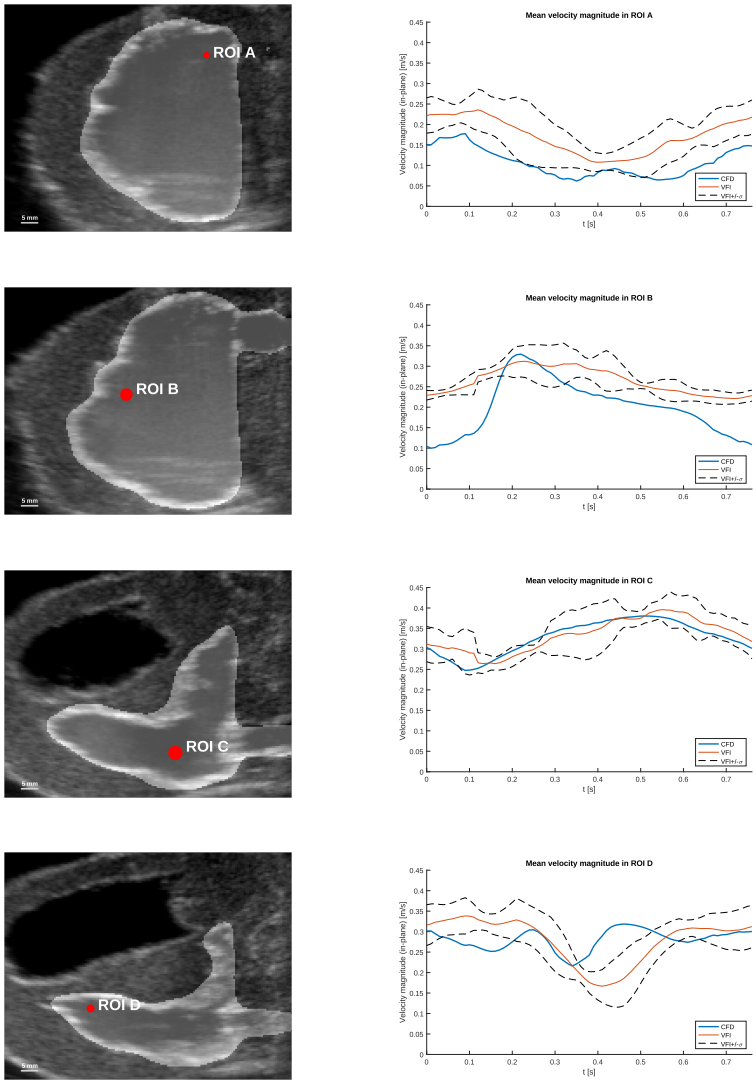

Figure 8.5: ROI placement and temporal velocity magnitude data for ROI's: A, B, C and D. **Left:** B-mode images with CFD fluid domain overlay. All at $t = 0$ s. The red dot represents the location of the ROI. **Right:** Mean velocity magnitude over time inside ROI for CFD and VFI. The VFI mean and standard deviation is based on averaging over 5 flow cycles. Modified from [Paper 2] .

8.5 Additional Considerations

It should be noted that the presented results here are based on the first run with the setup. When the pipeline is further improved this validation platform should be applied again to test the effectiveness of the improvements. The way the validation platform was used for these results has some limitations which were discovered during the process of application. These limitations are mentioned here. The inlet velocity in the setup was supposed to be constant to simplify the process of estimating the inlet boundary conditions as much as possible. However, because of the limitations of the DC pump that was available at the time, the inlet flow is actually pulsating with the contractions of the phantom ventricle because of the changing pump afterload. Furthermore, the water level of the blood mimicking fluid was too low which potentially could cause some unexpected changes in pressure in the ventricle afterload. This can be seen in Fig. 7.4. Because the inlet was not the expected constant 5 L/min the inlet boundary condition was based on the VFI measurement. This is of course not ideal as the VFI measurement is also used as ground truth in the comparison. These flow related issues have been mitigated in the new phantom setup as described in Chapter 4.

Additionally the choice of probe was made to measure on the largest area possible. This led to choosing a convex ultrasound probe over a linear ultrasound probe because the convex probe was able to visualize the entire long axis of the ventricular cavities of the DHP. However since the VFI acquisition had to be limited to a smaller region due to frame rate considerations, the linear probe would have been a better choice in two regards. One is that the linear probe is capable of producing better VFI results. The other is that the VFI results of the convex probe were found to be more difficult to post-process because of the ambiguity in spatial coordinates and vector directions due to the curvilinear grid in the convex probe.

Finally an important limitation in these results is that the VFI measurements are only two dimensional. Even though this is a limitation of the hardware used, the repeatability of the DHP movement could be combined with using the UR3 robot arm to measure perpendicular planes with very accurate spatial relationships to provide a thee dimensional flow field of three dimensional flow vectors instead of a three dimensional vector field of two dimensional flow vectors like the presented VFI measurement data.

Taking these additional comments into consideration will potentially enhance the performance of the pipeline substantially.

Part IV

Outro

CHAPTER 9

Discussion and Future Perspective

In this chapter the main points of the dissertation are summarized and discussed. Advantages and limitations of the pipeline are presented, discussed and the future perspective is outlined.

9.1 Discussion

A pipeline was developed and applied on a dynamic heart phantom. The DHP is seen as the simplest testable scenario for geometry prescribed CFD in terms of repeatability, measurability and complexity of the movement. The input data for the pipeline on the DHP was obtained by CTA. The pipeline results were compared to highly controlled ultrasound VFI measurements. The development of the pipeline included obtaining VFI data, obtaining CTA data, preprocessing of data, segmentation, volumetric image registration, CFD, and co-registration for comparison.

The main objective of the project was to develop a pipeline that combines several different fields of science. A big part of the workload has therefore been development and verification of methods that have not been used before. Because most of the methods were uncharted prior to the project it was not possible to predetermine which parameters should be optimized, and what results to produce other than a working pipeline. The main result in the project is the validation of the pipeline where the validation method itself is considered a novel contribution. The validation is based on comparison of the simulated velocity fields to experimentally acquired velocity data using VFI. This kind of qualitative and quantitative comparison is to the best of the authors knowledge still lacking in this field, even though the subject of geometry prescribed intra-cardiac flow simulations is already being researched with promising in-vivo applications, such as (Lantz et al. 2018). The work during the project has been focused on the technical side of the development and implementation, however a clinical point of view would have been invaluable to narrow the scope of the pipeline. Medical tests and measurements are seldom performed in the clinic without a specific purpose. In fact it is discouraged to prevent over diagnosis. The pipeline is at a mature state at this point, and simulations can be performed with relatively low effort, especially of the phantom. Reaching this state of maturity is a success for the project, however the pipeline is still a tool without

any specific use cases. Future work should indeed focus on clinical applications, so the best design choices can be made while there is still freedom to do so. Furthermore, a simulation is often better if the purpose of the simulation is specific and known at the time of the data acquisition. This segues into an important limitation of simulations which has a famous saying, although paraphrased slightly here, which is: "garbage in, garbage out". This saying has two important implications to the pipeline. First implication is that the input data are an extremely important part of the pipeline. If the input data acquisition method is not able to or optimal for capturing the desired phenomena, the quality of the simulation itself cannot make up for the low quality input data. An example of this is the choice between CTA and MRI for the moving geometry, where MRI averages over several hundred heart beats which could potentially diminish the small changes in flow that was sought to be simulated in the first place. It is therefore a good rule of thumb to know what the question is, before gathering data to answer it. This is where the view of the clinicians comes in. The second implication of "garbage in, garbage out" on the pipeline is the ability to capture the moving geometry accurately with the image registration framework. The reason the pipeline is referred to as a pipeline instead of a CFD simulation is because the numerical CFD framework cannot be evaluated by itself, as it is sensitive to the input. Now that the numerical framework is at a mature state, the future work should focus on improving the segmentation and registration framework in accordance with the clinical needs.

Creating a pipeline with a high number of inter-disciplinary components from scratch naturally involves many unknowns. Influential design choices in the pipeline have been made at a very early stage. This introduces the design paradox which states that the freedom to make design choices is high in the early stages, but rapidly declines when the process moves forward. This is because the pipeline components all affect each other, and changing one component often requires changes to others. The cost of modification increases when the process moves forward. Unfortunately, so does the knowledge about the pipeline and each of the components. Therefore very influential design choices were made at a time with little knowledge, and now that the knowledge is there, the freedom to make design choices is low, and the cost of implementing them high. This is the design paradox.

Limitations to the current pipeline The current implementation of the pipeline has known limitations that can be mitigated. As the pipeline was developed as a whole, no single segment has been optimized beyond the point of working reliably. Therefore all segments of the pipeline can be optimized. The segmentation has not been optimized or validated. This is because the segmentation of the phantom RV became trivial due to the high contrast between the contrast fluid and the rest of the phantom. That is not the case in-vivo, where segmentation is harder. This is especially true at the heart valves. Furthermore the moving geometry obtained from registration has not been formally validated. This could have been done by comparing the moving geometry at each time frame to a separate

segmentation of each volume at the same time frame. The current pipeline does not model heart valves although heart valves have a big influence on the flow patterns. This has not been necessary yet, as the DHP does not have any valves. This is a choice to keep the phantom validation as simple as possible at this point. It is of course something that needs to be addressed when applying the pipeline to in-vivo data. Instead of valves, the phantom inlet flow is driven by a DC pump which was very sensitive to afterload as well as other factors. In future experimental setups a calibrated gearhead pump is used. This will also add volume flow control to the setup which is going to be an advantage for future measurements.

Limitations to the geometry prescribed CFD Using the geometry prescribed CFD as the model type has the advantages of "capturing everything" without the need of acquiring data for everything and simulating interactions. The model type does however come with some limitations, some of which are directly related to the heart. One of the biggest concerns is the heart valve motion. To begin with it is challenging to obtain the valve motion, as the heart valves are too thin to be captured easily on CTA, and because they move to rapidly. To obtain the heart valve geometry and movement correctly in the current pipeline, it must be measured in a separate acquisition using another image modality such as US. To include the valve movement to the simulation it must then be added to the ventricle geometry which is complicated and causes issues related to time registration, spatial registration and even the fact that the valve motion is obtained at another time has a potential effect. Assuming all complications have been resolved, there is a great chance of over constraining the simulation with a prescribed valve movement as the valve is interacting with the fluid to a high degree. An alternative to prescribing a moving valve is to model the valves in another way. The flow across the valve annuli could be measured using VFI and used as boundary condition. Because the measured flow across the valve is a direct effect of the valve, this approach is likely to succeed. An alternative to measurement is modeling the inlet and outlet volume flows based on the volume change of the ventricle (Petersen 2019). Geometry prescribed CFD requires 4D data, however CTA usually only acquires a single volume in time at late diastole to reduce the dosage. Therefore the pipeline cannot be applied directly on existing data for other purposes, but another type of acquisition must be made which exposes the patient to a higher dosage. Even though the extra dosage is minimal with new dosage reduction techniques, the benefit of the pipeline has to be greater than the risk of the added exposure.

Limitations to the phantom validation The validation is performed using the current pipeline and therefore has the same limitations as described in Section 9.1. The limitations specific to the validation, including the measurements and comparison, are described in [Paper 2] . In summary, the biggest limitation is that the validation is performed on a phantom. The validation is therefore not sufficient to determine the performance of the pipeline in-vivo. There are several reasons for this. The simplified phantom movement

and the relatively simple ventricle geometry with a smooth endocardium are the most important reasons. These particular limitations are however a part of the strength of the phantom validation, as the number of variables is reduced, and the root cause of any issue can be isolated faster. The VFI acquisition has limitations as well. The biggest limitation is caused by the averaging over 42 separate acquisitions which are stitched together in post processing. The argumentation for allowing this is that the phantom movement is repeatable and has very low inter-measurement variability, however the actual inter-measurement variability has not been characterized formally yet. Another limitation in the validation related to the VFI measurement is that only in-plane flow velocities are measured, and only in parallel planes. The validation is therefore only in two of three dimensions that are simulated. This was necessary because of limitations to the setup at the time, however future measurements will incorporate the robot arm setup which has six degrees of freedom and can be automatized to measure orthogonal planes without losing precision. The VFI data were measured using a convex probe which has non optimal imaging qualities compared to the linear probe. The convex probe also caused other unexpected issues that needed to be attended. This is avoidable in the future by utilizing the linear probe instead. The metrics for comparison in [Paper 2] have been chosen to be as free of prejudice as possible. The idea is that the flow should be evaluated to be identical instead of optimizing the pipeline to a clinical parameter at this stage of development. This is an advantage at this stage, however the clinical relevance of this validation metric has not been investigated yet.

Regarding COMSOL The numerical framework is supposed to be a tool for solving the model, and nothing more. If the tool works, and if it is verified and validated, it generates almost identical results whether it is finite element, finite volume, COMSOL or STARCCM+. Using COMSOL as the tool has several advantages and disadvantages. The reason COMSOL was chosen as the tool is the already existing resources in form of technical assistance, both internally and externally, and experience from previous courses and projects at the university. COMSOL uses the finite element method which is not the typical discretization method for CFD, where the finite volume discretization is more popular, and often easier to work with. Using COMSOL makes it possible to expand physics, such as adding a FSI problem to the simulation. As the movement of the fluid domain is calculated as an elastic material, the multiphysics capabilities of COMSOL is already at play, even though the physics are not directly coupled in the solver. Furthermore, COMSOL is very flexible to different types of problems and inputs, which facilitates the modular approach of the development of the pipeline. A disadvantage of using COMSOL, and thereby finite element method, for CFD is that it requires more work to obtain a robust solution. This is however outweighed by the advantages, and the fact that COMSOL has several CFD specific features that are tuned to the purpose.

9.2 Future Perspectives

Providing patient specific blood flow pattern metrics based on existing cardiac medical imaging technology can potentially increase the number of early detections for various heart conditions. The whole premise of calculating the blood flow patterns based on imaging data that is already routinely collected in the clinic today has the potential to provide information to the clinicians that would otherwise require additional measurement to obtain. Depending on the future discoveries of clinical importance of intra-cardiac flow patterns this type of pipeline might one day be a cheap and non-discriminating screening tool for various diseases. Non-discriminating in the sense that an automated pipeline would be applied automatically to any applicable patient data, whereas extra measurements might only be provided for a certain high-risk group. The future discoveries of clinical implications of the itra-cardiac blood flow patterns cannot be predicted of course, however with better tools for estimation there is always the possibility of new discoveries. It has even been suggested that intra-ventricular blood flow patterns might detect so-called subclinical markers of impaired LV function (Eriksson et al. 2013) before the cardinal symptoms, which are often irreversible, begin to emerge. A very early detection could even help save lives by simply mitigating behavioral risk factors in time, thereby reducing the need for medications and invasive interventions.

The combination of the potential for automatic application on existing clinical workflows as a novel screening tool, together with the potential for very early detection of cardiovascular disease, makes the continued work on this type of pipeline a strong candidate for reducing the need for medical interventions and even saving lives otherwise lost to cardiovascular diseases.

CHAPTER 10

Conclusion

A geometry prescribed pipeline for estimating intra cardiac blood flow patterns from 4D images of the heart was developed and validated on a dynamic heart phantom.

The pipeline, including the phantom validation platform, is now at state where more complicated phantom cases, such as variations of torsion, compression and heart rate, can be explored. The further work on the pipeline should be focused on clinical application and optimization the volumetric image registration to obtain the most accurate representation of the moving geometry possible.

In conclusion, the pipeline was developed and implemented successfully. The pipeline produced similar flow patterns as a direct measurement in a phantom study. While geometry prescribed CFD of the human heart by itself is not novel, the novelty of this research lies in the validation platform which has the potential to acquire highly controlled high quality ground truth data. This is an essential tool for the development of a pipeline capable of exceeding the quality of the current state-of-the-art in-vivo methods.

Bibliography

References from Chapter 1

Eriksson, J., A. Bolger, T. Ebbers, and C. Carlhäll (2013). "Four-dimensional blood flow-specific markers of LV dysfunction in dilated cardiomyopathy". In: *European Heart Journal Cardiovascular Imaging* 14.5, pp. 417–424. DOI: 10.1093/ehjci/jes159. URL: https://www.scopus.com/inward/record.uri?eid=2-s2.0-84876559936%5C&doi=10.1093%2fehjci%2fjes159%5C&partnerID=40%5C&md5=76dc25290699614f2f6fea9208d8cb61 (cit. on pp. 3, 5).

Hong, G.-R., G. Pedrizzetti, G. Tonti, P. Li, Z. Wei, J. K. Kim, A. Baweja, S. Liu, N. Chung, H. Houle, and et al. (2008). "Characterization and quantification of vortex flow in the human left ventricle by contrast echocardiography using vector particle image velocimetry". In: *JACC: Cardiovascular Imaging* 1.6, pp. 705–717. DOI: 10.1016/j.jcmg.2008.06.008 (cit. on pp. 3, 4).

Hong, G. R., M. Kim, G. Pedrizzetti, and M. A. Vannan (2013). "Current Clinical Application of Intracardiac Flow Analysis Using Echocardiography". In: *Journal of Cardiovasc Ultrasound* 21.4, pp. 155–162. DOI: http://dx.doi.org/10.4250/jcu.2013.21.4.155 (cit. on p. 4).

Leipsic, J., T. Yang, A. Thompson, B. Koo, G. B. J. Mancini, C. Taylor, M. J. Budoff, H. Park, D. S. Berman, and J. K. Min (2014). "CT angiography (CTA) and diagnostic performance of noninvasive fractional flow reserve: results from the Determination of Fractional Flow Reserve by Anatomic CTA (DeFACTO) study". In: *American Journal of Roentgenology*, pp. 989–994 (cit. on p. 4).

Mohiaddin, R. H. (1995). "Flow patterns in the dilated ischemic left ventricle studied by MR imaging with velocity vector mapping". In: *J. Magn. Reson. Imaging*, pp. 493–498 (cit. on pp. 3, 4).

Norgaard, B., J. Leipsic, S. Gaur, S. Seneviratne, B. Ko, H. Ito, J. Jensen, L. Mauri, B. D. Bruyne, H. Bezerra, K. Osawa, M. Marwan, C. Naber, A. Erglis, S. Park, and E. Christiansen (2014). "Diagnostic performance of noninvasive fractional flow reserve derived from coronary computed tomography angiography in suspected coronary artery disease: The NXT trial (Analysis of Coronary Blood Flow Using CT Angiography: Next Steps)". In: *Journal of the American College of Cardiology* 63.12. cited By 463, pp. 1145–1155. DOI: 10.1016/j.jacc.2013.11.043.

URL: https://www.scopus.com/inward/record.uri?eid=2-s2.0-84896972430%5C&doi=10.1016%2fj.jacc.2013.11.043%5C&partnerID=40%5C&md5=14c716780b200c58d30d5bc4c40e5d76 (cit. on p. 4).

Organization, W. health (17 May 2017). *Cardiovascular diseases*. Accessed: 2019-11-28. URL: https://www.who.int/news-room/fact-sheets/detail/cardiovascular-diseases-(cvds) (cit. on p. 3).

Taylor, C. A., T. A. Fonte, and J. K. Min (2013). "Computational Fluid Dynamics Applied to Cardiac Computed Tomography for Noninvasive Quantification of Fractional Flow Reserve". In: *J. Am. Coll. Cardiol.* 61.22, pp. 2233–2241 (cit. on p. 4).

Zarins, C. K., C. A. Taylor, and J. K. Min (2013). "Computed fractional flow reserve (FFTCT) derived from coronary CT angiography". In: *J. of Cardiovasc. Trans. Res.*, pp. 708–714 (cit. on p. 4).

References from Chapter 2

Bellhouse, B. and F. Bellhouse (1969). "Fluid mechanics of the mitral valve". In: *Nature* 224.5219, pp. 615–616. DOI: 10.1038/224615a0. URL: https://www.scopus.com/inward/record.uri?eid=2-s2.0-0014668472%5C&doi=10.1038%2f224615a0%5C&partnerID=40%5C&md5=3dbafe8a1b30a3a1945fb9c315ede408 (cit. on p. 15).

Bellhouse, B. J. and F. H. Bellhouse (Jan. 1968). "Mechanism of Closure of the Aortic Valve". In: *Nature* 217, pp. 86–87. DOI: 10.1038/217086b0 (cit. on p. 15).

Bellhouse, B. J. and L. Talbot (1969). "The fluid mechanics of the aortic valve". In: *Journal of Fluid Mechanics* 35.4, pp. 721–735. DOI: 10.1017/S0022112069001406 (cit. on p. 15).

Caballero, A., W. Mao, L. Liang, J. Oshinski, C. Primiano, R. McKay, S. Kodali, and W. Sun (2017). "Modeling left ventricular blood flow using smoothed particle hydrodynamics". In: *Cardiovascular engineering and technology* 8.4, pp. 465–479 (cit. on p. 17).

Craene, M. D., G. Piella, O. Camara, N. Duchateau, E. Silva, A. Doltra, J. D'hooge, J. Brugada, M. Sitges, and A. F. Frangi (2012). "Temporal diffeomorphic free-form deformation: application to motion and strain estimation from 3D echocardiography". In: *Med Image Anal.*, pp. 427–450 (cit. on pp. 36, 37, 39).

Doost, S., D. Ghista, B. Su, L. Zhong, and Y. Morsi (2016). "Heart blood flow simulation: A perspective review". In: *BioMedical Engineering Online* 15.1, pp. 1–28. DOI: 10.1186/s12938-016-0224-8. URL: https://www.scopus.com/inward/record.uri?eid=2-s2.0-84983672153%5C&doi=10.1186%2fs12938-016-0224-8%5C&partnerID=40%5C&md5=22ec6a808d0a106530db8e333ed843db (cit. on p. 19).

Evans, C. J., M. I. G. Bloor, and M. J. Wilson (2001). "Parameterization of the Time-Dependent Geometry of the Heart for Steady Fluid Dynamical Analysis". In: *Journal of Theoretical Medicine* 3, pp. 221–230 (cit. on p. 34).

Fung, Y. C. (1990). *Biomechanics - Motion, flow, stress and growth*. Springer-Verlag, New York (cit. on p. 26).

Hunter, P., A. Pullan, and B. Smaill (2003). "Modeling total heart function". In: *Annual Review of Biomedical Engineering* 5. cited By 210, pp. 147–177. DOI: 10.1146/annurev.bioeng.5.040202.121537. URL: https://www.scopus.com/inward/record.uri?eid=2-s2.0-0642274852%5C&doi=10.1146%2fannurev.bioeng.5.040202.121537%5C&partnerID=40%5C&md5=d291762217df697307120c1c014f961d (cit. on p. 18).

Hvid, R. (2018). "Development of 3D simulation model of the heart for validation of vector flow imaging". MA thesis. Technical University of Denmark (cit. on pp. 23, 34, 35, 37).

Ibrahim, E. H. (2011). "Myocardial tagging by cardiovascular magnetic resonance: evolution of techniques–pulse sequences, analysis algorithms, and applications." In: *Journal of cardiovascular magnetic resonance : official journal of the Society for Cardiovascular Magnetic Resonance* 13. Cited by: 202; All Open Access, Gold Open Access, Green Open Access, p. 36. DOI: 10.1186/1532-429X-13-36. URL: https://www.scopus.com/inward/record.uri?eid=2-s2.0-84855179684%5C&doi=10.1186%2f1532-429X-13-36%5C&partnerID=40%5C&md5=976c84b17414b4d797dcbaf8db850cbc (cit. on p. 39).

Jensen, J. A. and P. Munk (1998). "A New Method for Estimation of Velocity Vectors". In: *IEEE Trans. Ultrason. Ferroelec. Freq. Contr.* 45.3, pp. 837–851. DOI: 10.1109/58.677749 (cit. on p. 21).

Keele, K. (1951). "Leonardo da Vinci, and the Movement of the Heart". In: *Journal of the Royal Society of Medicine* 44.3. cited By 8, pp. 209–213. DOI: 10.1177/003591575104400309. URL: https://www.scopus.com/inward/record.uri?eid=2-s2.0-67849104020%5C&doi=10.1177%2f003591575104400309%5C&partnerID=40%5C&md5=506db6680e87cd49b8a08f464a6ca7e7 (cit. on p. 15).

Khalafvand, S., E. Ng, and L. Zhong (2011). "CFD simulation of flow through heart: A perspective review". In: *Computer Methods in Biomechanics and Biomedical Engineering* 14.1. cited By 30, pp. 113–132. DOI: 10.1080/10255842.2010.493515. URL: https://www.scopus.com/inward/record.uri?eid=2-s2.0-79251516098%5C&doi=10.1080%2f10255842.2010.493515%5C&partnerID=40%5C&md5=ba575449c490d343e7a1c4fd747d053c (cit. on p. 19).

Lantz, J., V. Gupta, L. Henriksson, M. Karlsson, A. Persson, C. Carlhall, and T. Ebbers (2018). "Intracardiac flow at 4D CT: Comparison with 4D flow MRI". In: *Radiology* 289, pp. 51–58. DOI: 10.1148/radiol.2018173017. URL: https://www.

scopus.com/inward/record.uri?eid=2-s2.0-85054127151%5C&doi=10.1148%2fradiol.2018173017%5C&partnerID=40%5C&md5=490cfd909251371f0e1126f6265d659f (cit. on p. 18).

Lantz, J., L. Henriksson, A. Persson, M. Karlsson, and T. Ebbers (2016). "Patient-Specific Simulation of Cardiac Blood Flow From High-Resolution Computed Tomography". In: *J. Biomech. Eng.* 138, pp. 121004-1–121004-9. DOI: 10.1115/1.4034652 (cit. on pp. 18, 19).

Lopez-Perez, A., R. Sebastian, and J. M. Ferrero (Apr. 2015). "Three-dimensional cardiac computational modelling: methods, features and applications". In: *BioMedical Engineering OnLine* 14.1, pp. 1–31. DOI: 10.1186/s12938-015-0033-5. URL: https://doi.org/10.1186/s12938-015-0033-5 (cit. on pp. 16, 19).

Makela, T., P. Clarysse, O. Sipila, N. Pauna, Q. C. Pham, T. Katila, and I. E. Magnin (2002). "A review of cardiac image registration methods". In: *IEEE Transactions on Medical Imaging* 21.9, pp. 1011–1021 (cit. on p. 39).

Mao, W., A. Caballero, R. McKay, C. Primiano, and W. Sun (2017). "Fully-coupled fluid-structure interaction simulation of the aortic and mitral valves in a realistic 3D left ventricle model". In: *PloS One* 12.9, e0184729. DOI: 10.1371/journal.pone.0184729 (cit. on p. 17).

Markl, M., A. Frydrychowicz, S. Kozerke, M. Hope, and O. Wieben (2012). "4D flow MRI". In: *J. Magn. Reson. Imaging* 36.5, pp. 1015–1036 (cit. on p. 24).

MathWorks (2022). *Matlab documentation: imregdemons*. Online. Accessed: 2022-10-22. URL: https://se.mathworks.com/help/images/ref/imregdemons.html (cit. on pp. 31–33).

Mittal, R., J. H. Seo, V. Vedula, Y. J. Choi, H. Liu, H. H. Huang, S. Jain, L. Younes, T. Abraham, and R. T. George (2016). "Computational modeling of cardiac hemodynamics: Current status and future outlook". In: *Journal of Computational Physics* 305, pp. 1065–1082. DOI: 10.1016/j.jcp.2015.11.022. URL: http://www.sciencedirect.com/science/article/pii/S0021999115007627 (cit. on p. 19).

Multiphysics, C. (2017). *Finite Element Mesh Refinement*. Accessed: 2022-10-23. URL: https://www.comsol.com/multiphysics/mesh-refinement?parent=physics-pdes-numerical-042-32 (cit. on p. 29).

Munoz, D., M. Markl, J. Mur, A. Barker, C. Fernandez-Golfin, P. Lancellotti, and J. Gomez (2013). "Intracardiac flow visualization: Current status and future directions". In: *European Heart Journal Cardiovascular Imaging* 14.11, pp. 1029–1038. DOI: 10.1093/ehjci/jet086. URL: https://www.scopus.com/inward/record.uri?eid=2-s2.0-84885928303%5C&doi=10.1093%2fehjci%2fjet086%5C&partnerID=40%5C&md5=bfed090b6ef9544b333672c373b3db31 (cit. on p. 19).

Nishimura, D. (2010). *Principles of Magnetic Resonance Imaging*. Lulu Press, Inc. (cit. on p. 20).

O'Regan, D. (2020). "Putting machine learning into motion: applications in cardiovascular imaging". In: *Clinical Radiology* 75.1, pp. 33–37. DOI: 10.1016/j.crad.2019.04.008. URL: https://www.scopus.com/inward/record.uri?eid=2-s2.0-85065118291%5C&doi=10.1016%2fj.crad.2019.04.008%5C&partnerID=40%5C&md5=267e97462720970bdc3437307bc43c3d (cit. on p. 39).

OpenStax (2021). *Anatomy and Physiology: Heart Anatomy*. Online. Accessed: 2021-08-13. URL: https://openstax.org/books/anatomy-and-physiology/pages/19-1-heart-anatomy (cit. on pp. 11–14).

Pedrizzetti, G. and F. Domenichini (2014). "Left ventricular fluid mechanics: The long way from theoretical models to Clinical Applications". In: *Annals of biomedical engineering* 43.1, pp. 26–40 (cit. on p. 17).

Peskin, C. S. (1972). "Flow patterns around heart valves: A numerical method". In: *Journal of Computational Physics*, pp. 252–271. DOI: 10.1016/0021-9991(72)90065-4 (cit. on p. 17).

Peyrat, J., H. Delingette, M. Sermesant, C. Xu, and N. Ayache (2010). "Registration of 4D Cardiac CT Sequences Under Trajectory Constraints With Multichannel Diffeomorphic Demons". In: *IEEE Transactions on Medical Imaging* 29.7, pp. 1351–1368. DOI: 10.1109/TMI.2009.2038908 (cit. on pp. 36, 39).

Prince, J. L. and J. M. Links (2006). *Medical imaging signals and systems*. Pearson Prentice Hall Upper Saddle River (cit. on p. 20).

Sarrami-Foroushani, A., T. Lassila, M. MacRaild, J. Asquith, K. C. B. Roes, J. V. Byrne, and A. F. Frangi (2021). "In-silico trial of intracranial flow diverters replicates and expands insights from conventional clinical trials". In: *Nat. Commun.* 12, p. 3861. DOI: 10.1038/s41467-021-23998-w (cit. on p. 18).

Segars, W. P., D. Lalush, M. Benjamin, and W. Tsui (1999). "Namic heart phantom". In: *IEEE Transactions on Nuclear Science* 46.3 PART 2. cited By 218, pp. 503–506. DOI: 10.1109/23.775570. URL: https://www.scopus.com/inward/record.uri?eid=2-s2.0-0033343646%5C&doi=10.1109%2f23.775570%5C&partnerID=40%5C&md5=29df44049e4c6382bdd4d388f4f1d570 (cit. on p. 16).

Sengupta, P. P., G. Pedrizzetti, P. J. Kilner, A. Kheradvar, T. Ebbers, G. Tonti, A. G. Fraser, and J. Narula (2012). "Emerging trends in CV flow visualization". In: *JACC: Cardiovascular Imaging* 5.3, pp. 305–316. DOI: 10.1016/j.jcmg.2012.01.003 (cit. on p. 24).

Sotiras, A., C. Davatzikos, and N. Paragios (2013). "Deformable Medical Image Registration: A Survey". In: *IEEE Trans. Med. Imag.* 32.7, pp. 1153–1190 (cit. on p. 31).

Tavakoli, V. and A. A. Amini (2013). "A survey of shaped-based registration and segmentation techniques for cardiac images". In: *Computer Vision and Image Understanding* 117.9, pp. 966–989. DOI: https://doi.org/10.1016/

j.cviu.2012.11.017. URL: http://www.sciencedirect.com/science/article/pii/S1077314213000775 (cit. on p. 39).

Technology, K. I. of (2022). *Computational Models of the Heart*. Online. Accessed: 2022-10-22. URL: https://www.ibt.kit.edu/english/camo.php (cit. on p. 17).

Thirion, J. (1998). "Image matching as a diffusion process: an analogy with Maxwell's demons". In: *Medical image analysis* 2.3, pp. 243–260 (cit. on p. 38).

Vázquez, M., R. Arís, J. Aguado-Sierra, G. Houzeaux, A. Santiago, M. López, P. Córdoba, M. Rivero, and J. C. Cajas (2015). "Alya Red CCM: HPC-Based Cardiac Computational Modelling". In: *Selected Topics of Computational and Experimental Fluid Mechanics*. Ed. by J. Klapp, G. Ruíz Chavarría, A. Medina Ovando, A. López Villa, and L. D. G. Sigalotti. Cham: Springer International Publishing, pp. 189–207. DOI: 10.1007/978-3-319-11487-3_11 (cit. on p. 17).

Vedula, V., S. Fortini, J. Seo, G. Querzoli, and R. Mittal (2014). "Computational modeling and validation of intraventricular flow in a simple model of the left ventricle". In: *Theoretical and Computational Fluid Dynamics* 28.6. cited By 20, pp. 589–604. DOI: 10.1007/s00162-014-0335-4. URL: https://www.scopus.com/inward/record.uri?eid=2-s2.0-84914811530%5C&doi=10.1007%2fs00162-014-0335-4%5C&partnerID=40%5C&md5=d445575ac255899949eca1a719a5dd6b (cit. on pp. 16, 18).

Vercauteren, T., X. Pennec, A. Perchant, and N. Ayache (2009). "Diffeomorphic demons: Efficient non-parametric image registration". In: *NeuroImage* 45.1, pp. 61–72 (cit. on p. 38).

Zhong, L., J. Zhang, B. Su, R. Tan, J. Allen, and G. Kassab (2018). "Application of patient-specific computational fluid dynamics in coronary and intra-cardiac flow simulations: Challenges and opportunities". In: *Frontiers in Physiology*, pp. 1–17. DOI: 10.3389/fphys.2018.00742. URL: https://www.scopus.com/inward/record.uri?eid=2-s2.0-85049077345%5C&doi=10.3389%2ffphys.2018.00742%5C&partnerID=40%5C&md5=4c7aec16a50d126dbb2224d5fcc660a9 (cit. on pp. 17, 19).

References from Chapter 3

Hvid, R. (2018). "Development of 3D simulation model of the heart for validation of vector flow imaging". MA thesis. Technical University of Denmark (cit. on p. 48).

Petersen, P. H. (2019). "Effect of Boundary Conditions on the Prediction of Blood Flow Patterns in the Human Left Ventricle". MA thesis. Technical University of Denmark (cit. on p. 49).

Su, B., X. Wang, F. Kabinejadian, C. Chin, T. T. Le, and J. Zhang (2019). "Effects of left atrium on intraventricular flow in numerical simulations". In: *Computers in Biology and Medicine* 106, pp. 46–53. DOI: https://doi.org/10.1016/

j.compbiomed.2019.01.011. URL: https://www.sciencedirect.com/science/article/pii/S0010482519300113 (cit. on p. 49).

References from Chapter 4

LLC, B. S. (2022). *Visual Show Automation*. Online. Accessed: 2022-10-22. URL: https://www.brookshiresoftware.com/ (cit. on p. 52).

Zaja, A. (2020). "Development of a Bi-ventricular Heart Model". MA thesis. Technical University of Denmark (cit. on pp. 55, 56).

References from Chapter 5

Campello, V. M., P. Gkontra, C. Izquierdo, and K. Lekadir (2021). "Multi-Centre, Multi-Vendor and Multi-Disease Cardiac Segmentation: The M&Ms Challenge". In: *IEEE Trans. Med. Imag.*, pp. 1–12 (cit. on p. 60).

Evans, C. J., M. I. G. Bloor, and M. J. Wilson (2001). "Parameterization of the Time-Dependent Geometry of the Heart for Steady Fluid Dynamical Analysis". In: *Journal of Theoretical Medicine* 3, pp. 221–230 (cit. on p. 60).

Garreau, M. S. D. (2019). "Biomechanical Modelling of the Right Ventricle". MA thesis. Technical University of Denmark (cit. on p. 60).

Hvid, R. (2018). "Development of 3D simulation model of the heart for validation of vector flow imaging". MA thesis. Technical University of Denmark (cit. on p. 61).

MathWorks (2022). *Matlab documentation: imregdemons*. Online. Accessed: 2022-10-22. URL: https://se.mathworks.com/help/images/ref/imregdemons.html (cit. on p. 62).

Sundgaard, J., K. Juhl, K. Kofoed, and R. Paulsen (2020). "Multi-planar whole heart segmentation of 3D CT images using 2D spatial propagation CNN". In: *Proc. SPIE Med. Imag.* Vol. 11313, 113131Y:1–8. DOI: 10.1117/12.2548015 (cit. on p. 60).

Thirion, J. (1998). "Image matching as a diffusion process: an analogy with Maxwell's demons". In: *Medical image analysis* 2.3, pp. 243–260 (cit. on p. 64).

Vercauteren, T., X. Pennec, A. Perchant, and N. Ayache (2009). "Diffeomorphic demons: Efficient non-parametric image registration". In: *NeuroImage* 45.1, pp. 61–72 (cit. on p. 64).

Zaja, A. (2020). "Development of a Bi-ventricular Heart Model". MA thesis. Technical University of Denmark (cit. on p. 60).

Zhuang, X. (2013). "Challenges and methodologies of fully automatic whole heart segmentation: A review". In: *Journal of Healthcare Engineering* 4.3, pp. 371–407. DOI: 10.1260/2040-2295.4.3.371. URL: https://www.scopus.com/inward/record.uri?eid=2-s2.0-84885648585%5C&doi=10.1260%2f2040-2295.4.3.371%5C&partnerID=40%5C&md5=8ddbb7796e647fe830e1a1ec431044ae (cit. on p. 60).

References from Chapter 7

Garreau, M. S. D. (2019). "Biomechanical Modelling of the Right Ventricle". MA thesis. Technical University of Denmark (cit. on p. 82).

References from Chapter 9

Eriksson, J., A. Bolger, T. Ebbers, and C. Carlhäll (2013). "Four-dimensional blood flow-specific markers of LV dysfunction in dilated cardiomyopathy". In: *European Heart Journal Cardiovascular Imaging* 14.5, pp. 417–424. DOI: 10.1093/ehjci/jes159. URL: https://www.scopus.com/inward/record.uri?eid=2-s2.0-84876559936%5C&doi=10.1093%2fehjci%2fjes159%5C&partnerID=40%5C&md5=76dc25290699614f2f6fea9208d8cb61 (cit. on p. 105).

Lantz, J., V. Gupta, L. Henriksson, M. Karlsson, A. Persson, C. Carlhall, and T. Ebbers (2018). "Intracardiac flow at 4D CT: Comparison with 4D flow MRI". In: *Radiology* 289, pp. 51–58. DOI: 10.1148/radiol.2018173017. URL: https://www.scopus.com/inward/record.uri?eid=2-s2.0-85054127151%5C&doi=10.1148%2fradiol.2018173017%5C&partnerID=40%5C&md5=490cfd909251371f0e1126f6265d659f (cit. on p. 101).

Petersen, P. H. (2019). "Effect of Boundary Conditions on the Prediction of Blood Flow Patterns in the Human Left Ventricle". MA thesis. Technical University of Denmark (cit. on p. 103).

Paper 1

Validation Platform for Development of Computational Fluid Dynamics of Intra-Cardiac Blood-Flow

Rasmus Hvid, Jørgen Arendt Jensen, Matthias Bo Stuart, Marie Sand Traberg

Published in:
Proceedings of the IEEE International Ultrasonic Symposium 2019

Document Version:
Published

DOI:
10.1109/ULTSYM.2019.8925893

Validation Platform for Development of Computational Fluid Dynamics of Intra-Cardiac Blood-Flow

Rasmus Hvid, Jørgen Arendt Jensen, Matthias Bo Stuart and Marie Sand Traberg
Center for Fast Ultrasound, Department of Health Technology, Technical University of Denmark
2800 Kgs. Lyngby, Denmark

***Abstract*—This study is an initial evaluation of a validation platform for computational fluid dynamics (CFD) pipelines made for human intra-cardiac flow estimation. The pipelines use image-based prescribed geometry CFD from computed tomography angiography (CTA). In this study the CTA provides approximately 20 volumetric images within one cardiac cycle. The validation platform consists of a dynamic heart phantom which mimics the human heart in CTA and ultrasound (US) measurements. The flow inside the phantom right ventricle (RV) was measured using two methods: 1) a novel CFD pipeline applied using the CTA data (3D+time). 2) US vector flow imaging (VFI) measured directly on the phantom (2D+time). The CFD and VFI are compared quantitatively by comparing point evaluations (line averages) of the in-plane fluid velocity magnitude. The similarity of the line averages, assessed from plots, is found to be depending on the spatial position of the lines. Some positions are very similar in CFD and VFI and some are not. Furthermore a qualitatively comparison is made by plotting the corresponding 2D slices of the vector fields which confirms the quantitative assessment: the overall flow patterns are similar but not everywhere.**

I. Introduction

Intra-cardiac flow patterns have the potential to become an important metric in diagnosis and treatment of cardiovascular diseases in future medicine [1]. Currently the gold standard for estimating intra-cardiac flow patterns is magnetic resonance imaging (MRI) which has several drawbacks including price, acquisition time and relatively poor spatial resolution [2]. An alternative to MRI is ultrasound with the downside of practicality: it is hard to obtain a good signal through the surrounding tissue [3]. Lately image-based computational fluid dynamics (CFD) has realistically been competing in the field of patient-specific intra-cardiac flow estimation by offering the potential of better spatial and temporal resolution [4]. Here an expandable validation platform is demonstrated by presenting a validation of a CFD pipeline.

II. Methods

The velocity fields (blood flow patterns) in a dynamic heart phantom are estimated using two methods and the results are compared. The methods are CFD and VFI. For the purpose of this study the phantom movement is simplified to a cyclic compression. Because the programmed phantom movement has no beat-to-beat variation the inter-measurement variation is minimal. The CFD pipeline applied has not been described in the literature yet and is therefore presented in this paper.

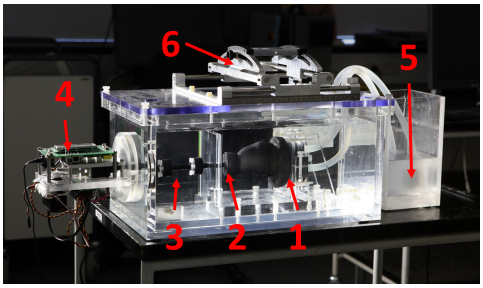

Fig. 1. Dynamic heart phantom (DHP) from Shelley Medical Imaging Technologies. **1:** PVA base **2:** PVA apex **3:** Actuator rod **4:** Servo motors and micro controller **5:** Blood-mimicking fluid reservoir **6:** Fixture for US probe where angle and position can be adjusted

A. Dynamic heart phantom setup

The phantom is a dynamic bi-ventricular heart phantom (DHP) from Shelley Medical Imaging Technologies (Toronto, Canada). The phantom has no heart valves. The phantom ventricles are made of polyvinyl alcohol (PVA) with additives. The additives make the ventricles appear as myocardium on computed tomography (CT) and ultrasound (US). The PVA heart is submerged in a water-filled tank and anchored at the base. Attached to the heart apex is an actuator rod which is attached to a servo motor. The servo motor is controlled from a programmable micro-controller. The micro-controller has three default output channels: compression, torsion and electrocardiography (ECG) output. The ECG output is used for synchronizing medical imaging. In this study only the right phantom ventricle is measured and simulated.

1) Phantom Flow: A constant inlet flow is applied through the right ventricle by a pump submerged in a reservoir of blood mimicking fluid. The flow rate is $\approx$ 5 L/min. See Fig. 1.

2) Phantom Movement: The movement programmed onto the micro-controller has three channels: compression, torsion

TABLE I
PHANTOM MOVEMENT SUMMARIZED

Function name	Function expression
Flow(t)	$5l/min$
Compression(t)	$sin(\pi t/T)^2 \cdot maxDisp$
Torsion(t)	0^o
ECG(t)	$\begin{cases} 1 & \text{if}(n \cdot T) \leq t \leq (n \cdot T + 0.1s) \\ 0 & \text{otherwise} \end{cases}$
for	$n = 0, 1, ..., N_{cycles}$ $T = 0.8s$

and ECG output. Furthermore the flow rate can be programmed as a fourth channel. For the simplified movement in this study two channels were used: compression and ECG output. The compression follows a squared sine function with 14mm amplitude and a frequency of 75 beats per minute (similar to Fig. 2). The ECG was programmed as a narrow rect function. The functions are summarized in table I where T is the cardiac cycle period and $maxDisp$ is the maximum displacement of the heart phantom apex.

B. Geometry

The geometry used for the simulation is a segmentation of a Computed Tomography Angiography (CTA) scan of the heart phantom.

1) Computed tomography: A CTA was performed on the phantom using a Canon (TOSHIBA) Aquilion ONE scanner. The cardiac cycle is defined as the R-R interval on the ECG and split into 20 phases corresponding to 5% increments (from 0% to 95%). The spatial resolution of the CTA reconstruction used for this study results in a voxel size of : $(x, y, z) = (0.6, 0.6, 0.5)mm^3$ with no overlap. The temporal resolution is 20 phases per heart cycle which results in a sample period of 0.8s/20 = 0.04s. This corresponds to a volume rate of 25Hz. Contrast fluid was added to the blood mimicking fluid before the CTA. The contrast fluid increases the contrast between blood and surrounding tissues which eases segmentation. This is the same procedure as for in-vivo CTA.

2) Moving fluid domain: The fluid domain is defined by an imported surface mesh from segmentation of the CTA. The 80% phase (frame #17 out of 20) where the phantom compression is minimal is used for this study. The movement is prescribed to this surface by a simplified linear deformation exclusively in the z-direction and a maximum displacement at the apex of 10mm ($zDisp$ in (2)). Note that 10mm displacement of the fluid domain's apex roughly corresponds to a 14mm displacement of the PVA's apex. The volumetric mesh nodes are smoothed corresponding to the surface movement. The simplified prescribed movement is verified by comparing the deformed geometry with the respective CTA segmentation in plots.

C. Computational fluid dynamics

The CFD pipeline is solved numerically in COMSOL Multiphysics v5.4 (COMSOL AB Stockholm, Sweden). Here the

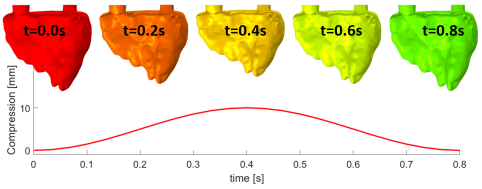

Fig. 2. Illustration of the fluid domain (right ventricle) surface compression. **Top:** RV surface at t= 0[s], 0.2[s], 0.4[s], 0.6[s], 0.8[s]. **Bottom:** Compression of the RV apex over 1 cycle (see (2))

incompressible Navier-Stokes equations

$$\rho\left(\frac{\partial \vec{u}}{\partial t} + (\vec{u} \cdot \nabla)\vec{u}\right) = -\nabla p + \eta \nabla^2 \vec{u} \tag{1}$$

$$\nabla \cdot \vec{u} = 0$$

are solved numerically assuming isothermal laminar flow. The blood mimicking fluid is assumed to be Newtonian.

In (1) $\vec{u}$ is the fluid velocity vector (m/s), t is time (s), p is pressure (Pa), $\rho = 1060kg/m^3$ is the fluid density and $\eta = 3.5$mPa·s is the fluid viscosity. ∇ is the del operator and ∇^2 is the Laplace operator.

1) Studies: The simulation is split into several studies to save computational resources and making the simulation solutions more stable.

Study 1: mesh movement

This study solves the spatial position of every mesh node for a single cycle. The movement is prescribed to the *wall* (see Fig.3) as a displacement function (see (2)). The function is periodic, so the mesh nodes on the *wall* will always end exactly where they started. The positions of the mesh nodes inside the fluid domain is computed using Yeoh smoothing. The position and velocity of each mesh node are stored between t=0s and t=0.8s for each timestep of Δt=0.01s. These positions are re-used in all of the subsequent cycles (studies 3-8).

$$dz(Z, t) = \frac{z}{lHeart} zDisp \cdot sin\left(\frac{t\pi}{T}\right)^2 \tag{2}$$

in (2) (x, y, z) are coordinates in the spatial frame of reference and (X, Y, Z) are coordinates in the material frame of reference. T=0.8s is the time period, $lHeart$=60mm is the approximate length of the RV-cavity and $zDisp$=10mm is the maximum displacement at the RV-cavity apex.

Study 2: initial conditions for first cycle

The choice of initial conditions has a great influence on how fast the solution converges. Poorly chosen initial conditions can make a model solution unstable and even unsolvable. Therefore instead of applying inlet flow on "zero pressure, zero velocity" initial conditions, the inlet flow is ramped up from 0 L/min to

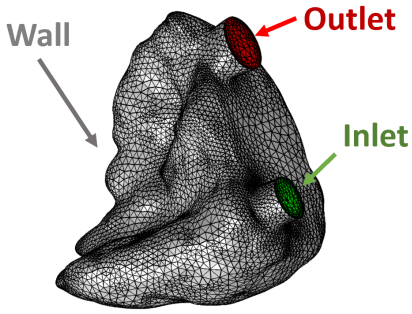

Fig. 3. Surface mesh (mesh size: "Normal") of the phantom right ventricle. The boundary types are collared: **Gray:** Wall **Green:** Inlet **Red:** Outlet

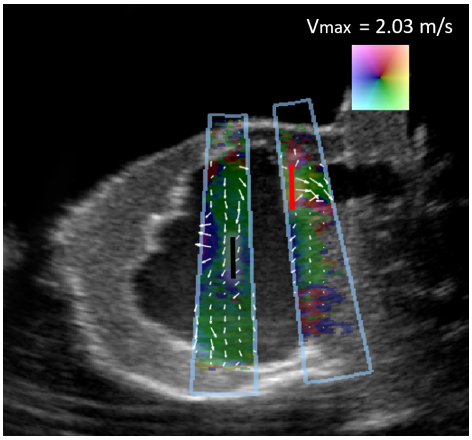

Fig. 4. A B-mode US image with VFI overlay from two separate acquisition. All three are from the 0% cardiac phase at minimum compression.

5 L/min over a time period of $\approx$ 0.8s. The outlet is defined as constant pressure p=0Pa. In this study the wall is stationary in the t=0s configuration from Study 1. The boundary condition on the wall is zero slip which in the stationary geometry corresponds to $\vec{u}$=0 at the *wall*. The time stepping is free, and only the last time frame is saved.

Study 3: cycle 1

This study computes the CFD of the moving geometry nodes (from study 1) using the initial conditions calculated in the previous study: study 3 uses the last time step of Study 2 as initial conditions. The boundary conditions are as follows:

Inlet Fully developed, constant inlet flow (5 L/min).

Outlet Normal flow, zero pressure.

Wall Zero slip: $\vec{u}_{fluid} = \vec{u}_{wall}$ at the wall.

Study 4: cycle 2

Same study type as study 3 except the initial conditions for study 4 is the last time frame from study 3. This procedure is followed for as many subsequent cycles necessary. The simulation is run for up to 6 cycles, or until the solution is converging towards the same periodic flow field. The solution in this paper is the 6th cycle repeated.

TABLE II
CFD KEY NUMBER AND RESOURCES

Boundary elements	13 878
Total elements	152 512
Computation time	1h 18m 7s
Resources for 8 studies (6 cycles)	2x Intel Xeon CPU E5-2660 v3 2 sockets, 20 cores, 2.60 GHz Available memory: 128.65 GB

2) Meshing: COMSOL has a built in automatic mesh function with a set of 9 pre-defined sizes (extremely coarse to extremely fine) which takes into account the type of physics solved for. In this simulation the physics is "fluid dynamics". In previous work [5] solutions from the mesh sizes "fine" and "normal" are within 2% in a mesh independence study. The mesh size for this study has been set to "normal" based on this. The mesh (surface elements only) is plotted in Fig. 3.

D. Vector Flow Imaging

VFI is measured using a modified BK5000 scanner and a 6C2 convex array probe (BK Medical, Herlev DK) mounted in a sliding fixture for capturing multiple parallel planes with 5mm intervals. Several acquisitions are made of each plane to obtain a higher frame rate. For full area flow estimations the frame rate is only $\approx$ 4Hz, for smaller areas of flow estimation the frame rate is $\approx$ 16Hz which is more appropriate for capturing the intra cardiac fluid dynamics. Examples of the smaller areas of VFI are seen in figure 4.

III. Results

A. Qualitative comparison

Initially the vector fields are compared qualitatively slice by slice. This is done by visual comparison of 2D+t vector fields. The overall flow patterns are found to be similar, but with variations. See figure 5.

B. Quantitative comparison

Several one-dimensional and time-dependent metrics are extracted from the estimations and compared. These metrics are point evaluations and "line averages". The line average is a better suiting metric to compensate for the roughly estimated co-registration in this study. In this paper two line averages are shown for 5 cycles. See Fig. 4, 5(a) and 6.

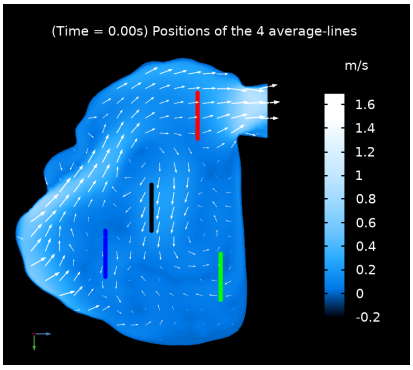

(a) CFD

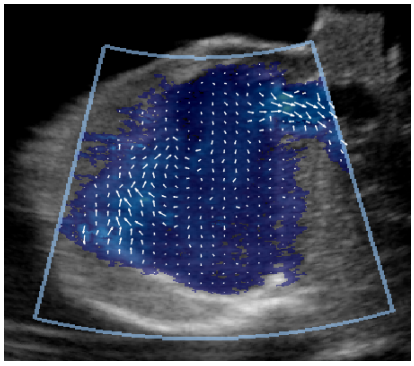

(b) VFI

Fig. 5. **a:** Slice from CFD. Colorbar is in-plane velocity magnitude. The average lines plotted in Fig. 6 is marked in red and black respectively. **b:** VFI of the same slice approximately at the same phase of the cardiac cycle.

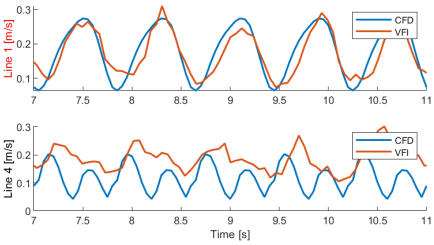

Fig. 6. Line averages of the in-plane velocity magnitude from images in Fig. 4 and 5(a)

IV. Discussion

Finding a suiting metric for validating a complex flow in 3D+time is not an easy task. In this study some points/lines have been selected, but a more global evaluation is preferable for validation purposes. As the simulation model is still being developed any mismatch between the VFI and CFD might be because of a CFD error.

A. Limitations/considerations

The valve-less phantom flow is not directly comparable to the in-vivo flow. The accuracy of the prescribed movement has not been verified. In future CFD pipelines, volumetric image registration will be used to estimate the wall movement directly. Co-registration has not been done precisely for this initial study although the validation setup has the potential for precise co-registration. Furthermore the inlet and outlet tubes have been cut relatively close to the phantom geometry. The effects of this has not yet been investigated.

V. Conclusion

To test the feasibility of further developing a phantom based validation platform the phantom intra-ventricular flow dynamics were measured using two methods. The methods show similarities both qualitatively, by visual comparison of slices, and quantitatively by comparing time dependent point evaluations of the velocity field.

Acknowledgment

The authors would like to thank Klaus F. Kofoed (MD, Ph.D, DmSc Department of Cardiology, Rigshospitalet, University of Copenhagen) for making the CTA data acquisition possible.

References

[1] L. Zhong, J. Zhang, B. Su, R. Tan, J. Allen, and G. Kassab, "Application of patient-specific computational fluid dynamics in coronary and intra-cardiac flow simulations: Challenges and opportunities," *Frontiers in Physiology*, pp. 1–17, 2018. [Online]. Available: https://www.scopus.com/inward/record.uri?eid=2-s2.0-85049077345\&doi=10.3389%2ffphys.2018.00742\&partnerID=40\&md5=4c7aec16a50d126dbb2224d5fcc660a9

[2] S. Doost, D. Ghista, B. Su, L. Zhong, and Y. Morsi, "Heart blood flow simulation: A perspective review," *BioMedical Engineering Online*, vol. 15, no. 1, pp. 1–28, 2016. [Online]. Available: https://www.scopus.com/inward/record.uri?eid=2-s2.0-84983672153\&doi=10.1186%2fs12938-016-0224-8\&partnerID=40\&md5=22ec6a808d0a106530db8e333ed843db

[3] D. Munoz, M. Markl, J. Mur, A. Barker, C. Fernandez-Golfin, P. Lancellotti, and J. Gomez, "Intracardiac flow visualization: Current status and future directions," *European Heart Journal Cardiovascular Imaging*, vol. 14, no. 11, pp. 1029–1038, 2013. [Online]. Available: https://www.scopus.com/inward/record.uri?eid=2-s2.0-84885928303\&doi=10.1093%2fehjci%2fjet086\&partnerID=40\&md5=bfed090b6ef9544b333672c373b3db31

[4] J. Lantz, L. Henriksson, A. Persson, M. Karlsson, and T. Ebbers, "Patient-specific simulation of cardiac blood flow from high-resolution computed tomography," *J. Biomech. Eng.*, vol. 138, pp. 121 004–1–121 004–9, 2016.

[5] R. Hvid, "Development of 3d simulation model of the heart for validation of vector flow imaging," MSc Thesis, Technical University of Denmark, 2018.

Paper 2

Intra-Cardiac Flow from Geometry Prescribed Computational Fluid Dynamics: Comparison with Ultrasound Vector Flow Imaging

Rasmus Hvid, Jørgen Arendt Jensen, Matthias Bo Stuart, Marie Sand Traberg

Name of journal:
Cardiovascular Engineering and Technology (CVET)

Document Version:
Second version, in review. First version is accepted with major revisions.

Intra-Cardiac Flow from Geometry Prescribed Computational Fluid Dynamics: Comparison with Ultrasound Vector Flow Imaging

Abstract

Purpose: This paper investigates the accuracy of blood flow velocities simulated from a geometry prescribed computational fluid dynamics (CFD) pipeline by applying it to a dynamic heart phantom. The CFD flow patterns are compared to a direct flow measurement by ultrasound vector flow imaging (VFI). The hypothesis is that the simulated velocity magnitudes are within one standard deviation of the measured velocities.

Methods: The CFD pipeline uses computed tomography angiography (CTA) images with 20 volumes per cardiac cycle as geometry input. Fluid domain movement is prescribed from volumetric image registration using the CTA image data. Inlet and outlet conditions are defined by the experimental setup. VFI is systematically measured in parallel planes, and compared to the corresponding planes in the simulated time dependent three dimensional fluid velocity field.

Results: The measured VFI and simulated CFD have similar flow patterns when compared qualitatively. A quantitative comparison of the velocity magnitude is also performed at specific regions of interest. These are evaluated at 11 non-overlapping time bins and compared by linear regression giving R^2 = 0.809, SD = 0.060 m/s, intercept = -0.039 m/s, and slope = 1.09. Excluding an outlier at the inlet, the correspondence between CFD and VFI improves to: R^2 = 0.823, SD = 0.048 m/s, intercept = -0.030 m/s, and slope = 1.01.

Conclusion: The direct comparison of flow patterns shows that the proposed CFD pipeline provide realistic flow patterns in a well-controlled experimental setup. The demanded accuracy is obtained close to the inlet and outlet, but not in locations far from these.

Keywords: Intra-cardiac hemodynamics, computational fluid dynamics, geometry prescribed motion, ultrasound blood flow imaging

Authors:
Rasmus Hvid[1], ORCID: 0000-0002-5070-9048
Matthias Bo Stuart[1], ORCID: 0000-0003-0809-530X
Jørgen Arendt Jensen[1], ORCID: 0000-0002-7896-3136
Marie Sand Traberg[1] *, ORCID: 0000-0001-7090-6607

[1] Department of Health Technology, Technical University of Denmark, 2800 Kongens Lyngby, Denmark
* Corresponding author e-mail: Marie Sand Traberg, msene@dtu.dk

Statement and declarations:
Rasmus Hvid, Matthias Bo Stuart, Jørgen Arendt Jensen and Marie Sand Traberg declares that they have no conflict of interest. This study has received funding from Innovation Fund Denmark (Grant no. 29035695). The authors would like to thank Klaus F. Kofoed (MD, PhD, DmSc Department of Cardiology, Rigshospitalet, University of Copenhagen) for making the CTA data acquisition possible.

1 Introduction

Intra-cardiac blood flow patterns have been simulated since the 1970's by modelling simplified ventricle geometries [1, 2]. Since medical imaging and computational power have become more available, models and simulations of intra-cardiac blood flow patterns have been competing with direct measurement for obtaining patient-specific intra-cardiac blood flow patterns.

In recent years intra-cardiac blood flow patterns have been investigated as a potential clinical tool for diagnostics and decision-aid. Current methods are variations of ultrasound [3, 4, 4–6] and cardiac magnetic resonance (CMR), which has several different sequences ranging from 2D phase contrast to the state-of-the-art 4D flow CMR [7, 8] are used. 4D flow CMR is considered state of the art for obtaining intra-cardiac blood flow patterns, but the method has the disadvantages of long acquisition times, averaging effects over multiple heart beats, and insufficient spatial and temporal resolution [7]. However, researchers have already correlated intra-cardiac blood flow patterns with pathology using flow-based metrics like vortex size and intensity [8] and changes in fractions between the flow types; direct flow, retained inflow, delayed ejection flow, and residual volume [9].

Computational fluid dynamics (CFD) models can estimate intra-cardiac blood flow patterns, and the metrics mentioned above can be derived from a simulation model as an alternative to direct measurement. Cardiac CFD models have advantages over direct measurement. In echocardiography current systems do not show the full velocity field in 3D with the 3D velocity vector, and, thus, do not reveal the whole picture of the ventricular flow. But in CFD models the data describing the full velocity field in 3D over time are available in any point at any time instant during the cardiac cycle. In 4D flow CMR imaging data are obtained by averaging up to several hundred heart beats, whereas the geometry for the presented CFD model is obtained from computed tomography angiography (CTA) where only a few cardiac cycles are required to reconstruct the geometry using a low radiation dose [10]. Furthermore, as previously mentioned, 4D flow CMR is limited by spatial and temporal flow resolution, where the resolution in both time and space of a simulation model is only limited by computer hardware and simulation time.

Simulation models are most effective and efficient when designed to a specific purpose, and therefore many modelling approaches have been developed for simulating intra-cardiac blood flow patterns. Doost et al. [11] presents an overview of common strategies for modelling cardiac flow. Choosing a strategy is based on data availability to feed the model and computational resources in terms of hardware and software. Since the heart phantom used in this study is compatible with ultrasound imaging and CTA, a dynamic patient-specific CFD model with geometry prescribed wall movement is chosen as the model approach. In addition, the formulation for handling the moving boundaries is based on the Arbitrary Lagrangian-Eulerian (ALE) formulation.

Validation of results achieved with i.e. in vivo patient-specific CFD simulations is difficult to perform for three main reasons. Firstly, what CFD simulations potentially offer is not always measurable using the current state-of-the-art methods. Second, the inter-measurement variability on the subjects blood flow patterns is confounded with the differences caused by the measurement method [12]. Lastly, acquiring in vivo data has limitations as described above. Despite its difficulties, in vivo studies have already been conducted by others, comparing patient-specific CFD simulations with the clinical state-of-the-art flow methods, reporting promising results [13, 14]. Lantz et. al. [14] compares metrics such as kinetic energy, stroke volume, etc. While the study shows correlation on important metrics, the data are still limited by inter-measurement variability and measurement limitations. The dynamic heart phantom setup utilised here allows for controlled and systematic high quality ultrasound measurements based on vector flow imaging (VFI) [15, 16] with precisely defined spatial relationships in a repeatable setup. VFI provides 2D vector velocity fields acquired in real-time, where quantitative data can be extracted from everywhere in the image. Therefore, it is ideal for comparison to simulated flow data in the heart as performed here.

This paper describes and applies a geometry prescribed CFD pipeline on a dynamic heart phantom with the purpose of validating the flow dynamics obtained from the pipeline.

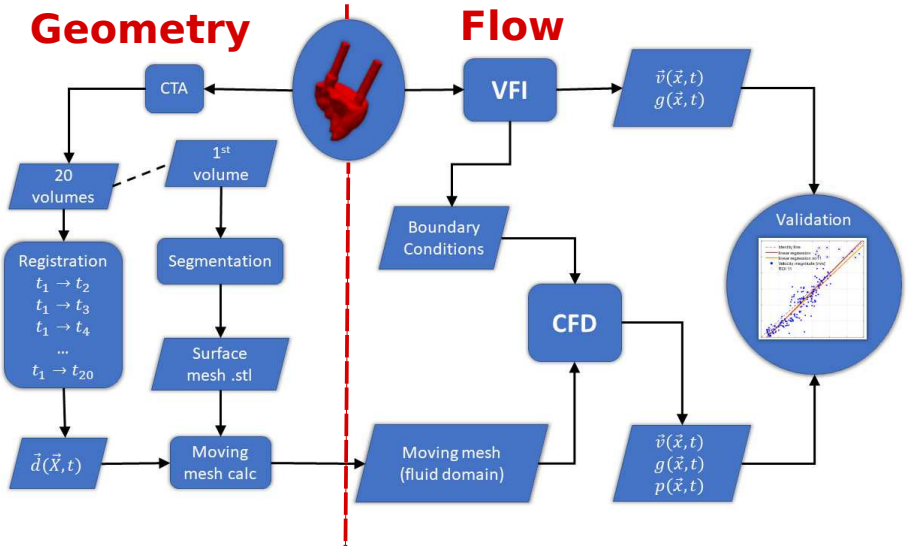

Fig. 1: Method flowchart for the CFD pipeline, where the part to the left of the red dashed line concerns the geometry, and the part to the right of the red dashed line concerns the flow simulation. The center is the lumen of the heart phantom visualised in red. The phantom is imaged by CTA and VFI to obtain boundary conditions for the CFD simulation and velocity data for validation. Rounded corners on the boxes represent methods of data processing. Sharp corners represent data sets and the circles indicates input (the heart phantom) and output (result of the validation). In the flowchart $g(\vec{x},t)$ represent the geometry, here the B-mode for the VFI and domain index for the CFD. The motion obtained from registration is labelled $\vec{d}(\vec{X},t)$, and $\vec{v}(\vec{x},t)$ is the velocity field. $p(\vec{x},t)$ represents the pressure field

It is hypothesised that the results of the CFD pipeline proposed here, i.e. the flow patterns and quantities, can accurately model the physical intra-ventricular flow. The model is considered accurate if the computed flow is within one standard deviation of the measured flow, i.e. the experimental VFI reference. This would show that the output of the pipeline is reliable and that the pipeline can be applied to in vivo cases.

The paper is organised as follows. In Section 2 a complete description of the applied methods is provided. It includes the individual elements of the pipeline starting out with the dynamic heart phantom, then the data acquisition with CTA and VFI is presented followed by a description of the CFD simulation details. Hereafter, the results are presented in Section 3 and discussed in Section 4. The paper is concluded in Section 5.

2 Methods

An overview of the CFD pipeline is presented as a flow chart in Fig. 1. The following presents the individual elements of the CFD pipeline and how the information is used to obtain the results.

2.1 Dynamic Heart Phantom

The CFD pipeline is applied to a dynamic biventricular heart phantom (DHP) from Shelley Medical Imaging Technologies (Toronto, Canada). The DHP wall surrounding the two ventricles is made of polyvinyl alcohol with additives, and the phantom has no heart valves. The additives make the ventricle walls appear similar to the myocardium on computed tomography images and during ultrasound scans. The DHP is submerged into a water-filled tank and anchored at the base, see Fig. 2.

An actuator rod is attached to the apex of the heart phantom, and two servo motors are attached

to the actuator rod, one pushing the rod introducing a compression and one rotating the rod introducing a torsional movement of the heart phantom. The servo movement is programmed on a micro-controller, which has three default output channels: compression, torsion and electrocardiography (ECG) output. The movement prescribed to the DHP here is a pure compression of 10 mm along the long-axis without rotation. This is a simplification of the in vivo cardiac motion where both compression and rotation are seen. The ECG output facilitates synchronisation in time, see Fig. 3, and is used for time synchronisation with the CTA. In this study only the right ventricle (RV) is measured and simulated.

In Fig. 3 two flow cycles are visualised, however in the experimental setup the movement runs for several hundred cycles to ensure periodic flow patterns independent of initial conditions at the time of measurement. A micro-controller was programmed to provide motor inputs to move the actuator rod according to:

$$c(t) = C_d \sin^2\left(\frac{\pi \cdot t}{0.8\,\mathrm{s}}\right), \qquad (1)$$

which corresponds to a compression of $C_d = 10$ mm every 0.8 s, i.e. 75 beats per minute. The actual flow cycle period was measured to be 0.76 s in both CTA and ultrasound measurements. The reason for this discrepancy is unknown. Since the two different measurements agree, a cycle period 0.76 s is assumed in the VFI processing and in the CFD model, as this represents the real conditions most accurately.

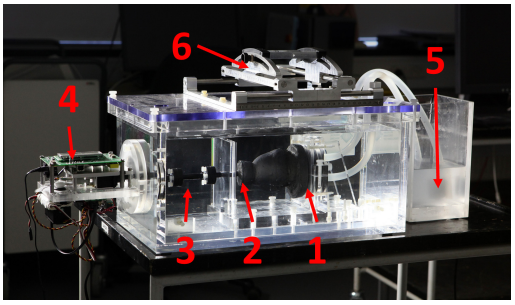

Fig. 2: Photograph of the DHP [17]. **1:** Base of the heart phantom with inlet and outlet tubing. **2:** Apex of the DHP. **3:** Actuator rod for transfer of motion. **4:** Servo motors and micro-controller to apply the motion. **5:** Fluid reservoir. **6:** Fixture for the ultrasound probe where angle and position is adjusted

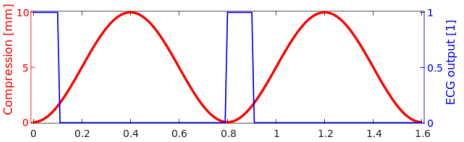

Fig. 3: Movement as prescribed to the micro-controller and applied to the phantom. **Red:** Compression applied to the actuator rod. **Blue:** The ECG output for time synchronisation in CTA

During the gathering of imaging data and flow measurements, blood mimicking fluid [18] is circulated through the ventricle inlet and out of the outlet via tubes from a fluid reservoir, see Fig. 2. The flow is governed by an impeller pump (Aqua Nova NBF-300, Aqua Nova, Poland) submerged into the fluid reservoir. The pump provides a constant flow rate, which is quantified in the phantom inlet using VFI, see Sec. 2.4. The peak volume flow rate at the RV inlet is 2.21 L/min. The total fluid volume in the phantom ventricle, tubes and reservoir is approximately 700 mL. This fluid has a density of $\rho = 1037 \pm 2$ kg/m^3, and a viscosity of $\mu = 4.1 \pm 0.1$ mPa·s [18]. Further, it behaves as a Newtonian fluid in the applied experimental conditions.

2.2 Computed Tomography Angiography

The dynamic heart phantom was scanned in a commercial CT scanner (Toshiba Aquilion ONE, Canon Medical Imaging Systems Inc., Japan) applying a CTA protocol while undergoing the exact displacement described in Section 2.1. The CTA was timed using the simulated ECG output, which is synchronised with the phantom movement as visualised in Fig. 3. The CTA output data consist of 20 volumes, i.e. 5% phase increments from peak to peak in the ECG. To ensure synchronisation between the CTA volumes and the CFD, each volume was compared to the corresponding geometry at these times in the CFD simulation. The voxel size in the reconstruction is $0.6\times0.6\times0.5$ mm^3. The heart cycle period was measured to be 0.76 s resulting in a volume-sample period of 0.038 s. The CTA procedure is the same as for an in vivo measurement with ECG electrodes connected to

the DHP ECG output channel, and intravenous contrast fluid was added to the fluid reservoir to obtain proper contrast between the fluid and the solid wall material similar to in vivo CTA.

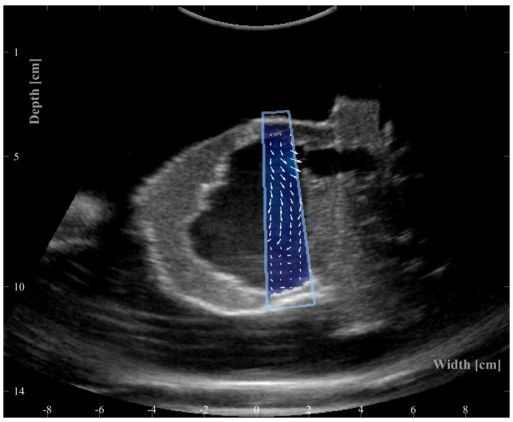

Fig. 4: Example of a full B-mode image with VFI in a sub-region. The arrows direction and length indicate flow direction and magnitude

2.3 Vector Flow Imaging

In-plane time dependent velocity fields were measured on the DHP with ultrasound VFI using a modified scanner for research (BK5000, BK Medical ApS, Herlev, Denmark) and a convex ultrasound probe (6C2,BK Medical ApS, Herlev, Denmark). The applied ultrasound sequence estimates the time dependent in-plane blood velocity vector field [15, 19] with a resolution of 0.75×1.5 mm given that the wavelength of the ultrasound wave is 0.375 mm. During VFI data acquisition the B-mode image is used to navigate the anatomy. The in-plane velocity magnitudes and directions are measured and visualised inside a sub-region that the operator draws on top of the B-mode image during acquisition as illustrated in Fig. 4. The narrow colour box is necessary to ensure sufficiently high sampling rate for the VFI data to capture the flow dynamics. The acquisition is time dependent, and can be saved as a video or as a raw data file. The probe was mounted on an in-house fixture on top of the DHP box, see Fig. 2, that enables full control of the probe position and tilt relative to the heart phantom. The fixture is used to scan eight parallel planes with an inter-plane distance of 5 mm as seen in Fig. 5b.

In each plane several acquisitions are made for a duration of six to eight seconds, corresponding to seven to ten cardiac cycles. Each VFI acquisition contains a full width B-mode image and VFI data inside a narrower sub-region of the B-mode image as seen in Fig. 4. The post-processed VFI data used for comparison contain data from 42 separate VFI acquisitions; 8 planes of 4-6 separate VFI acquisitions per plane, 210 cardiac cycles in total. The ultrasound equipment did not have ECG triggering to synchronise the cardiac phase of the measured cardiac cycles. Therefore, to ensure that all 42 VFI acquisitions are in phase, a time-delay was defined for each acquisition and added to the time stamps. The time-delays were estimated using a cross correlation of the B-mode images on a registration based displacement metric, i.e. by the movement of the phantom observed in the B-mode images.

2.4 Computational Fluid Dynamics

The simulation pipeline is based on the geometry prescribed CFD, which applies a known movement to the boundary of a fluid domain [11]. How the fluid moves inside the fluid domain is determined by the boundary conditions applied to the three boundaries seen in Fig. 5a, and defined as

$$\begin{aligned} \Omega_{inlet} &: \quad \vec{U}_{inlet}(t) \\ \Omega_{outlet} &: \quad 0 \quad \text{Pa} \\ \Omega_{wall} &: \quad \vec{U}_{mesh}(t) \quad , \end{aligned} \tag{2}$$

where the boundary condition at the inlet, Ω_{inlet}, is a time dependent plug flow prescribed by a mean velocity magnitude $|\vec{U}_{inlet}(t)|$. The velocity magnitude is estimated from the inlet cross-section area in the geometry representing the simulation model and demanding the same inlet volume flow rate $Q(t)$ as in the VFI measurement. $Q(t)$ is obtained from the VFI data by

$$Q(t) = |\vec{U}_{inlet}(t)| \cdot (\pi(D/2)^2) \quad , \tag{3}$$

where $|\vec{U}_{inlet}(t)|$ is acquired along the diameter D of the inlet assuming that the inlet is circular.

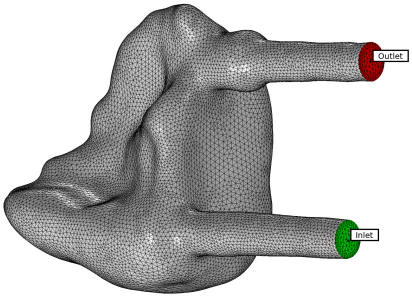

(a) RV cavity with labeled boundary types. **Gray:** Wall boundary domain Ω_{wall}. **Green:** Inlet boundary domain Ω_{inlet}. **Red:** Outlet boundary domain Ω_{outlet}

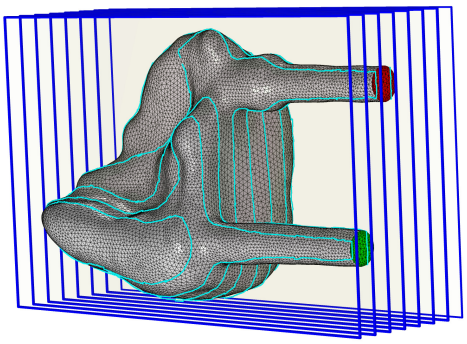

(b) VFI scan plane position relative to the CFD fluid domain. **Blue:** Edges of the 8 parallel VFI scan planes. **Cyan:** The intersection between VFI scan plane and CFD fluid domain boundary

Fig. 5: Visualisation of the segmented RV from CTA at the initial configuration, i.e. $t = 0$ s

This quantification of $Q(t)$ is necessary because the position of the inlet in the simulation model is different from the position of the VFI measurement. The inlet in the simulation model is defined upstream in the entrance tube, see Fig. 5a, compared to where the inlet velocity is measured with VFI. In the simulation, this is done to allow the flow profile to develop prior to entering the RV. Because none of the VFI scan planes line up with the inlet tube diameter, see Fig. 5b, velocity data were extracted from the plane, which covers the majority of the inlet diameter. Specifically, the velocity field along a line perpendicular to the flow at the transition between the inlet tube and the RV volume is extracted, and the spatial mean velocity is calculated for each time step throughout the flow cycle. Due to this offset of the imaging plane, this measured mean velocity is estimated to be 80% of the true mean velocity under the condition that the flow profile is parabolic. When compensating for the underestimation of the true spatial mean velocity the difference amounts to 0.386 m/s at $t = 0$ s. This is added to the applied inlet velocity waveform to obtain the same volumetric flow rate at the inlet in the CFD model as in the VFI measurement. The volume flow rate acquired from VFI is plotted in Fig. 6. The inlet velocity profile, $\vec{U}_{inlet}(t)$, is prescribed as a plug

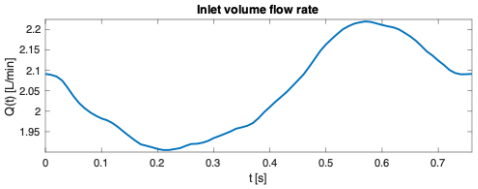

Fig. 6: The time dependent inlet volume flow rate $Q(t)$ applied to the inlet boundary as a plug flow. $Q(t)$ was obtained by a VFI measurement and an estimate of the cross sectional area at the VFI measurement

flow, but in reality the spatial velocity profile deviates from this to a more blunt parabolic-like profile at the RV entrance. This is obtained by allowing the profile to develop in the inlet pipe prior to entering the RV volume.

The boundary condition at the outlet, Ω_{outlet}, is a constant pressure of 0 Pa, which corresponds to the outlet tube going into a reservoir with a constant fluid column height. The boundary condition at the wall, Ω_{wall}, is the no-slip condition. In this model no-slip is defined as the fluid velocity being equal to the mesh movement velocity at the wall boundary. The CFD is solved numerically in COMSOL Multiphysics v5.6 (COMSOL AB Stockholm, Sweden) using

the finite element method and the ALE formulation. Here the Navier-Stokes equations for an in-compressible fluid,

$$\rho\left(\frac{\partial\vec{U}(\vec{r},t)}{\partial t}+(\vec{U}(\vec{r},t)\cdot\nabla)\vec{U}(\vec{r},t)\right) = -\nabla p+\mu\nabla^2\vec{U}(\vec{r},t) \quad (4)$$

$$\nabla\cdot\vec{U}(\vec{r},t)=0 \quad (5)$$

are solved numerically on a moving mesh assuming isothermal laminar flow. In (4) and (5) $\vec{U}(\vec{r},t)$ is the fluid velocity vector (m/s) which is depending on both time t (s) and space $\vec{r}$ (m). Here $\vec{r}=x\hat{e}_x+y\hat{e}_y+z\hat{e}_z$ is the position vector for a given point (x,y,z) in the fluid domain. Further, p is pressure (Pa), ρ is the fluid density (kg/m^3), and μ is the fluid viscosity (Pa·s). ∇ is the del operator, and ∇^2 is the Laplace operator. The effects of gravity are negligible, and gravity is therefore ignored. The fluid density and viscosity in the presented CFD model are assigned those of the blood mimicking fluid used in the experimental measurements with CTA and VFI (see Section 2.1).

2.4.1 Geometry

The fluid domain is defined as a surface mesh obtained from segmentation of the right ventricle (RV) in a single CTA volume (see Section 2.2) at the first time instance, which corresponds to minimum compression in the presented configuration. The segmentation is performed in MATLAB (Mathworks Inc., Natick, MA) and the final geometry is visualised in Fig. 5a. The full extend of the inlet and outlet tubes is kept as part of the segmentation to ensure smooth transition between the moving outer wall of the RV volume and the walls of the inlet and outlet pipes, which are not moving.

The ventricle movement is prescribed to the surface mesh via a displacement field, which is obtained by volumetric image registration. See Section 2.4.2.

2.4.2 Registration

The ventricle movement is estimated by volumetric image registration of the 20 CTA volumes. Several separate registrations are performed as illustrated in Fig. 1. These registrations are between the first volume and every other volume in the CTA sequence. At $t=0$ s the displacement is naturally zero. Furthermore, since the movement is cyclic, zero displacement is appended to the temporal displacement field, resulting in 21 time instances. The resulting displacement field contains a displacement vector component in each direction (x,y,z) in each voxel at each time step. The resulting displacement field is represented by the displacement field $\vec{d}(x,y,z,t)$

$$\vec{d}(x,y,z,t)=\begin{bmatrix}d_x(x,y,z,t)\\ d_y(x,y,z,t)\\ d_z(x,y,z,t)\end{bmatrix} \quad (6)$$

The registration uses the MATLAB function `imregdemons`, which is based on the Diffeomorphic Demons algorithm [20, 21]. Finally the displacement is smoothed temporally, interpolated in MATLAB and sent to the COMSOL model solver during the mesh movement computations.

2.4.3 CFD Steps in COMSOL

The numerical computation can be split into two independent steps to decrease complexity; The mesh movement (pure Lagrangian), and the CFD (ALE on the moving mesh nodes from the mesh movement step). This split allows the movement to be calculated separately, saving computation time by allowing larger time steps, and avoiding re-calculating the mesh positions for every cycle by reusing the cyclic mesh movement solution for each cardiac cycle.

Mesh Movement

The mesh movement is obtained by applying the discrete displacement field, $\vec{d}(x,y,z,t)$, on the surface mesh of the fluid domain. First, the displacement field is interpolated and smoothed temporally. The temporal smoothing is penalised to ensure equal rates of volume change at the beginning and end of the cardiac cycle. The displacement is applied directly to the fluid domain surface. The movement of the volume inside the

fluid domain is determined by a hyper-elastic spatial smoothing. The output of this study step is a moving mesh of one cardiac cycle, where every boundary node has the exact same position in the beginning, and in the end of the cardiac cycle. The mesh positions are calculated at fixed time steps of 0.019 s. The mesh movement solution is stored and used as input for the CFD solver, which interpolates the solution for each time step taken by the CFD solver.

Ensuring Well-posed Initial Conditions

A stationary solution is calculated and used as initial condition to avoid solving an ill-posed model. A series of stationary solutions are calculated at $t = 0$ s on the initial reference geometry with zero displacement with increasing inlet velocity from 0 m/s to the inlet velocity at $t = 0$ s. Each stationary solution uses the previous solution as an initial guess. The final stationary solution is used as the initial condition for the first cycle of the dynamic solution.

Table 1: Time dependent solution: key numbers and resources

Total elements	384,054
Degrees of freedom	391,324 (plus 384,055 internal DOFs)
Computation time	16h 38m 33s
Resources	2x Intel Xeon CPU E5-2660 v3 2 sockets, 20 cores, 2.60 GHz Available memory: 128.65 GB (utilized memory): 33.94 GB

Mesh independence study

A mesh independence study was performed to check the quality of the mesh and the numerical accuracy of the simulation results. Four different meshes were tested on the model geometry and the metric on which the meshes were evaluated is the volume and cycle average of the velocity magnitude. The result is shown i Fig. 7. The mesh independence study indicate that the solution is precise within 0.5% when the number of degrees of freedom is larger than $8.8 \cdot 10^5$. For this study the settings in Mesh 4 were used.

Please note that the degrees of freedom listed in Tab. 1 is calculated differently compared to the degrees of freedom listed in Fig. 7, which is based on all compiled equations in the simulation.

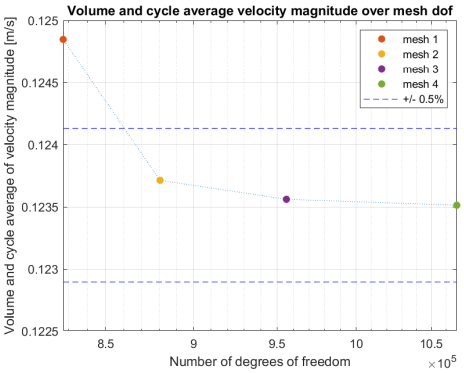

Fig. 7: Mesh independence study. The mesh size is provided in degrees of freedom on the x-axis. The meshes are colour coded and the dashed horizontal lines mark a difference of 0.5% compared to the mesh with the highest number of degrees of freedom.

Time Dependent CFD

The mesh movement solution calculated in the first step is applied to all mesh nodes using the ALE formulation. The boundary conditions are defined in (2). The simulation is run for six cycles to ensure cycle convergence, and thereby independence from initial conditions. The convergence is evaluated by calculating the difference in velocity magnitude at evenly distributed volumes in the fluid domain at the last time step of each cycle, such that

$$Vel_{\text{diff}} = |\vec{U}_i| - |\vec{U}_{i+1}| \tag{7}$$

where Vel_{diff} is the quantified difference in velocity magnitude in a volume, and i is the flow cycle index running from one through five. The result of the convergence is given in Fig. 8. It is seen that the absolute difference in velocity magnitude is reduced consecutively as more cycles are run. The difference in absolute velocity magnitude when comparing cycle 1 to cycle 2 is 0.133 m/s, whereas when looking at this difference between cycle 5 and 6, it is reduced to 0.038 m/s. The CFD simulations were run on a computer with Intel Xeon CPUs with details on resources provided in Table 1. The computation time was approximately 17 hours.

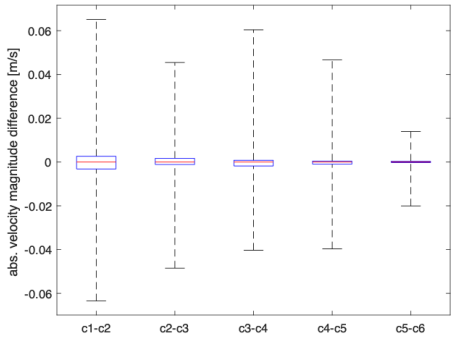

Fig. 8: Cycle convergence evaluation. Each box plot visualises difference in velocity magnitude between consecutive cycles measured in 97,831 points

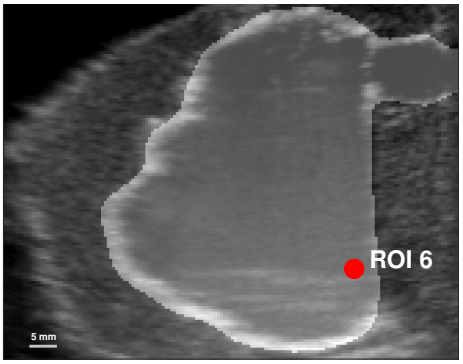

Fig. 9: Illustration of the fluid domain layered on top of the B-mode image. In this plane ROI #6 is seen at the base of the heart phantom.

2.5 Post Processing

The CFD simulation solution contains a time dependent 3D flow velocity field and pressure field, as well as domain (geometry) information. The VFI is limited to eight parallel planes containing time dependent in-plane 2D flow velocities, and the corresponding time dependent B-mode images as the geometry information. For direct comparison the two data sets are interpolated onto the same spatial-temporal grid consisting of eight planes with a pixel size of 0.5×0.5 mm^2, and a temporal sample period of 0.01 s. The information available for each pixel at each time point in each plane is therefore: u, v, w, and g, where u, v, and w are the velocity vector components along each direction in the global coordinate system, such that

$$\vec{U}(x,y,z,t) = \begin{bmatrix} u(x,y,z,t) \\ v(x,y,z,t) \\ w(x,y,z,t) \end{bmatrix} \begin{matrix} x-\text{comp.} \\ y-\text{comp.} \\ z-\text{comp.} \end{matrix} \quad (8)$$

and g is geometry, i.e. B-mode for the ultrasound and domain index for the CFD. The geometry is used for co-registration of the two data sets by aligning landmarks using a rigid transformation. In Fig. 9 the CFD fluid domain is visible as a transparent grey overlay on top of the B-mode image.

Note that the CFD data contains more information than the VFI data, because the VFI does not have any pressure information and only measures in-plane 2D velocities. The v component is, in this situation, the out-of-plane velocity vector component of the VFI and therefore not included in the analysis. Hence, the comparisons are only made from in-plane velocities, and the v component of the CFD is not included either in the comparisons made here. The magnitude of the out-of-plane component from the CFD data is provided in the results to illustrate the importance of having the full velocity information when analysing complex flow as in the heart.

2.6 Method and metrics for comparison

The qualitative comparison is a description of flow trends in corresponding VFI slices and CFD slices. Thus, it is based on visual assessment of flow direction and magnitude at two specific time points during the flow cycle. The first time instant is at 0.34 s corresponding to 45% into the flow cycle. The second time instant is at 0.74 s, which corresponds to 97% of the total flow cycle. The metric for quantitative comparison is the velocity magnitude,

$$|\vec{U}| = \sqrt{u^2 + w^2} \quad (9)$$

where u and w are the components of the velocity vector $\vec{U}$ as defined in (8) and $\vec{U}$ is evaluated at all time points in 16 regions of interest (ROI) distributed over the eight planes. The location of the 16 ROIs was selected manually with

the aim to represent physiologically meaningful landmarks such as the inlet jet, the apex and the outlet tract. For the results presented here four specific ROIs where selected among the 16 because they represent some common findings. They are; at the inlet jet, close to the outlet tract, at the apex close to the moving wall, and in the almost cone shaped part of the RV close to the moving wall. The position of all 16 ROIs can be found in Online Resource 2. Note that the ROIs are stationary in space through out the flow cycle even though the fluid domain is moving. The velocity magnitude data for all ROIs are grouped in eleven non-overlapping time bins and averaged within each ROI. In both qualitative and quantitative comparisons, the VFI data are an average over five cycles. The CFD data are obtained from the last flow cycle in the simulation.

3 Results

The result section is divided into a qualitative comparison of the simulated and measured velocity field in representative 2D planes, followed by a quantitative comparison of the flow in representative ROI's through out the cardiac cycle.

3.1 Velocity field comparison

In Fig. 10 the in-plane velocities for CFD and VFI at $t = 0.34$ s in two slices are shown, and in Fig. 11 the same shown is show at $t = 0.74$ s. These two slices and time instances are chosen because they showcase both good as well as poor correspondence in the velocity fields. The dynamics for all CFD slices and all VFI slices are available as additional data (Online Resource 1) visualising the measured and simulated flow for the complete flow cycle defined in this study. The colour bar indicates the velocity magnitude, and the arrows show the flow direction in each slice. Each image is also labelled with three anatomical landmarks on the phantom; the inlet, the outlet and the apex. In Fig. 10i and 10iii the velocity vectors in both the CFD and VFI data show a general clockwise flow trend, especially to the left indicated by the label A, and low velocity (<0.05 m/s) in the central region at label B.

The flow in the lower part at label C is down towards the right corner for both CFD and VFI. Additionally, a clockwise vortex to the right of label C is seen in both cases. In the domain centre, at label B, a vortex is observed together with very low velocities (<0.05 m/s) in the VFI data. In the simulated flow there is also rotation at label B, but it is not as pronounced as in the measured data when looking at the arrow directions and magnitudes.

At the end of the flow cycle at $t = 0.74$ s, visualised in Fig. 10ii and 10iv, both CFD and VFI have a clockwise rotational flow, with a dominant north-east flow direction in both at label D. In the bottom of the fluid domain, at label E, the direction is downwards and flow separation is seen, especially in the VFI data. At label F, opposite flow directions in CFD and VFI are observed, however, at the boundary to the right of label F, the flow is in the same direction for both techniques. There is a clockwise vortex in the simulated flow just above label F, and a similar vortex is seen in the VFI at label E in Fig. 10iv.

In Fig. 11i and 11iii the highest velocity of 0.4 m/s in both cases is through the outlet at label G. In both CFD and VFI there is an upwards directional flow at label H, and a downwards directional flow at label I, creating a clockwise vortex between label I and label H. A second clockwise vortex is seen at label J for both cases. In both CFD and VFI there is a flow separation between fluid going through the outlet towards the right, and going downwards below the outlet. In the bottom and top of the domain, both labelled K, there is a downward trend of the flow in the CFD, but the opposite is seen in the VFI.

Lastly, in Fig. 11ii and 11iv, the flow trend towards south in the centre above and below label L, additionally an upwards flow trend is seen at label M at the apex. Note here, that the apex is not moving at this time instant. In both CFD and VFI the highest velocity is at label N in the centre of the outlet (>0.35 m/s) and the flow direction is downwards at the boundary to the right, labelled O, which corresponds to the base of the heart phantom. Besides high velocity at the outlet, the velocity is also high at the apex of the heart phantom at label M in both cases. Further, there is a vortex at label P in both situations, however, the vortex is clockwise in the simulated flow and counterclockwise in the measured flow. A clockwise vortex is seen in the CFD data between label M and label P, where the same clockwise vortex in

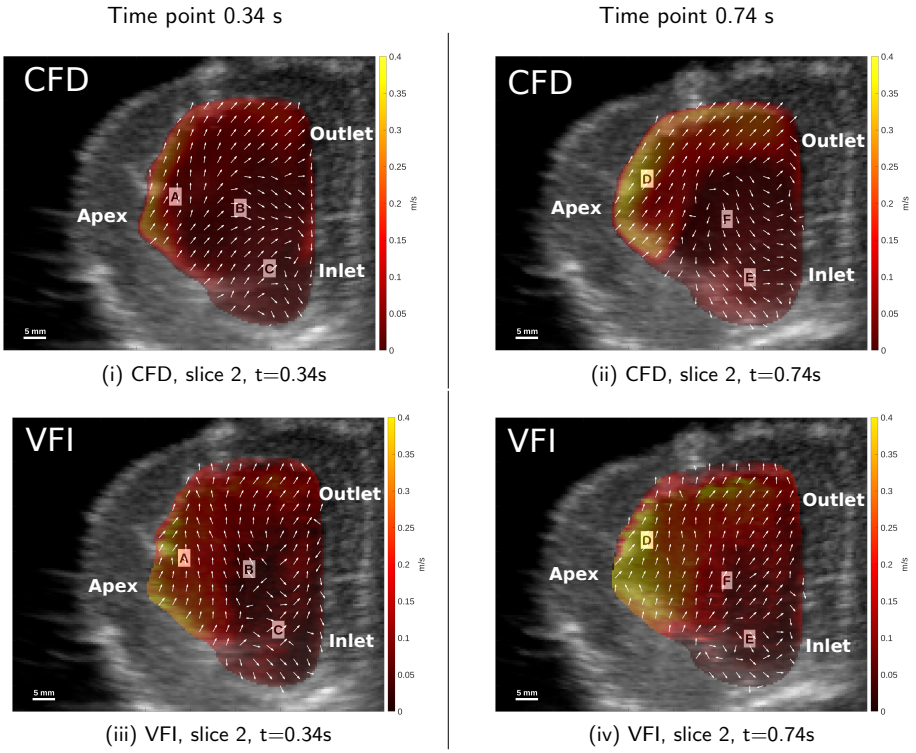

Fig. 10: Comparative visualisations of in-plane velocities in slice 2 at the time-points t = 0.34 s (left column) and t = 0.74 s (right column). All visualisations are on top of a B-mode image at the corresponding time-point. The colour represents in-plane velocity magnitude inside the fluid domain, the arrows are normalised in-plane velocity directions. **(i,ii):** CFD in-plane velocities. **(iii,iv):** VFI in-plane velocities.

VFI is located between label M and label L, and is not as pronounced as in the simulated flow.

Regarding the velocity magnitude, in general, the VFI data show slightly higher velocity when comparing the distribution of the dynamic range of the colour bar. For example, in Fig. 10i and 10iii this is seen at the apex near label A. To obtain a more specific assessment of the velocity magnitude, it is obtained in four ROIs (see Sec. 3.2).

Overall the qualitative assessment of the intracardiac flow patterns in measurement and simulation shows similar trends in most cases, when comparing CFD to VFI.

3.2 Quantitative assessment of the flow

The quantitative comparison consists of a description of four representative ROIs displayed in Fig. 12 and a linear regression over all sixteen ROIs at time points over the entire cardiac cycle, see Fig. 13.

In Fig. 12a ROI A (ROI #5, slice 2) is close to the outlet of the right ventricle. The outlet is not visible in the CFD domain on the slice shown in Fig. 12a, but can be seen vaguely in the B-mode image behind ROI A. Both the CFD and VFI follow the same trend in velocity magnitude; a u-shaped curve with the lowest point just after 0.4 s. The magnitude for the CFD peaks at 0.18 m/s and has a minimum of 0.06 m/s. For the VFI the maximum is 0.24 m/s and the minimum is 0.11 m/s. In ROI A the CFD is consistently lower than the VFI and deviating slightly more than one standard deviation of the VFI.

ROI B (ROI #7, slice 3) is placed close to the moving boundary at the apex of the heart phantom where a large clockwise flow trend is observed

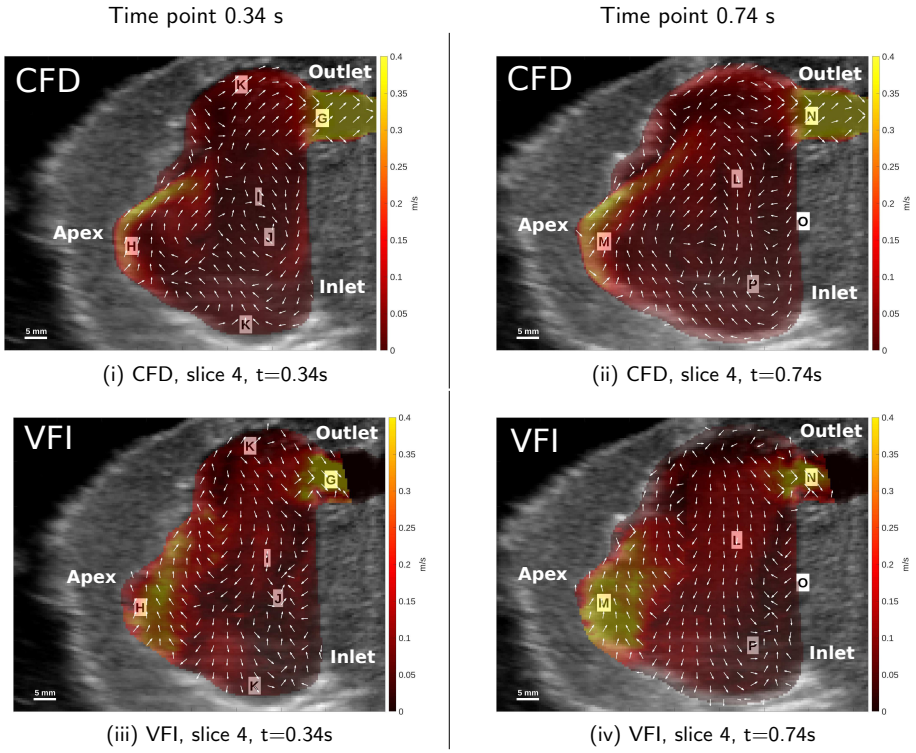

(i) CFD, slice 4, t=0.34s

(ii) CFD, slice 4, t=0.74s

(iii) VFI, slice 4, t=0.34s

(iv) VFI, slice 4, t=0.74s

Fig. 11: Comparative visualisations of in-plane velocities in slice 4 at the time-points $t = 0.34$ s (left column) and $t = 0.74$ s (right column). All visualisations are on top of a B-mode image at the corresponding time-point. The colour represents in-plane velocity magnitude inside the fluid domain, the arrows are normalised in-plane velocity directions. **(i,ii):** CFD in-plane velocities. **(iii,iv):** VFI in-plane velocities.

in both CFD and VFI in Fig. 11i, 11ii, 11iii and 11iv. Since this ROI is close to a moving boundary, the trend in velocity magnitude in ROI B is expected to be dominated by the changing proximity to the boundary. In the most extreme case, the moving boundary could cross the ROI position and report zero velocity during that period of time, however, this is not the case here. The velocity magnitude in the VFI is a reversed u-shaped curve with the peak around 0.3 s. The CFD is generally underestimating the VFI more in ROI B compared to ROI A, but it has a large local acceleration between 0.1 s and 0.2 s. The larger local acceleration in ROI B in the CFD could be explained by the larger spatial velocity gradient seen in the CFD data in Fig. 11i and 11ii due to fluid being pushed into the ROI by the wall movement. The magnitude for the CFD predicted flow peaks at 0.33 m/s, and has a minimum of 0.10 m/s. For the flow obtained with VFI the maximum velocity is 0.31 m/s and the minimum velocity is 0.22 m/s.

ROI C (ROI #13, slice 5) is located close to the inlet jet, see Fig. 12e. The velocity magnitude trend is therefore expected to follow the trend of the volume flow rate, $Q(t)$, applied to the system, which is shaped like a negative sine wave (see Fig. 6). There is a good correspondence between CFD and VFI in Fig. 12f since the velocity magnitude from the CFD simulation falls within one standard deviation of the VFI data. This is expected when data are extracted this close to the inlet because the inlet conditions for the flow simulation are based on the VFI measurement in close proximity to this location. The velocity magnitude for the CFD peaks at 0.38 m/s and has a minimum of 0.25 m/s. For the VFI the maximum is 0.40 m/s and the minimum is 0.26 m/s.

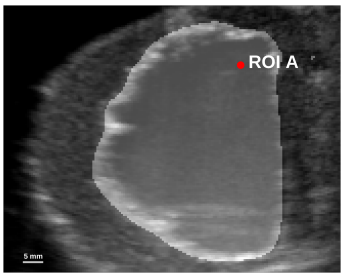

(a) Slice 2

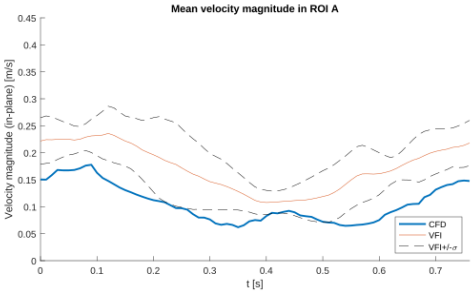

(b)

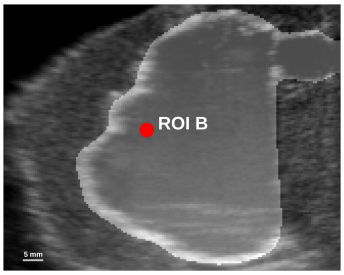

(c) Slice 3

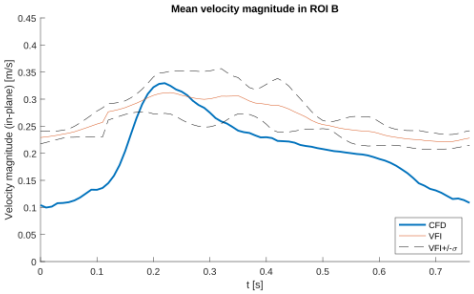

(d)

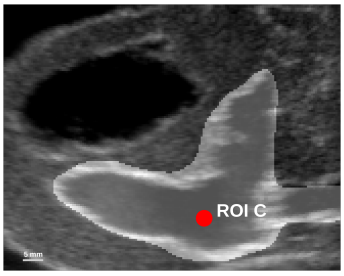

(e) Slice 5

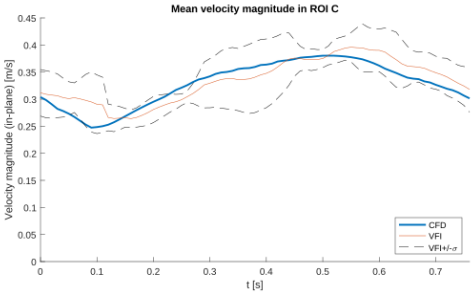

(f)

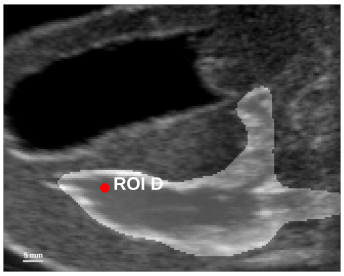

(g) Slice 7

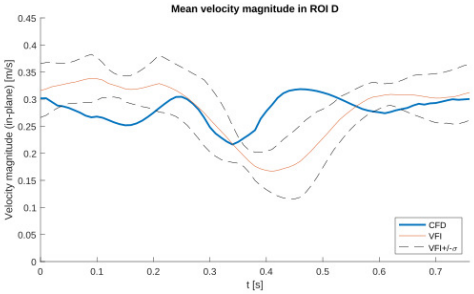

(h)

Fig. 12: ROI placement and temporal velocity magnitude data for ROIs: A, B, C and D. **Left (a, c, e, g):** B-mode images with CFD fluid domain overlay, all taken at $t = 0$ s. The red dot represents the location of the ROI. **Right (b, d, f, h):** The mean velocity magnitude over time inside each ROI for the CFD simulation and VFI measurement. The VFI flow profiles are averaged over 5 flow cycles. Systolic phase (compression) is from 0 s to 0.4 s, diastolic phase is from 0.4 s to 0.76 s.

The last ROI, ROI D (ROI #15, slice 7), is placed in an almost cone-shaped part of the ventricle and close to the moving boundary, see Fig. 12g. The velocity magnitude trend is similar in both CFD and VFI. It starts and stops at 0.3 m/s over the flow cycle, where the largest deviation is a valley that occurs at $t = 0.35$ s in the CFD, and at $t = 0.42$ s in the VFI. The time shift of this valley can be explained by a small moving vortex that reaches and moves past ROI D in the CFD data set slightly before the same phenomena is observed in the VFI (See Online Resource 1 and 2, slice 7). The velocity magnitude of the CFD peaks at 0.32 m/s and has a minimum of 0.22 m/s. For the VFI the maximum is 0.34 m/s and the minimum is 0.17 m/s. The CFD velocity profile is within one standard deviation of the velocity profile obtained with VFI through the majority of the flow cycle, except in the interval from 0.4 s to 0.5 s.

3.2.1 Evaluation of the out-of-plane component

The CFD data provides velocity information in all three spatial dimensions, so to complete the evaluation of the full velocity field, the quantitative data for all three velocity components in the ROIs presented in Fig. 12 are presented here. Table 2 lists the average values for each velocity vector component in each of the four ROIs. The evolution in time of the three velocity components in each ROI is shown in Online Resource 3.

Table 2: Average velocity magnitudes for all three velocity vector components within ROIs. Here $\langle u \rangle$, $\langle v \rangle$ and $\langle w \rangle$ are the average over one full flow cycle.

	$\langle u \rangle$ [m/s]	$\langle v \rangle$ [m/s]	$\langle w \rangle$ [m/s]
ROI A	0.097	0.064	-0.043
ROI B	0.119	-0.095	-0.159
ROI C	-0.327	0.026	0.019
ROI D	-0.196	-0.084	-0.192

In ROI C, which is closest to the inlet, the out-of-plane component $\langle v \rangle$ has a magnitude corresponding to 7.95% of the dominating in-plane velocity component $\langle u \rangle$. For ROIs A and B the out-of-plane component is 66.0% and 59.8% of the dominating in-plane velocity component respectively. Lastly, in ROI D which is closest to the apex of the heart phantom, $\langle v \rangle$ is 43.9% of the dominating in-plane velocity component.

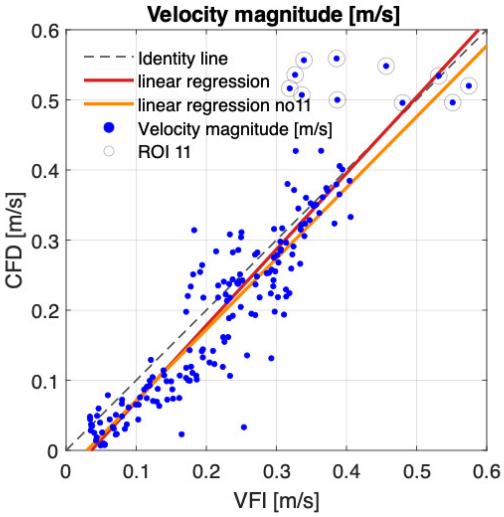

Fig. 13: Comparison of velocity magnitude in 11 time bins at all 16 ROIs. *Red line:* Linear regression on all data points (R^2 = 0.809, intercept = -0.039 m/s, slope = 1.09, SD = 0.060 m/s). *Orange line:* Linear regression excluding data from ROI #11 (R^2 = 0.823, intercept = -0.030 m/s, slope = 1.01, SD = 0.048 m/s). The data from ROI #11 have been circled

3.3 Global evaluation

To complete the comparison and evaluate the performance of the proposed pipeline, a global evaluation is made based on all 16 ROIs. The time dependent spatial mean velocity magnitude within each ROI is divided into 11 non-overlapping time bins. The temporal means of the resulting 176 time bins are compared between CFD and VFI in a scatter plot with a fitted linear regression line. The scatters in Fig. 13 are the 176 CFD time bins plotted against the 176 VFI time bins.

A group of 11 blue scatters in Fig. 13, all belonging to ROI #11, are marked with a circle to indicate that they are considered as outliers. The large deviations in ROI #11 are thought to be an effect of the inlet corrections described in Section 2.4 since this ROI is positioned in the transition between the inlet pipe which has a rigid wall and the RV volume that has a moving wall boundary.

An evaluation including all ROIs is made as well as an evaluation excluding ROI #11. The evaluation consists of a linear regression fitted to the scatters in Fig. 13 and a calculation of the standard deviation. The resulting regression numbers are presented in Table 3. From this, as expected, excluding the suspected outliers from ROI #11 the R^2 improves from 0.809 to 0.823. This is also reflected in the slope of the regression line, which improves from 1.09 to 1.01, as well as in the SD on the velocity magnitude. Here the SD is reduced from 0.06 m/s to 0.048 m/s. In both regressions the slope is close to 1 with intercept below zero at -0.039 m/s and -0.030 m/s respectively. This indicates that the output of the CFD pipeline consistently underestimates the velocity magnitude compared to VFI, and that the level of underestimation is independent of the measured velocity magnitude.

Table 3: Regression numbers

	R^2	Intercept [m/s]	Slope	SD [m/s]
All ROI's	0.809	-0.039	1.09	0.060
Excluding ROI #11	0.823	-0.030	1.01	0.048

4 Discussion

The results presented in this paper show a CFD pipeline applied for the first time on a dynamic heart phantom and compared to a highly controlled ultrasound VFI measurement of the same phantom under the same conditions. This work flow facilitates validation of cardiac flow properties based on directly obtained flow-based metrics. The CFD pipeline is based on the movement of the phantom ventricle, which is gathered from CTA and volumetric image registration. The inlet was a prescribed time dependent velocity calculated to provide the same volume flow rate as in the VFI measurements. A qualitative comparison, based on in-plane velocity direction and magnitude, showed overall correspondence when looking at the locations close to the inlet and outlet. When comparing the results in positions further away from the inlet towards the apex the similarity was less. The same tendency was observed for the quantitative results. A quantitative comparison, based on 11 non-overlapping time bins in all 16 ROIs showed the CFD estimates to be consistent, however with a negative bias and a SD of 10% at the highest measured values. Although the standard deviation of the CFD estimates seems large, the comparison is based on a pipeline where the registration approach has not yet been optimised. An important optimisation to the registration is to consider the temporal dimension in the registration instead of treating each registration as independent. Looking at the quantitative results in Fig. 12, the hypothesis of this paper has not be met for all 16 ROIs. However, by performing optimisation of the registration and formulation of the fluid boundary conditions the hypothesis can potentially be accepted.

The bulk blood flow fluid dynamics inside the RV presented here is solved using geometry-prescribed CFD, where the numerical technique is based on the ALE formulation. Others have modelled the fluid dynamics in the heart using single particle hydrodynamics (SPH) [22, 23]. The SPH is a mesh-free finite element method, which handles the solution of the fluid and solid mechanics in one algorithm as it is a purely Lagrangian formulation. This is advantageous when valves are part of the model geometry [24]. The numerical computation here is a two step procedure where the mesh movement is handled according to a Lagrangian description, and the CFD is handled in an ALE formulation of the Navier-Stokes equations, which is a mesh-based method. This is done to lower the computational complexity and reduce the computation time. The use of the ALE method is not straight forward in the case where heart valves are included in the model geometry due to the intricate fluid-structure interaction governed by the rapid movement and slender structure of the valves.

The pipeline is designed to be applied in vivo, however validating on a phantom provides a higher quality comparison compared to in vivo validation. The presented phantom setup is therefore a crucial tool for developing the CFD pipeline further. The phantom is easier to measure with ultrasound, because there are no anatomical restrictions, and the ultrasound transducer can be mounted in a fixture, adding spatial information and consistency to the measurements. The phantom measurements are in parallel planes with 5 mm between them, which would be very hard,

if not impossible, to obtain in vivo, because the transducer must be placed in contact with the skin, and either between or under the ribs.

Since the CFD pipeline estimates three dimensional flow velocities, the presented validation only compares two of the three dimensions. Neglecting the out-of-plane component in the analysis can be valid in flow of low complexity. However, the flow in the heart has a high complexity. In this study, the out-of-plane component at the inlet was 7.95% of the dominating in-plane component magnitude. This is because the fluid has not yet entered the RV and thus flow in a laminar configuration with a slightly blunt parabolic profile. But the further the fluid advances inside the RV away from the inlet, the out-of-plane component becomes more dominant, especially during the stretching from fully compressed to the initial position of the phantom (see Online Resource 3). The fixture shown in Fig. 2 is capable of measuring planes orthogonal to the presented data set, and can thereby obtain velocity data for the out-of-plane velocity component. But this is not a trivial measurement to perform. For the ultrasound probe used here, the sample volume for a velocity estimate is at best $1 \times 3 \times 0.5$ mm^3 and up to 10 mm in the y-direction due to the probe's acoustic lens. While it would be technically possible to measure the out-of-plane component by rotating the probe 90 degrees and thereby form a full 3D velocity vector, this anisotropic sample volume would make the combination of the x and z components from one measurement with the y component from a second measurement highly uncertain at best. An alternative could be to acquire the ultrasound data in 3D to get the full velocity field. Currently, there are techniques to do 3D ultrasound flow estimation [25, 26], with only a few examples of imaging and quantification of complex flow [27]. These techniques still lacks detailed performance evaluation before they are applicable as ground truth for validation of flow simulation pipelines like the one presented here.

The setup here even allows changing parameters, such as heart rate, stroke volume, beat-to-beat variations, etc., to create best-case and worst-case scenarios for targeted troubleshooting during development of the pipeline before moving to in vivo validation. Most importantly, the prescribed phantom movement and flow patterns are repeatable. This allows for repeated measurements with minimal inter-measurement variation, which is why averaging over 210 cardiac cycles is acceptable in the phantom measurements, even though it is listed as a disadvantage for in vivo methods.

The purpose of this work is to present a novel CFD pipeline and validation setup for development of cardiac flow simulation models. The metrics for evaluating accuracy in this paper are therefore designed to compare the CFD flow patterns to the VFI measurements as transparently as possible. Other publications have largely been comparing metrics already used in the clinic such as stroke volume, peak flow rate, kinetic energy at peak systole, etc. [14]. While these metrics are directly translatable and valuable in clinic, they are either directly derivable or closely related to geometry changes instead of the flow patterns themselves. These metrics are often an integration over a large volume or a wide time span. The work presented in this paper is a smaller, more scrutinised, step in the intra-cardiac CFD pipeline development, focusing directly on the flow patterns. Metrics derived from CFD simulation models can only truly be trusted, if it is certain that they are derived directly from the actual blood flow patterns. When this is achieved, CFD simulations can be a valuable addition to existing clinical methods, adding new important flow based metrics to the diagnosis of cardiac diseases, as well as providing a more detailed post-operative evaluation as part of the treatment follow-up.

4.1 Limitations

An important limitation to all phantom validation is that it only reflects the performance of the method when applied to the phantom. The inlet flow was applied using a simple commercially available impeller pump allowing for application of constant flow only and less exact control of the delivered flow rate. The events of systole and diastole were governed by the cyclic motion of the phantom applied through the actuator rod, where the compression represents the systolic phase, and the diastolic phase is when the the phantom returns to its starting position. In combination with the fact that the phantom is designed without valves, this resulted in that the pump was significantly affected by the changes in after-load caused by the compression of the phantom. The inlet

conditions were therefore extracted from the ultrasound VFI measurements to obtain the correct volume flow rate. The applied volume flow rate is low compared to the physiological flow rate [28]. The nominal flow rate of the pump is 5 L/min, corresponding to the average cardiac output in an adult. But this flow rate was significantly reduced because the afterload on the pump outmatched what the pump was designed for. Misalignment of the imaging plane used for estimation of the spatial mean velocity caused an underestimation of 80 % of the true velocity, which corresponds to that the imaging plane is at 89.4 % of the true vessel diameter. This, however, will only have a little impact on the estimated volume flow rate. It has been shown that a 10 % off-axis error for the imaging plane results in approximately a 5% underestimation of the volume flow rate [29]. This causes the inlet conditions to be a function of the VFI measurement as well as the segmentation of the inlet geometry, which reduces the control of the phantom. Thus, the pipeline is not validated against a completely independent measurement. Future validation measurements should use a calibrated gear-head pump, which is less sensitive to changes in after-load and can control the volume flow rate to match in vivo cases. This will simplify the inlet boundary condition in the CFD model, and increase the control of the heart phantom.

The standard deviation of the velocity magnitude, excluding ROI #11, is 0.048 m/s. Relative to the highest measured velocity this SD is around 10% which is excellent for such complicated flow as investigated here. Additionally, considering that the wall movement in the presented CFD pipeline is based on an non-optimised registration approach, the flow simulation pipeline has the potential to obtain an even higher precision through optimisation of the registration approach.

Evaluating quantitative results like in Fig. 13 and Table 3 from a controlled phantom setup is going to be an essential validation tool during future pipeline development. The general underestimation in velocity magnitude, represented by the intercept and slope of the regression, could be a consequence of the inlet estimation. The registration approach in this work was performed in the simplest way possible that still provided acceptable results. Considering the presented method is founded on a geometry prescribed CFD simulation of the flow behaviour, the wall movement is the most important input to the model for accurate results. The presented approach performs 19 independent registrations, between first volume and all other volumes, however the registrations are not truly independent, and the temporal information should be included in the registration [30].

5 Conclusion

A complete pipeline for geometry prescribed CFD simulation of intra-cardiac blood flow patterns has been applied on a dynamic heart phantom for validation purposes. The qualitative comparison with ultrasound VFI data shows overall similarities in flow direction and location of vortexes. The quantitative data showed similarity in time progression of velocity magnitude in 16 different ROIs with a general tendency of underestimation: $R^2 = 0.823$, intercept = -0.030m/s, slope = 1.01, and SD = 0.048m/s. This direct comparison of flow properties and patterns shows that the flow simulation pipeline applied here produce accurate flow patterns in regions close the inlet and outlet, since the velocity magnitude is within one SD of the reference VFI data. But it also shows that in regions far away from the well-controlled boundary conditions the pipeline fails to produce accurate results. By optimising the registration method and apply well-controlled volume flow in the experimental setup, the output of the pipeline can become more reliable and applied to in vivo cases.

Acknowledgement

The authors would like to thank Klaus F. Kofoed (MD, PhD, DmSc Department of Cardiology, Rigshospitalet, University of Copenhagen) for making the CTA data acquisition possible.

Conflict of interest

Rasmus Hvid, Matthias Bo Stuart, Jørgen Arendt Jensen and Marie Sand Traberg declares that they have no conflict of interest. This study has received funding from Innovation Fund Denmark (Grant no. 29035695).

References

[1] Bellhouse B, Bellhouse F. Fluid mechanics of the mitral valve. Nature. 1969;224(5219):615–616. https://doi.org/10.1038/224615a0.

[2] Peskin C. Numerical analysis of blood flow in the heart. J Comput Phys. 1977;25(3):220–252. https://doi.org/10.1016/0021-9991(77)90100-0.

[3] Garcia D, del Alamo JC, Tanne D, Yotti R, Cortina C, Bertrand E, et al. Two-dimensional intraventricular flow mapping by digital processing conventional color-Doppler echocardiography images. IEEE Trans Med Imaging. 2010;29(10):1701–1713. https://doi.org/10.1109/TMI.2010.2049656.

[4] Hong GR, Pedrizzetti G, Tonti G, Li P, Wei Z, Kim JK, et al. Characterization and quantification of vortex flow in the human left ventricle by contrast echocardiography using vector particle image velocimetry. JACC: Cardiovascular Imaging. 2008;1(6):705–717. https://doi.org/10.1016/j.jcmg.2008.06.008.

[5] Hansen KL, Møller-Sørensen H, Kjaergaard J, Jensen MB, Jensen JA, Nielsen MB. Aortic Valve Stenosis Increases Helical Flow and Flow Complexity: A Study of Intra-operative Cardiac Vector Flow Imaging. Ultrasound Med Biol. 2017;43(8):1607–1617. https://doi.org/10.1016/j.ultrasmedbio.2017.03.018.

[6] Fadnes S, Nyrnes SA, Torp H, Lovstakken L. Shunt Flow Evaluation in Congenital Heart Disease Based on Two-Dimensional Speckle Tracking. Ultrasound Med Biol. 2014;40(10):2379–2391. https://doi.org/10.1016/j.ultrasmedbio.2014.03.029.

[7] Sengupta PP, Pedrizzetti G, Kilner PJ, Kheradvar A, Ebbers T, Tonti G, et al. Emerging trends in CV flow visualization. JACC: Cardiovascular Imaging. 2012;5(3):305–316. https://doi.org/10.1016/j.jcmg.2012.01.003.

[8] Munoz D, Markl M, Mur J, Barker A, Fernandez-Golfin C, Lancellotti P, et al. Intracardiac flow visualization: Current status and future directions. Eur Heart J Cardiovasc Imaging. 2013;14(11):1029–1038. https://doi.org/10.1093/ehjci/jet086.

[9] Eriksson J, Bolger A, Ebbers T, Carlhäll C. Four-dimensional blood flow-specific markers of LV dysfunction in dilated cardiomyopathy. Eur Heart J Cardiovasc Imaging. 2013;14(5):417–424. https://doi.org/10.1093/ehjci/jes159.

[10] Stocker TJ, Deseive S, Leipsic J, Hadamitzky M, Chen MY, Rubinshtein R, et al. Reduction in radiation exposure in cardiovascular computed tomography imaging: results from the prospective multi-center registry on radiation dose estimates of cardiac CT angiography in daily practice in 2017 (PROTECTION VI). Eur Heart J. 2018;39:3715–3723. https://doi.org/10.1093/eurheartj/ehy546.

[11] Doost S, Ghista D, Su B, Zhong L, Morsi Y. Heart blood flow simulation: A perspective review. Biomed Eng Online. 2016;15(1):1–28. https://doi.org/10.1186/s12938-016-0224-8.

[12] Stoll VM, Loudon M, Eriksson J, Bissell MM, Dyverfeldt P, Ebbers T, et al. Test-retest variability of left ventricular 4D flow cardiovascular magnetic resonance measurements in healthy subjects. J Cardiovasc Magn Reson. 2018;20(15). https://doi.org/10.1186/s12968-018-0432-4.

[13] Lantz J, Henriksson L, Persson A, Karlsson M, Ebbers T. Patient-Specific Simulation of Cardiac Blood Flow From High-Resolution Computed Tomography. J Biomed Eng. 2016;138:121004–1–121004–9. https://doi.org/10.1115/1.4034652.

[14] Lantz J, Gupta V, Henriksson L, Karlsson M, Persson A, Carlhall C, et al. Intracardiac flow at 4D CT: Comparison with 4D flow MRI. Radiology. 2018;289:51–58. https://doi.org/10.1148/radiol.2018173017.

[15] Jensen JA, Munk P. A New Method for Estimation of Velocity Vectors. IEEE Trans Ultrason Ferroelec Freq Contr. 1998;45(3):837–851. https:

//doi.org/10.1109/58.677749.

[16] Olesen JB, Villagómez Hoyos CA, Møller ND, Ewertsen C, Hansen KL, Nielsen MB, et al. Non-invasive Estimation of Pressure Changes using 2-D Vector Velocity Ultrasound: An Experimental Study with In-Vivo Examples. IEEE Trans Ultrason Ferroelec Freq Contr. 2018;65(5):709–719. https://doi.org/10.1109/TUFFC.2018.2808328.

[17] Hvid R, Jensen JA, Stuart MB, Traberg MS. Validation Platform for Development of Computational Fluid Dynamics of Intra-Cardiac Blood-Flow. In: IEEE Int. Ultrason. Symp; 2019. p. 868–871.

[18] Ramnarine KV, Nassiri DK, Hoskins PR, Lubbers J. Validation of a new blood mimicking fluid for use in Doppler flow test objects. Ultrasound Med Biol. 1998;24:451–459. https://doi.org/10.1016/s0301-5629(97)00277-9.

[19] Jensen JA, Brandt AH, Nielsen MB. Convex Array Vector Velocity Imaging Using Transverse Oscillation and Its Optimization. IEEE Trans Ultrason Ferroelec Freq Contr. 2015;62(12):2043–2053. https://doi.org/10.1109/TUFFC.2015.006970.

[20] Thirion J. Image matching as a diffusion process: an analogy with Maxwell's demons. Med Image Anal. 1998;2(3):243–260. https://doi.org/10.1016/S1361-8415(98)80022-4.

[21] Vercauteren T, Pennec X, Perchant A, Ayache N. Diffeomorphic demons: Efficient non-parametric image registration. NeuroImage. 2009;45(1):61–72. https://doi.org/10.1016/j.neuroimage.2008.10.040.

[22] Shahriari S, Kadem L, Rogers BD, Hassan I. Smoothed particle hydrodynamics method applied to pulsatile flow inside a rigid two-dimensional model of left heart cavity. Int J Numer Method Biomed Eng. 2012;28(11):1121 – 1143. https://doi.org/10.1002/cnm.2482.

[23] Caballero A, Mao W, Liang L, Oshinski J, Primiano C, McKay R, et al. Modeling left ventricular blood flow using smoothed particle hydrodynamics. Cardiovasc Eng Technol. 2017;8(4):465 – 479. https://doi.org/10.1007/s13239-017-0324-z.

[24] Mao W, Caballero A, McKay R, Primiano C, Sun W. Fully-coupled fluid-structure interaction simulation of the aortic and mitral valves in a realistic 3D left ventricle model. PLoS ONE. 2017;12(9):e0184729. https://doi.org/10.1371/journal.pone.0184729.

[25] Holbek S, Lindskov KH, Bouzari H, Ewertsen C, Stuart MB, Thomsen C, et al. Common carotid artery flow measured by 3-D Ultrasonic Vector Flow Imaging and validated with Magnetic Resonance Imaging. Ultrasound Med Biol. 2017;43(10):2213–2220. https://doi.org/10.1016/j.ultrasmedbio.2017.06.007.

[26] Correia M, Provost J, Tanter M, Pernot M. In-vivo 4D Ultrafast Vector Flow Imaging: quantitative assessment of arterial blood flow. In: IEEE Int. Ultrason. Symp; 2016. p. 1–4.

[27] Wigen MS, Fadnes S, Rodriguez-Molares A, Bjåstad T, Eriksen M, Stensæth KH, et al. 4-D intracardiac ultrasound vector flow imaging-reasibility and comparison to phase-contrast MRI. IEEE Trans Med Imaging. 2018;37(12):2619–2629. https://doi.org/10.1109/TMI.2018.2844552.

[28] Fredriksson AG, Zajac J, Eriksson J, Dyverfeldt P, Bolger AF, Ebbers T, et al. 4-D blood flow in the human right ventricle. Am J Physiol Heart Circ Physiol. 2011;301(6):H2344–H2350. https://doi.org/10.1152/ajpheart.00622.2011.

[29] Jensen J, Olesen JB, Stuart MB, Hansen PM, Nielsen MB, Jensen JA. Vector velocity volume flow estimation: Sources of error and corrections applied for arteriovenous fistulas. Ultrasonics. 2016;70:136–146. https://doi.org/http://dx.doi.org/10.1016/j.ultras.2016.04.023.

[30] Peyrat J, Delingette H, Sermesant M, Xu C, Ayache N. Registration of 4D cardiac CT sequences under trajectory constraints with multichannel diffeomorphic demons. IEEE

Trans Med Imaging. 2010;29(7):1351–1368.
https://doi.org/10.1109/TMI.2009.2038908.

Poster 1

Image based, geometry prescribed CFD of intra-cardiac flows on a dynamic heart phantom

Rasmus Hvid, Marie Sand Traberg

Published in:
COMSOL CONFERENCE 2020, Europe

Document Version:
Published

Links to Material:

Watch recording of talk - - - - - - - - - - *Accessed: 2021-08-15*
Download poster - - - - - - - - - - *Accessed: 2021-08-15*
Best Poster by Popular Vote - - - - - - - - - - *Accessed: 2021-08-15*

Image based, geometry prescribed CFD of intra-cardiac flows on a dynamic heart phantom

R. Hvid[1], M. S. Traberg[1]

1. DTU Health Technology, Technical University of Denmark, Lyngby, Denmark

INTRODUCTION A pipeline for simulating intra-cardiac blood flows from computed tomography angiography (CTA) is presented. The pipeline computes a geometry prescribed CFD based on segmentation and registration of the CTA volumes. The simulation inputs are discrete which has previously been a challenge to solve robustly.

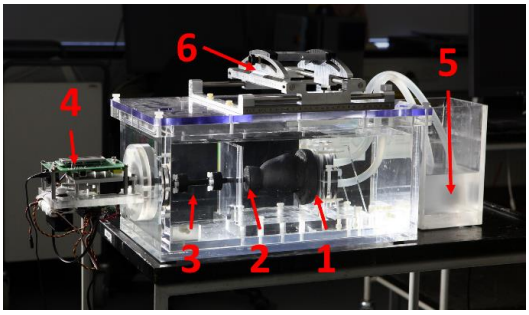

Figure 1 Dynamic heart phantom with in-house sliding fixture for ultrasound probes. **1:** Phantom base **2:** phantom apex **3:** Rod for compression **4:** Servo motors and programmable micro controller **5:** fluid reservoir **6:** Sliding fixture for ultrasound probe

EXPERIMENTAL METHODS Several experiments were made to provide model input and ground truth measurements for validation.

Phantom: The DHP mimics a human heart with two ventricles without heart valves. The phantom ventricles are compressed 10mm cyclically at 75 beats per minute in the direction of the long axis. Blood mimicking fluid is pumped through the inlet of the right phantom ventricle at 5L/min.

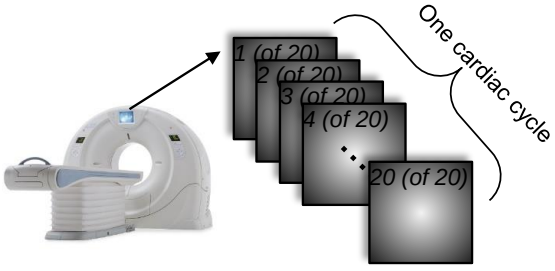

Figure 2 Visualization of the 20 volumetric images each representing a time instance of the cardiac cycle.

Ultrasound: The DHP is scanned using ultrasound vector flow imaging (VFI), see figure 4, providing planes with time-dependent fluid velocities (2D+t). 8 planes are obtained for multiple cardiac cycles each.

CTA: The DHP is scanned with CTA. The CTA data are processed and used as model input for the CFD simulation.

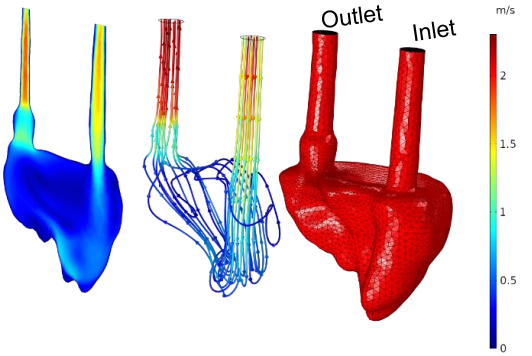

Figure 3. Visualization of 6th cardiac cycle in simulation at t=0.29s. **Left:** slice showing absolute velocity **Center:** Streamlines **Right:** Surface mesh with inlet and outlet annotation.

PRE PROCESSING The fluid domain was segmented in MATLAB as a surface mesh. The surface movement was estimated using volumetric image registration between the 20 CTA volumes. The resulting displacement field $\vec{d}(\vec{x},t)$ contains 3D vectors in a discrete 3D+t space.

$$\vec{d}(\vec{x},t) = \begin{bmatrix} d_x(x,y,z,t) \\ d_y(x,y,z,t) \\ d_z(x,y,z,t) \end{bmatrix}$$

COMPUTATIONAL METHODS A moving mesh was defined with a deforming domain and prescribed mesh displacement. The mesh movement is computed in a separate study. The CFD was modeled as a laminar, isothermal and non-compressible flow using Navier-Stokes equation. The flow was computed for 6 cardiac cycles.

Boundary conditions: Inlet: 5L/min, Outlet: 0 Pa, Wall: $\vec{u}_{wall} = \vec{u}_{\text{fluid}}$

RESULTS The CFD pipeline was successfully implemented. The flow patterns are visually assessed to be in correspondence with the measurement. See figure 4.

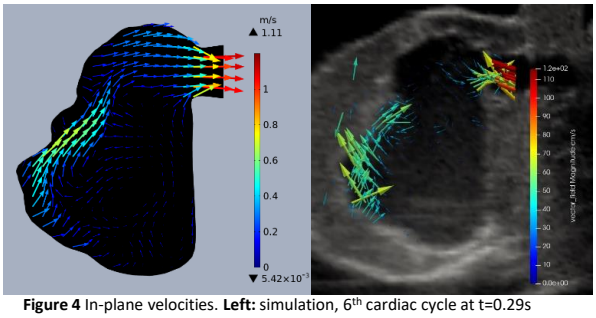

Figure 4 In-plane velocities. **Left:** simulation, 6th cardiac cycle at t=0.29s **Right:** VFI measurement of phantom 0.29s in cardiac cycle

Poster 2

A New Technique of Reconstructing 3D Geometries From CT Images - A CFD Study

Masoud Meskin, **Rasmus Hvid**, Marie Sand Traberg

Published in:
Congress of the European Society of Biomechanics 2022

Document Version:
Published

Links to Material:
Download poster - - - - - - - - - - *Accessed: 2022-10-22*

A NEW TECHNIQUE OF RECONSTRUCTING 3D GEOMETRIES FROM CT IMAGES – A CFD STUDY

Masoud Meskin (1), Rasmus Hvid (1), Marie Sand Traberg (1)

1. Cardiovascular Biomechanics Group, Technical University of Denmark, Denmark

Introduction

Numerical models have become a fundamental tool in cardiovascular studies [1]. The first step in numerical modeling is reconstructing a prototypical 3D geometry of the structure of interest from different medical imaging modalities [2]. A way to reconstruct the 3D geometry of the cardiac components is through segmenting computed tomography (CT) images and generating a mesh. However, the generated mesh may be corrupted during segmentation, resulting in a flawed or discontinuous mesh. Moreover, repairing such a corrupted mesh is a tedious task. In this work, the 3D structure of the left atrial (LA) chamber was generated with a new technique by using the "freeform part modeling" feature in the Autodesk Inventor® (Autodesk, Inc., California, USA). The created 3D LA geometry was then used in a computational fluid dynamic (CFD) study of the LA during left ventricular diastolic phase in STAR-CCM+ (Siemens Industries Digital Software).

Methods

To prepare the 3D LA geometry for the CFD study, first the LA structure at the beginning of systole was segmented, using 3DSlicer, from a 4D CT image data set and imported into Autodesk Inventor as a surface mesh (Fig.1a). Then a freeform cylinder with the approximate dimensions of the LA structure was created and divided into a number of rectangular patches (Fig.1b). Next, each rectangular patch was manipulated and formed individually to be shaped like the area of the LA structure it covers. Afterwards, the pulmonary veins (PVs) are added as cylindrical tubes with circular cross-sectional area, and the mitral valve (MV) was embedded as an oval conduit at the outlet of the LA. The LA structure was imported into STAR-CCM+ and polyhedral-shaped cells along with prismatic cells were utilized to generate volume and boundary layer mesh elements (Fig.1c and 1d). The final mesh consists of 215389 elements. The PVs and MV diameters and the inlet flowrate profiles were taken from Dahl et.al [3]. The MV was connected to a long tube and a zero pressure was set as the outlet boundary condition at the end of the tube. Blood is the working fluid and considered incompressible, with density of 1060 kg/m^3 and viscosity of 4 mPa·s.

Results

The results are mesh independent as the relative difference between the results is less than 3% after conducting mesh convergence analysis. The velocity contour on the MV plane and the intra-atrial flow field streamlines during the diastolic phase are displayed in Fig.2. The maximum transmitral velocity is 0.58 m/s and the maximum intra-atrial velocity is 0.47 m/s. The vortex rings formation is also visible in the LA chamber.

Discussion

The topology of the reconstructed LA geometry resembles the one reported by Dahl et al [3]. The values of maximum transmitral velocity and intra-atrial flow reported by Dahl et al [3] are 0.50 m/s and 0.60 m/s respectively, which are close to the findings of this study. In conclusion, the freeform technique could generate a representative model of the LA geometry.

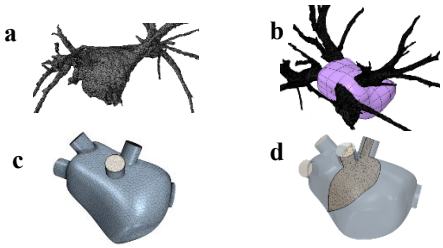

Figure 1: a) 3D surface mesh. b) freeform cylinder. covered the surface mesh. c,d) mesh structure.

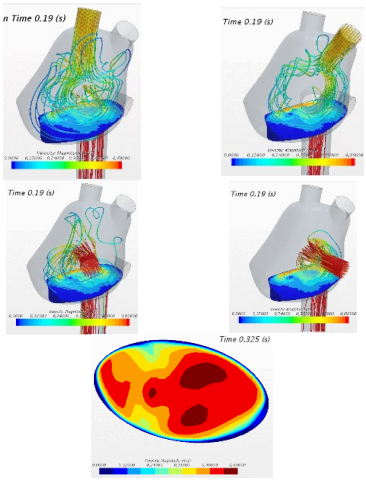

Figure 1: The intra-atrial flow field and transmitral velocity contour.

References

1. Lamata et al, Biophysics and molecular biology,2014
2. Masci et al, J Biomech Eng, 2020.
3. Dahl et al, BMES, 2012.